

Tensor networks for classical and quantum simulation of open and closed quantum systems

Fariha Azad

A dissertation submitted in partial fulfillment
of the requirements for the degree of
Doctor of Philosophy
of
University College London.

Department of Physics & Astronomy
University College London

January 24, 2024

I, Fariha Azad, confirm that the work presented in this thesis is my own. Where information has been derived from other sources, I confirm that this has been indicated in the work.

Abstract

Tensor networks are an invaluable tool for the study of quantum systems. In this thesis we use tensor networks, and more directly matrix product states, to simulate both open and closed quantum systems.

In the first part we study the one-dimensional spin-1/2 J_1 - J_2 model using a path integral constructed over matrix product states. This is a spin-model with neighbour (of strength J_1) and next-nearest neighbour (J_2) interactions. We show how this treatment is able to capture the transition from antiferromagnetic order to singlet order at the semi-classical, saddle point level, since saddle points support non-trivial entanglement structure. Taking an appropriate continuum limit, that is a generalisation of the Haldane map, we recover the previously known field theory with the crucial topological terms that determine the nature of the phase transition.

In the second part we introduce a Langevin unravelling of the density matrix evolution of an open quantum system over matrix product states, which we term the time-dependent variational principle-Langevin equation. This allows the study of entanglement dynamics as a function of both temperature and coupling to the environment. As the strength of coupling to and temperature of the environment is increased, we find a transition where the entanglement of the individual trajectories saturates, permitting a classical simulation of the system for all times.

Finally, we present a time-evolution algorithm for ion-trap based quantum computers. Here we optimise translationally invariant quantum circuit representations of states to simulate the dynamical phase transition of the quantum transverse-field spin-1/2 Ising model. We implement efficient sequential quantum circuits that are inspired by infinite matrix product states. Preliminary results on ion-trap emulators show promise for the utility of this approach.

Contents

Impact Statement	7
1 Introduction	9
1.1 Tensor Network States	14
1.1.1 Exponential size of the Hilbert space	14
1.1.2 Bosonic coherent states	16
1.1.3 Tensor network states and matrix product states (MPS)	18
1.1.4 Constructing MPS	20
1.2 Properties of MPS states	22
1.2.1 Canonical form of MPS	23
1.2.2 Calculating observables	24
1.2.3 Time evolving MPS using the time-dependent variational principle (TDVP)	24
2 Technical background	26
2.1 Field theories over tensor networks	26
2.1.1 Constructing the path integral over MPS	27
2.1.2 Example: Heisenberg antiferromagnet	28
2.2 Open quantum systems	29
2.2.1 Systems and baths	30
2.2.2 Briefly, the Keldysh formalism	31
2.2.3 A quantum particle interacting with an environment	32
2.3 Quantum simulation on quantum computers	33
2.3.1 Encoding MPS in quantum circuits	34

3	A generalised Haldane map	
	for the J_1-J_2 model	36
3.1	Introduction	37
3.1.1	Landau-Ginzburg-Wilson paradigm	38
3.1.2	One spin-1/2 Berry phase	40
3.1.3	Haldane's mapping	42
3.2	Results for the J_1 - J_2 model	43
3.2.1	The model and MPS ansatz	45
3.2.2	Energetics and phase diagram	46
3.2.3	SO(4) order parameter and continuum limit	50
3.2.4	The effective action	52
3.3	Discussion	56
3.3.1	Extending to higher dimensional J - Q models	58
4	Phase transitions in the classical simulability of open quantum systems	59
4.1	Introduction	60
4.2	A Stochastic TDVP Langevin Equation	62
4.2.1	Numerical implementation	69
4.2.2	Thermal distributions are fixed points	71
4.3	Environment induced transitions in entanglement dynamics	73
4.3.1	Results for tilted field Ising model	76
4.3.2	Scaling functions and features of open Langevin evolution	78
4.4	Limits on Classical Simulability	85
4.5	Further applications	87
4.6	Discussion	90
5	MPS algorithms for quantum computers	92
5.1	Introduction	93
5.1.1	Ion-trap quantum computing	93
5.1.2	Time-like quantum circuits	95
5.2	The algorithm	97
5.2.1	Calculating state overlaps	97
5.2.2	<i>Quantum</i> time-dependent variational principle	99

Contents

6

5.3	Results	100
5.3.1	Mitigating sampling costs	101
5.3.2	Results so far	102
5.4	Discussion	102
6	Discussion	103
	Bibliography	105

Impact Statement

Quantum systems are often difficult to understand, keep track of, and make predictions about. Tensor networks have proven to be an invaluable tool for understanding these complex quantum systems. High-dimensional tensors encapsulate quantum correlations, i.e. systems with large amounts of entanglement. Tensor networks provide a means of approximating these tensors to efficiently represent localised entanglement in quantum many-body systems. In this thesis we use tensor networks in different ways and present new tools built from these existing tools.

The research of this thesis uses tensor networks for their relevant field of study in the following ways:

Chapter 3: In this chapter we use the new tool of field theories over entangled, tensor network, states. This is a new way of capturing entanglement at the saddle point, rather than including the proliferation of instantons. We apply this to study the J_1 - J_2 model, which is a simple model of a frustrated quantum magnet, that has an interesting phase transition from singlet to antiferromagnetic order. The quantum description of electrons underpins magnetism in solid state systems. This generally presents difficult problems, but we find for such an example system, the tensor networks are able to greatly simplify the analysis and recover established results of more advanced techniques.

Chapter 4: This work presents a new tool for investigating open quantum systems; a Langevin equation over tensor network states. The study of open quantum systems is important to understand realistic experimental setups of quantum systems and the emergence of classicality. This work also identifies regions where the

influence of the environment limits the entanglement, so that the system becomes semi-classical. Such a description requires fewer computational resources to make predictions, so it is useful to identify when this occurs. In this phase there can also be no quantum advantage from using a quantum computer.

Chapter 5: In this chapter we present a tensor network based algorithm for near-term ion-trap quantum devices. Near-term quantum computers are limited by low numbers of qubits, limited fidelities, and high errors and noise. Algorithms using tensor network states can maximise use of limited resources. Such algorithms are important to understand for near-term devices, and our algorithm implementing quantum time evolution shows promise to work on quantum hardware. Ion-trap based quantum hardware have high fidelities, however they are limited by being slow. Accordingly, we are also faced with balancing the advantages and disadvantages of the ion-trap architecture.

Chapter 1

Introduction

The world at the level of the very small, *or microscopic*, is inescapably quantum. In the 1980s, scientists' newfound ability to produce high purity samples, near absolute zero temperatures, and advanced nanotechnology gave rise to a flurry of discovery – unveiling the exotic nature of low-dimensional materials. This shifted the experimental paradigm of condensed matter physics, and investigation into *quantum magnetism* and *topological materials* gained considerable traction.

Trying to explain and understand the mechanisms behind these new discoveries and also testing the predictions that follow has required the development of new theoretical tools. Some of these approaches are based in calculations of simple systems and some are based in simulation. Models and simulations show how the structure and mechanisms of a system generates the behaviour we observe.

Accessing large quantum systems efficiently is beyond the capabilities of classical computers, so techniques have been devised to overcome certain specific hurdles to do so. Some of these approaches are based on *tensor networks*, as the title of this thesis goes, which we will go on to introduce. Accordingly, an early goal of *quantum computing* was for dynamical simulations [1]. We will also introduce the type of quantum computers that exist today, which are markedly shy of this goal but still show potential for interesting experiments. Here we will show how tensor networks can allow for solutions of quantum problems that maximise the limited resources that these devices have.

So why is it that quantum systems are so difficult to understand?

From the beginning – the late 1920s brought the advent of quantum mechanics, and during this time the concept of wave-particle duality was established by de Broglie [2]. This revealed the possibility for particles, like electrons, to have further wave-like properties such as diffraction or superposition. This phenomena was soon after experimentally observed [3,4] and is now a technique that allows determination of the crystal structure of materials [5].

The magnetic moment of an atom is due to the motion of the electron. Taking the classical picture of electrons orbiting a nucleus, these closed current loops have a magnetic dipole by the laws of electromagnetism. For some atoms the individual magnetic moments across all the electrons can cancel out, implying no net magnetic dipole. The motion of electrons have an associated angular momentum, so the magnetic dipole of an atom, where it exists, is associated with the angular momentum of the atom. In quantum mechanics there is a further type of angular momentum, spin, which is the intrinsic angular momentum of a body. We can think of spins as minuscule magnets that are localised to points.

During this time it was difficult to reconcile the interaction of two electrons. Here, the *wave*-like aspects of linear superposition and quantum coherence has great consequence. Einstein, Podolsky and Rosen (EPR) set out the following thought experiment of two electrons [6]. Suppose the state of one of the electrons is spin up $|\uparrow\rangle$ and the other has its spin down $|\downarrow\rangle$. Then the state is prepared as the linear combination, $(|\uparrow\downarrow\rangle + |\downarrow\uparrow\rangle)/\sqrt{2}$. The thought experiment then separates these two electrons so that they are very far apart from each other, in the process not disturbing their quantum states.

Then, if we measure the state of one of the electron pair to be $|\uparrow\rangle$, the perfect anticorrelation of the spins *implies* the state of the other is fixed to be $|\downarrow\rangle$. EPR found this ‘action-at-a-distance’ effect unappealing. This lead them to the conclusion that quantum theory did not provide a complete description of reality. Skipping through history, this problem was further developed (i.e. Bell’s theorem [7]), which culminated into the understanding that quantum theory does indeed provide a complete description of reality – a reality that includes *quantum entanglement*. This description is at the cost of being inherently probabilistic. That is, there is a fundamental uncertainty in all observable quantities.

Classical intuition strives to remove uncertainties; probabilities concern our ignorance of a system. In quantum, randomness can be a feature and manifests interesting quantum effects. Shifting to quantum mechanics replaces a classical (say 3-dimensional) coordinate with a probability distribution of possible coordinates. The wavefunction has the simple interpretation of telling us the probability that we will find a particle at a given position.

Extending the once daunting notion of the entanglement of two electrons, i.e. individual spins, to *many* spins, opens up a whole branch of theoretical physics – lattice quantum spin systems. This is the study of how lattices with spin degrees of freedoms confined to sites interact. They are important as prototypical models of quantum systems being conceptually simple (regular structures), yet still conveying surprisingly rich physics. The study of simple low dimensional systems has led to exact solutions. Spin systems also demonstrate phase transitions, seen at the interplay between thermal and quantum fluctuations.

This quantum description of many electrons leads to quantum magnetism in solid state systems. The classical intuition would predict that atoms with net magnetic moments align on the microscopic scale leading to macroscopic magnetism. However, this alignment requires large forces between the atoms and the usual magnetic dipole interaction is too weak to explain room-temperature magnetism. That is, this should be some zero temperature phenomenon, in order to preserve the delicate ordering of spins from the disordering effects of thermal fluctuations.

In fact, it is the exchange interaction that influences the alignment of spins. This is down to Pauli exclusion principle [8] – spins interact by the electrical forces between the electrons, rather than magnetic. Forces of electrical origin are much stronger, permitting macroscopic scale magnetism even at room temperature. This interaction is also short ranged, being dependent on the overlap of atomic wavefunctions. These details make the exchange interaction easier to handle than magnetic dipole interactions. The form of this can be expressed as,

$$H = \alpha \mathbf{S}_1 \cdot \mathbf{S}_2 + \beta S_1^z S_2^z \quad (1.1)$$

where H is the Hamiltonian, an identification of the total energy of the interaction between the two atoms with spins labelled \mathbf{S}_1 and \mathbf{S}_2 .

When $\alpha = 0, \beta = J$ this is known as the Ising interaction, while for $\alpha = J, \beta = 0$ this is the isotropic Heisenberg interaction. For the Ising interaction, the one-dimensional case is trivial, and further non-trivial results are known for the two-dimensional case (Onsager solution). For the Heisenberg interaction there are many important (and non-trivial) results in one-dimension (e.g. exactly solvable models with Bethe ansatz), and beyond this, results are numerical. The combination of these interactions and accounting for external fields underpin spin dynamics.

Extending this interaction to many spins takes the form of a summation over such interacting terms. For example, nearest-neighbour interactions would consist of a sum over pairs of terms of the form of Eq. 1.1. These interactions can be extended to act non-trivially on k sites, and thus be called k -local interactions,

$$H = \sum_i h_i \quad (1.2)$$

where each of the h_i operators act on at most k sites. In the case of $k = 2$ such a h_i could be $h_i = \alpha \mathbf{S}_i \cdot \mathbf{S}_{i+1}$. k -local Hamiltonians describe realistic systems, where interactions can generally be treated as local.

From Hamiltonians we would like to determine the energy spectrum (i.e. lowest energy or ground state) or values of local observables. The obvious technique to do so is exact diagonalisation. This is a numerical scheme to calculate the exact eigenstates and energy eigenvalues of a quantum Hamiltonian by expressing the finite system in matrix form. Thermal expectation values then follow by using these values. This technique is limited to small system sizes due to memory constraints (for a chain of length N and spin-1/2, the Hamiltonian represented as a matrix has dimension $2^N \times 2^N$).

To make progress we must overcome the exponentially large vector space (equipped with *inner product*), i.e. Hilbert space \mathcal{H} , where quantum states reside, $\psi \in \mathcal{H}$. Moving beyond the particularities of particles and waves, from now we think of quantum states as these vectors ψ . Then the superposition of states follows from linearity of Hilbert space, say for a single particle qubit with eigenstates $|0\rangle$ and $|1\rangle$, any superposition of these is a valid state, $|\psi\rangle = \alpha|0\rangle + \beta|1\rangle$.

Going beyond one qubit, the qubits A and B in states $|0\rangle_A$ and $|0\rangle_B$, form a joint quantum system described by a tensor product,

$$|\psi_{AB}\rangle = |0\rangle_A \otimes |0\rangle_B. \quad (1.3)$$

However, if the total system cannot be described by specifying the states of A and B individually, much like in the EPR experiment, they are said to be entangled. For instance,

$$|\psi_{AB}\rangle = |0\rangle_A \otimes |0\rangle_B + |1\rangle_A \otimes |1\rangle_B \neq |\psi_A\rangle \otimes |\psi_B\rangle. \quad (1.4)$$

The degree to which two subsystems (say A and B) are entangled is measured by the entanglement entropy.

This can be defined by first introducing a further useful quantity, the density matrix of a system, here it is given by $\rho_{AB} = |\psi_{AB}\rangle\langle\psi_{AB}|$ (the outerproduct of these states in Dirac notation). This is a matrix that defines our quantum system. It is possible to obtain a reduced density matrix for some subsystem (say A) by *tracing out* the remainder of the system (B), $\rho_A = \text{Tr}_B |\psi_{AB}\rangle\langle\psi_{AB}|$.

The von Neumann entropy S of the reduced density matrix is the entropy of entanglement. If it is zero, the two subsystems are separable into pure states, $\rho_A = \text{Tr}_B |\psi_{AB}\rangle\langle\psi_{AB}| = |\psi_A\rangle\langle\psi_A|$, otherwise the subsystem is in a mixed state and they are entangled. In general,

$$S(\rho_A) = -\text{Tr}_A(\rho_A \log_2 \rho_A). \quad (1.5)$$

Since the joint Hilbert space of quantum systems is given by the tensor product of the individual Hilbert state spaces, Hilbert space grows exponentially. It is this feature of quantum mechanics that makes doing calculations hard. Only few problems can be solved exactly, so often problems are solved approximately, using analytical or numerical methods.

One such avenue for analytical and numerical study is using the variational principle [9]. The idea is to guess a trial wavefunction for the problem, which has adjustable parameters called variational parameters. In the following we introduce such a family of states – variational classes of quantum states called tensor networks.

1.1 Tensor Network States

Tensor networks are mathematical representations of quantum many-body states based on their entanglement structure [10]. The specific tensor network describes states with different physical properties, properties such as their dimension or energy. The tensors themselves codify some degree of entanglement or key properties of the overall wavefunction. Connecting these regions or tensors as a network builds the complex quantum state.

1.1.1 Exponential size of the Hilbert space

So far we have only briefly introduced Hilbert space, \mathcal{H} , and there we mentioned how it is *exponentially large*. Hilbert space is a complex inner product space – that is a vector space equipped with the mathematical operation of inner product. Quantum states are vectors with Hilbert space their state space. Using Dirac notation, $|\psi\rangle \in \mathcal{H}$, and for two such states, $|\psi\rangle, |\phi\rangle \in \mathcal{H}$, their inner product, $\langle\psi|\phi\rangle$, is associated with their overlap.

One of the simplest quantum systems is the qubit, a two-level system of $|0\rangle$ and $|1\rangle$. This is named as such being the quantum version of a classical binary bit. Physical examples of these systems include the spin(-1/2) of an electron, which can be either up or down. While a classical bit can be *either* 0 or 1, a qubit can be anything of the form $\alpha|0\rangle + \beta|1\rangle$, where $\alpha, \beta \in \mathbb{C}$ and $|\alpha|^2 + |\beta|^2 = 1$ ensures normalisation. These qubit states can be summarised geometrically as points on the Bloch sphere.

Further computational advantage lies in the way Hilbert space scales with the number of qubits. A system of n qubits has 2^n possible basis states. For example if $n = 3$, there are $2^3 = 8$ possible basis states, $|000\rangle, |100\rangle, |010\rangle, |001\rangle, |110\rangle, |101\rangle, |011\rangle, |111\rangle$. Thus, the dimension of vectors describing quantum states, also the dimension of matrices that describe quantum gates or operations, increases exponentially. These basis states allow for entangled combinations of these qubits, i.e. Eq. 1.4.

As a result, storing and manipulating sizeable quantum states is a near impossible task for classical computers. In the introduction we appreciate this problem and had presented solutions that include developing quantum computers. The problem is simplified by the fact that physically relevant states often have low entanglement.

These include low-energy states of generic local Hamiltonians, which are bound to live in a small corner of Hilbert space [11, 12]. How low this entanglement is, is made precise by area laws. In the following we show where this corner lies.

Area laws for entanglement scaling

The idea that the entropy of a region should scale with its boundary rather than its volume was first discovered by Bekenstein, who showed that the entropy of a black hole is proportional to its surface horizon [13]. While general relativity is expected to be described by an underlying theory of quantum gravity, it is remarkable that Bekenstein's result arises within an entirely classical theory, where no description of the microscopic nature of a black hole exists.

For a quantum many-body system existing within some volume and for some ground state, the area law conjecture is the statement that the entanglement entropy of this state scales at most with the boundary of the volume. While a classical system of n particles requires $\mathcal{O}(n)$ parameters to describe, quantum entanglement increases this to $2^{\mathcal{O}(n)}$ for the analogous quantum system. Satisfying an area law reduces this requirement, and this has been proven to be true for the interesting class of gapped one-dimensional quantum systems by Hastings [12].

The Hamiltonian gap is the difference in energy between the ground state and the first excited state. If this gap is non-zero in the thermodynamic limit, the Hamiltonian is gapped. The consequences for one-dimensional systems is that correlations decay exponentially [14], on-top of this a further stronger form of locality is imposed by area law scaling of entanglement. Furthermore, their ground states are well approximated by *matrix product states* (MPS), which are one-dimensional tensor network states. If the Hamiltonian is ungapped, correlations show power-law decay and the entropy scales with the logarithm (that is not with the system size as is true for random states) so the number of parameters remains yet lower.

This thesis focuses on using matrix product state representations for different areas of many-body quantum systems. In the following sections we introduce classes of quantum states, from coherent states to tensor network states. This leads to introducing MPS and their properties.

1.1.2 Bosonic coherent states

Before introducing tensor network states, we introduce a precursor class of states – bosonic coherent states. We present important features of these states following [15]. In the introduction, we discussed the fundamental uncertainty of quantum mechanics, this is the Heisenberg uncertainty principle. This asserts a fundamental resolution to which certain pairs of observables (i.e. the standard deviation of a particle's position σ_x and momenta σ_p) can be known, and is set by Planck's constant $h = 2\pi\hbar$, requiring $\sigma_x\sigma_p \geq \frac{\hbar}{2}$. The wavefunction of coherent states satisfy the Heisenberg uncertainty principle with equality. Because a minimum uncertainty wavepacket is necessarily a Gaussian, the expectation values of position and momentum satisfy the classical equations of motion of a harmonic oscillator.

Another aspect defining coherent states involves a continuous parametrization and a resolution of the identity [16]. This is a weighted integral over one dimensional projection operators onto the set of coherent states. This feature comes across when we write coherent states $|\alpha\rangle$, with displacement parameter $\alpha \in \mathbb{C}$, in the $|n\rangle$ basis [15]:

$$|\alpha\rangle = e^{-\frac{1}{2}|\alpha|^2} \sum_{n=0}^{\infty} \frac{\alpha^n}{\sqrt{n!}} |n\rangle. \quad (1.6)$$

These are not stationary states of the harmonic oscillator, but are appropriate for taking the classical limit. From this the overlap between coherent states is,

$$|\langle\alpha|\beta\rangle|^2 = e^{-|\alpha-\beta|^2} \quad (1.7)$$

Thus, the set $\{|\alpha\rangle\}$ is said to be *overcomplete*, since $\langle\alpha|\beta\rangle \neq 0$ for $\alpha \neq \beta$. There is still a closure relation, leading to the resolution of the identity,

$$\int \frac{d^2\alpha}{\pi} |\alpha\rangle\langle\alpha| = \mathbf{1}. \quad (1.8)$$

Inserting many such resolutions of the identity into the quantum-mechanical partition function transforms it into a sum over classical configurations. The matrix elements of this sum becomes classical Boltzmann weights. Here the resolution of the identity provides a way to take a quantum Hamiltonian to a classical Hamiltonian.

Coherent states have applications in Feynman's path integral formulation of quantum mechanics [17]. A system is described as a weighted sum over classical coherent state trajectories, that is, sequences of classical configurations. These path integrals are therefore useful for understanding the emergence of classicality. On the contrary, being composed of product (i.e. not entangled) states of coherent states, entanglement cannot be determined directly from product state field theories.

Spin coherent states

It is also possible to define spin coherent states [18]. In the introduction we introduce spin, which is a fundamentally non-classic property of matter. In algebraic properties and symmetries this quantity is very similar to angular momentum. It is a vector operator that when quantised produces a *finite* number of states.

The spin coherent state $|\underline{l}\rangle$ is obtained by rotating the highest weight S_z eigenstate to point in the direction of \underline{l} . That is, we start with a state well localised in the z -direction, and apply rotations $R(\hat{\Omega})$ where $\hat{\Omega} = (\theta, \phi)$ [19]. $|\underline{l}\rangle$ is the spin coherent state parametrised by the $O(3)$ unit vector \underline{l} , and $|\underline{-l}\rangle$ is orthogonal to it. Much like how coherent states of the harmonic oscillator are sharply peaked Gaussians in the (x, p) -plane, spin coherent states point in a particular direction to the greatest allowed extent by angular momentum commutation relations.

Here, for some value of spin S , the overlap between two states and resolution of the identity is given by,

$$|\langle \underline{l}_1 | \underline{l}_2 \rangle|^2 = \left(\frac{1 + \underline{l}_1 \cdot \underline{l}_2}{2} \right)^S \quad (1.9)$$

$$\mathbf{1} = \frac{2S + 1}{4\pi} \int d\hat{\Omega} |\underline{l}\rangle \langle \underline{l}|. \quad (1.10)$$

The spinor representation of spin coherent states is useful, and we make use of it in this thesis. Parametrizing an arbitrary normalised spinor z , this is related to \underline{l} by a Hopf or double covering map, $\underline{l} = z^\dagger \underline{\sigma} z$. For spin-1/2 the $SU(2)$ coherent state is,

$$|\psi(\theta, \phi)\rangle = \cos \frac{\theta}{2} |\uparrow\rangle + e^{i\phi} \sin \frac{\theta}{2} |\downarrow\rangle. \quad (1.11)$$

This spinor representation can be generalised for tensor network states.

Spin coherent states are the maximal allowed projection along some direction in space, and in many aspects are the *most classical* quantum spin states. When this spin analogy of coherent states was written down in the 1970s [18], it was not clear whether these would prove to be as useful as the coherent states of the harmonic oscillator. Then they had uses to discuss simple problems such as a single spin in a field, a spin wave, or two spin-1/2s with Heisenberg coupling.

They also increase physical insight to problems, but spin coherent states alone are not enough. While these are the most classical quantum states, the most entangled states are Bell states. We have introduced bosonic and spin coherent states as they are very useful and will be utilised throughout this work. The coherent states are also used as variational wavefunctions to some success, but they cannot be a complete description of a reality that is not almost classical. They are limited by the scope of entanglement that they cover.

1.1.3 **Tensor network states and matrix product states (MPS)**

Challenges in understanding strongly correlated quantum many-body systems are down to the exponential scaling of Hilbert space. A numerically efficient solution to solving and processing the quantum state is using tensor network representations. Variational classes of tensor network states have good properties such as their numerical efficiency by fulfilling the area law, and codifying the entanglement structure of a system. Such an approach is semi classical, as their parameters scale polynomially with the system size.

This ease of description comes from the natural diagrammatic notation these representations allow, meaning it is not necessary to write down formulas of tensors with many indices. We represent a single tensor by a geometric shape with legs sticking out of it, each of these legs correspond to an index, examples of these diagrams are depicted in Figure 1.1

To represent tensor contraction (e.g. matrix multiplication, vector inner products, the trace of a matrix) the indices being summed over are a shared leg between the two geometric objects as seen in Figure 1.1a. It is possible to label the direction

of these legs so that we can graphically describe vectors and their dual in Hilbert space (i.e. performing calculations with bra-ket notation) and avoid prohibited contractions, this is illustrated in Figure 1.1b.

Another useful concept to emphasise is grouping and splitting of the tensor network. For general tensors this would be a tensor rank decomposition. It is possible to group or split indices in order to lower or raise the rank. This can be seen in the Figure 1.1c, where grouping unused indices reduces this contraction to matrix multiplication. Grouping and splitting is possible because spaces of tensors are isomorphic when their overall dimensions match.

We will present these properties for the example of matrix product states (MPS). MPS are one-dimensional tensor network states where the tensors are matrices. Nice properties are guaranteed by parametrising states in the area law corner of Hilbert space. These are useful for one-dimensional physical systems by virtue of provably satisfying an area law. Their construction, and further their grouping and splitting is done using the singular value decomposition.

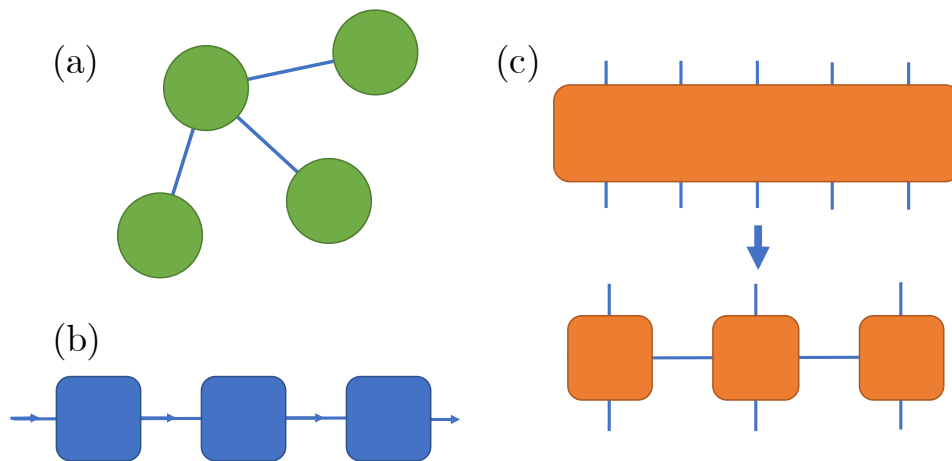


Figure 1.1: Examples of tensor network diagrams. a) Shows a general tensor of rank-3 that is being contracted with three rank-1 tensors. b) Here we have an example of matrix multiplication, i.e. contraction of rank-2 tensors. The arrows indicate the allowed order of multiplication, i.e. where it is not commutative. c) Shows pictorially tensor rank decomposition. Larger tensors can be broken up into smaller tensors, which is a useful property for calculation. The type of tensor determines how this is performed.

1.1.4 Constructing MPS

Singular value decomposition (SVD) and Schmidt decomposition

We introduce the singular value decomposition (SVD) following [20]. For matrix M , $\dim M = N_A \times N_B$, the SVD guarantees the existence of a unique decomposition $M = USV^\dagger$, where:

- U is the matrix such that $\dim U = N_A \times \min(N_A, N_B)$ with orthonormal columns (left singular vectors) so that $U^\dagger U = \mathbf{1}$. Furthermore if $N_A \leq N_B$, U is unitary, $UU^\dagger = \mathbf{1}$.
- S is the diagonal matrix such that $\dim S = \min(N_A, N_B) \times \min(N_A, N_B)$. Its entries $S_{ii} = \lambda_i$ are called singular values assumed to be in descending order. The number of non-zero singular values is the Schmidt rank of M .
- V^\dagger is the matrix such that $\dim U = \min(N_A, N_B) \times N_B$ with orthonormal rows (right singular vectors) so that $V^\dagger V = \mathbf{1}$. Furthermore if $N_A \geq N_B$, V is unitary, $VV^\dagger = \mathbf{1}$.

A key property of the SVD is that truncation of the dimension by the number of Schmidt coefficients we keep gives the optimal approximation of the matrix with respect to the Frobenius norm. We use the SVD to derive the Schmidt decomposition of quantum states. This decomposition minimally entangles these two subsystems, with entanglement given by the Schmidt values. A pure state on subsystems A and B can be written as,

$$|\psi\rangle = \sum_{ij} C_{ij} |i\rangle_A |j\rangle_B, \quad (1.12)$$

where $\{|i\rangle_A\}$ and $\{|j\rangle_B\}$ are orthonormal bases of A and B . To calculate the decomposition to $\psi = \sum_\alpha \lambda_\alpha |\alpha\rangle_A |\alpha\rangle_B$, where λ_α are the Schmidt coefficients, we re-write the state as a matrix then apply SVD. For this general state,

$$\begin{aligned} |\psi\rangle &= \sum_{ij} \sum_{\alpha}^{\min(N_A, N_B)} U_{i\alpha} S_{\alpha\alpha} V_{j\alpha}^\dagger |i\rangle_A |j\rangle_B \\ &= \sum_{\alpha}^{\min(N_A, N_B)} \left(\sum_i U_{i\alpha} |i\rangle_A \right) \lambda_\alpha \left(\sum_j V_{j\alpha}^\dagger |j\rangle_B \right) \\ &= \sum_{\alpha}^{\min(N_A, N_B)} \lambda_\alpha |\alpha\rangle_A |\alpha\rangle_B. \end{aligned} \quad (1.13)$$

Orthonormality of U and V^\dagger ensures that $\{|\alpha\rangle_A\}$ and $\{|\alpha\rangle_B\}$ are orthonormal and can be extended to be orthonormal bases of A and B . Restricting the number of Schmidt coefficients, i.e. the sum to run up to $r \leq \min(N_A, N_B)$, we obtain the Schmidt decomposition. When $r = 1$, this corresponds to (classical) product states and $r > 1$ to entangled (quantum) states.

We can use this to compute the von Neumann entropy of entanglement (Eq. 1.5) along this bipartition of the state into A and B ,

$$S_{A|B}(|\psi\rangle) = -\sum_{\alpha}^r \lambda_{\alpha}^2 \log_2 \lambda_{\alpha}^2. \quad (1.14)$$

For MPS with bond-dimension D , the entanglement is bounded by $S \leq 2 \log D$. So to simulate a system with high entanglement, the bond dimension must grow exponentially with the entropy.

Decomposition of quantum states into MPS

In the following, we briefly summarise the steps taken in [21] to arrive at the many-body wavefunction of MPS. A system of N sites, each with corresponding on-site d -dimensional Hilbert spaces, is characterised by the pure quantum state $|\psi\rangle \in \mathbb{C}^{\otimes d^N}$. Since we consider only the spin-1/2 case, we may set $d = 2$.

- To each of the N spins, we assign two virtual indices (distinguished by Greek indices), of dimension D . This is called the bond dimension.
- We assume each pair of neighbouring virtual spins corresponding to all the different sites are in a maximally entangled state, $|I\rangle = \sum_{\alpha=1}^D |\alpha, \alpha\rangle$.
- To each of the N sites we apply the SVD,

$$\mathcal{A} = \sum_{i=1}^d \sum_{\alpha, \beta=1}^D A_{i, \alpha, \beta} |\sigma_i\rangle \langle \alpha, \beta|, \quad (1.15)$$

where $\{\sigma_i\}$ form a basis of spin states on the site i .

- A_i represents the $D \times D$ matrix with elements $A_{i, \alpha, \beta}$. In general, the dimension of the maximally entangled state $|I\rangle$, and the map \mathcal{A} , can be dependent on the site. Then we write the matrix $A_i^{[k]}$ to represent the matrix corresponding to the site $k \in \{1, \dots, N\}$.

$$E_i = \begin{array}{c} \square \\ | \\ \square \end{array} . \quad (1.18)$$

Following the notation introduced so far, the topmost blue square represents the matrix A_i , and the bottom blue square is A_i^* .

1.2.1 Canonical form of MPS

Between two consecutive components of the MPS, it is possible to insert the identity MM^{-1} , where M is an invertible matrix, and not changing the overall wavefunction. This enables the choice of a *canonical form* of the MPS.

$$\begin{array}{c} \square \quad \square \\ | \quad | \\ \square \quad \square \end{array} = \begin{array}{c} \square \quad \overset{M}{\square} \quad \overset{M^{-1}}{\square} \quad \square \\ | \quad | \quad | \quad | \\ \square \quad \square \quad \square \quad \square \end{array} \quad (1.19)$$

A canonical form is a choice of fixing this degree of freedom that is convenient for calculations [10,23]. An MPS is in canonical form if each bond is the Schmidt decomposition across that index, i.e. it could have been arrived at by the decomposition into MPS. Each bond index corresponds to the labelling of Schmidt vectors across that bond. Truncating the MPS by bond-dimension is simply keeping some number of indices ordered by Schmidt coefficients. Furthermore, calculating the entropy across a bipartition of the MPS chain is simple as it is just the square of the Schmidt coefficients (as seen in Eq. 1.14).

For infinite translationally invariant MPS, this means that only one tensor and one vector of Schmidt coefficients is required to describe the whole state. In this case, when in the canonical form, the bond indices of the MPS always correspond to orthonormal vectors to the left and right. This is achieved by finding the dominant left/right eigenvectors, V_L, V_R , of the transfer matrix (Eq. 1.18). For the right transfer matrix this is solving the following fixed point equation,

$$\begin{array}{c} \square \\ | \\ \square \end{array} \begin{array}{c} \circ \\ \circ \end{array} = \begin{array}{c} \circ \\ \circ \end{array} \quad (1.20)$$

normalised, the dominant eigenvalue is 1 and V_R is called the *right environment*.

1.2.2 Calculating observables

Computing expectation values for finite MPS is clear in the diagrammatic language. The n -site operator is inserted and then the outermost transfer matrices are contracted. The setup for this calculation for a two-site operator $\hat{\theta}$ looks like,

$$\langle \psi | \hat{\theta} | \psi \rangle = \text{Diagram} \quad (1.21)$$

For the infinite MPS (with 1-site unit cell, or translational invariance), this is much the same upon canonicalisation,

$$\langle \psi | \hat{\theta} | \psi \rangle = \text{Diagram} = \text{Diagram} \quad (1.22)$$

where the canonicalisation is such that $V_L = 1$.

The operator $\hat{\theta}$ here is a two-site operator. Hamiltonians consist of sums of such n -site operators. The MPS concept can be extended to *matrix product operators* (MPOs) leading to an efficient representation of Hamiltonian operators for algorithms such as DMRG [24] for computing ground states, or for time evolution. We present one approach to time evolution in the following.

1.2.3 Time evolving MPS using the time-dependent variational principle (TDVP)

One method for time evolution is the formulation of the Dirac-Frenkel variational principle for MPS [25]. The time-dependent Schrödinger equation takes the form, $\hat{H}(t)|\psi\rangle = i\hbar\partial_t|\psi\rangle$. The key to this method is to project the time-derivative of the wavefunction onto the variational manifold.

Consider a set of complex parameters $\{X_i\}$ of the variational manifold, for MPS these are the MPS tensors. Every point in this manifold has a well defined tangent space, so the time-derivative of the wavefunction may be written $\partial_t|\psi\rangle \approx |\partial_t\psi\rangle \dot{X}_i$.

The action of the Hamiltonian will generally take us out of the variational manifold, so we project back onto the manifold by taking the inner product with $\langle \partial_j \psi |$. The path is chosen from the tangent space of this point such that the fidelity of the approximation is maximised.

Performing the orthogonal projection of the Schrödinger evolution onto the MPS manifold, the TDVP equations read,

$$\langle \partial_i \psi | \partial_j \psi \rangle \dot{X}_j = -i \langle \partial_i \psi | \hat{H} | \psi \rangle, \quad (1.23)$$

where the collection of complex-valued parameters \dot{X} represents the variational parametrisation, $|\psi\rangle = |\psi(X)\rangle$.

Remarkably, these equations are those of a classical Hamiltonian system [25]. For trajectories evolved this way, the entanglement growth is capped by $\log D$. For generic states, the MPS is not a sufficient approximation of the microstate, which should evolve to volume law entanglement entropy. Nonetheless, TDVP respects conservation laws [25] regardless of the truncation via bond dimension [26]. Accordingly, we are guaranteed that the hydrodynamic behaviour of local observables will emerge at long times irrespective of the truncation.

To implement this algorithm, we follow the approach of Haegeman *et al.* [27]. In Chapter 4 we introduce a Langevin extension to the TDVP equations, and in Chapter 5 we look at implementing TDVP on present-day quantum computers.

Chapter 2

Technical background

In this chapter we introduce the relevant background for each of the results chapters. To begin we give a brief overview of work constructing field theories over tensor network states. This is relevant to Chapter 3, where Feynman path integrals over matrix product states are employed to treat the J_1 - J_2 model. Next, we discuss open quantum systems, and aspects of the literature that relate to our new technique of Chapter 4, for simulating such systems with tensor network states. Finally, we discuss quantum simulation on quantum computers using MPS, which is background for our work in Chapter 5 implementing time-evolution algorithms on present-day quantum computers.

2.1 Field theories over tensor networks

The path integral formulation of quantum mechanics takes us from A to B by considering a sum of all possible trajectories, to return a probability amplitude. The sum is taken over these paths and the mathematics goes that finer and finer sums become integrals. These allowed trajectories are sums of classical paths, i.e. in the language so far, product state configurations. The path integral formulation is thus useful for understanding emergent classicality.

Entanglement is usually introduced into the path integral in terms of the Feynman diagrammatic expansion in small fluctuations, or by allowing for imaginary-time excursions (instantons) to describe tunnelling events [19]. In [28], another way to introduce some degree of entanglement is shown, presenting the Feynman path integral formulation over matrix product states.

2.1.1 Constructing the path integral over MPS

When introducing spin coherent states in Section 1.1.2, we showed that they form an overcomplete basis set and we wrote down an expression for the resolution of the identity. To recap, inserting resolutions of the identity over an over-complete basis set into the quantum-mechanical partition function transforms this into a sum over classical configurations. This is a way to take a quantum Hamiltonian and recover classical Hamilton's equations.

A gauge invariant measure is found to be the Haar measure for $SU(2)$ operators [28]. It is then possible to write down a resolution of the identity over MPS,

$$\mathbf{1} = \int \mathbf{D}A |A\rangle\langle A|, \quad (2.1)$$

we then do the same and insert this into the partition function at every imaginary timestep, so that we have a path integral over MPS,

$$\begin{aligned} \mathcal{Z} &= \text{Tr} e^{-\beta\hat{H}} = \prod_{\tau} \text{Tr} e^{-d\tau\hat{H}} \mathbf{1} e^{-d\tau\hat{H}} \mathbf{1} e^{d\tau\hat{H}} \\ &= \int \prod_n dA_n \dots e^{-d\tau\hat{H}} |A_n\rangle \underbrace{\langle A_n| e^{-d\tau\hat{H}} |A_{n+1}\rangle}_{(\langle A_n|A_{n+1}\rangle - d\tau\langle A_n|\hat{H}|A_{n+1}\rangle)} \langle A_{n+1}| e^{-d\tau\hat{H}} \dots \\ &= \int \mathbf{D}A e^{\int d\tau [\langle A|\partial_{\tau}A\rangle - \langle A|\hat{H}|A\rangle]} \\ &= \int [\mathbf{D}A] e^{-\mathcal{S}[A]}, \end{aligned} \quad (2.2)$$

where the measure $[\mathbf{D}A]$ contains MPS information and the action \mathcal{S} contains the expectation of the Hamiltonian, \hat{H} , and a dynamical Berry phase term arising from the difference between the MPS tensors at each imaginary timestep.

The addition of Berry phases capture the subtleties of quantum interference effects, and are crucial in underpinning the quantum nature of the phases. The path integral is dominated by paths that minimise the action. These correspond to the projection of the Hamiltonian motion through Hilbert space projected onto the restricted manifold of MPS. That is to say the saddle point equations, $\delta\mathcal{S}/\delta A = 0$ recovers the time-dependent variational principle TDVP (Sec 1.2.3).

2.1.2 Example: Heisenberg antiferromagnet

The limitations of the coherent state path integral alone is seen in the Heisenberg antiferromagnet (i.e. $J > 0$),

$$H_{AF} = J \sum_{\langle i,j \rangle} \vec{S}_i \cdot \vec{S}_j + \dots, \quad (2.3)$$

where $\langle i,j \rangle$ indicates the sum is over adjacent spins, where the operator acts on the entire Hilbert space but non-trivially at these sites, and the ellipses represent freedom in tuning short-ranged interactions to drive quantum phase transitions. For $\langle i,j \rangle$ in two dimensions, the ground state can be Néel ordered, with gapless spin-wave excitations. Whereas the disordered ground state is of singlets,

$$|\psi\rangle = \prod_{\langle i,j \rangle} \frac{1}{\sqrt{2}} (|\uparrow\rangle_i |\downarrow\rangle_j - |\downarrow\rangle_i |\uparrow\rangle_j), \quad (2.4)$$

The coherent state description of two spin-1/2 spins is given by symmetric configurations of $|L_1, L_2\rangle$. The ground state of the Heisenberg hamiltonian is the antisymmetric spin singlet $\frac{1}{\sqrt{2}}(|\uparrow\downarrow\rangle - |\downarrow\uparrow\rangle)$. This type of tunnelling between spins is not captured by the path integral over product states. However, if we consider the path integral over MPS of the form,

$$|\psi\rangle = n_1 |L_1, L_2\rangle + n_2 | -L_1, -L_2\rangle, \quad (2.5)$$

then transforming the spinor to an $O(3)$ vector \underline{n} by the Hopf map, the partition function can be written down,

$$\mathcal{Z} = \int D\psi e^{-\mathcal{S}[\psi]} = \int DL_1 DL_2 D\underline{n} e^{-\mathcal{S}[L_1, L_2, \underline{n}]}, \quad (2.6)$$

and the Berry phase \mathcal{S}_B is,

$$\mathcal{S}_B[L_1, L_2, \underline{n}] = \int dt [\langle \underline{n} | \dot{\underline{n}} \rangle + n^Z (\langle L_1 | \dot{L}_1 \rangle + \langle L_2 | \dot{L}_2 \rangle)]. \quad (2.7)$$

In the entangled path integral, the singlet state is captured at the saddle point. What would be disconnected configurations using product states are smooth fields for MPS. The manifold of saddle point configurations is increased to include semi-classical configurations. Alongside expanding about the semi-classical saddle point, increasing the bond dimension is another way to include quantum fluctuations. For an extended presentation of the theory, refer to [29].

2.2 Open quantum systems

The quantum systems we have considered so far live in this contrived universe where only the quantum system exists. Realistic descriptions of quantum systems must take into account the *environment* in which it is embedded. An open system is one that exchanges information with another *external* system. Even highly controlled quantum experiments have some degree of unavoidable openness, so an understanding of open quantum systems is vital for quantum technologies.

A system *becomes* open in the context of time evolution. Beginning with a product state of some system and environment, over time these states will become entangled, then further in time the environment will influence the quantum system to decohere. Depending on the scale of the quantum system, and its interaction with the environment, various relevant timescales appear.

Most quantum systems that are weakly coupled to a large environment usually relax to a steady state due to dissipation [30]. When the environment is in thermal equilibrium, the steady state is universally described by the Gibbs state [31]. Classically, an example of thermal equilibrium is a particle undergoing Brownian motion – random motion due to the influence of being suspended in a medium. It is understood through the Langevin equation,

$$M\ddot{x} + \gamma\dot{x} + V'(x) = F(t), \quad (2.8)$$

where $F(t)$ is a fluctuating force such that $\langle F(t) \rangle = 0$ and $\langle F(t)F(t') \rangle = 2\gamma k_B T \delta(t - t')$. This *fluctuation-dissipation* relation accounts for the competing sources of drifts and resistance to drifts leading to thermal fluctuations.

An early goal of quantum theory was to obtain differential equations for time evolution, leading to the Schrödinger equation. Similarly, this can account for the open system by introducing noise and dissipation terms as above, making it a stochastic differential equation. However, extending to interacting particles and accounting for entanglement is limited by the exponential scaling of Hilbert space.

In Chapter 4 we bypass this problem by introducing a stochastic Langevin equation for tensor network states (different to the Lindblad formalism [30]). In the following section we introduce background for this formulation. This includes the bath model used and elements of the Keldysh formalism to derive this equation.

2.2.1 Systems and baths

The total Hamiltonian for the system and the environment is made up of three components: the system contribution, the environment, and their interaction,

$$\hat{H} = \hat{H}_S + \hat{H}_E + \hat{H}_I. \quad (2.9)$$

If the initial state of system and environment is assumed to be separable, the joint system-environment state is given by,

$$|\Psi_{SE}(t)\rangle = T e^{-i \int_0^t \hat{H} dt} |\Psi_{SE}(0)\rangle = \hat{U}(t,0) |\Psi_{SE}(0)\rangle = \hat{U}(t,0) |\psi_S(0)\rangle \otimes |\psi_E(0)\rangle, \quad (2.10)$$

Direct calculations are impossible due to the huge size of the environment Hilbert space. It is useful to introduce the density matrix, $\rho_{SE} = |\Psi_{SE}\rangle\langle\Psi_{SE}|$, which is a generalisation of the wavefunction to include the possibility of uncertainty in its preparation. Then a suitable density matrix that describes the state of subsystem S is by taking a partial trace over the environment degrees of freedom, $\rho_S = \text{Tr}_E(\rho_{SE})$.

For the environment, a useful model is the Caldeira-Leggett model [32] (Fig. 2.1). This is a model of a system coupled to baths of independent Harmonic oscillators. This model enabled the first microscopic description of quantum Brownian motion and dissipative quantum tunnelling. Taking a bath of N modes with positions x_j , the relevant Hamiltonians are,

$$H_E = \frac{1}{2} \sum_{n=1}^N p_n^2 + \omega_n^2 x_n^2, \quad (2.11)$$

$$H_I = -x_0 \sum_{n=1}^N \hat{F}_n x_n, \quad (2.12)$$

where the system-environment interaction F_n is assumed to be sufficiently weak so it is well approximated by a linear coupling (also known as an Ohmic bath).

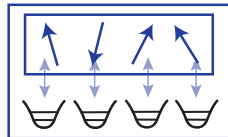


Figure 2.1: An example quantum spin system that is coupled individually to external simple harmonic oscillators. Fluctuations occurring between the single harmonic oscillator modes and the system is the source of dissipation.

2.2.2 Briefly, the Keldysh formalism

The density matrix, ρ , is an operator, so it is time-evolved by application of a forward in-time operator to its left, and a backwards in-time operator to its right, $\rho(t) = T e^{i \int_0^t H dt} \rho(0) \bar{T} e^{-i \int_0^t H dt}$. A path integral for this evolution thus has forwards and backwards evolving fields, this is known as the Keldysh path integral. Amongst the many applications of this theory, it is useful in the treatment of systems away from thermal equilibrium and open quantum systems. A Langevin equation can be constructed from a Keldysh path integral.

Keldysh's specific formulation [33] introduces what comes to be a convenient choice of variables via a *Keldysh rotation*. The fields along the forwards and backwards evolving branches of the time contours, $\phi^\pm(t)$ are transformed into their *classical* and *quantum* components,

$$\phi^{cl}(t) = \frac{1}{\sqrt{2}}(\phi^+(t) + \phi^-(t)) \quad \phi^q(t) = \frac{1}{\sqrt{2}}(\phi^+(t) - \phi^-(t)) \quad (2.13)$$

This transformation is useful for the functional formulation of the theory (i.e. writing formally the continuum limit of correlators or Green functions). The Keldysh rotation allows us to define independent Green functions, which we introduce by name,

$$\langle \phi^\alpha \bar{\phi}^\beta(t') \rangle \equiv iG^{\alpha\beta}(t, t') = \begin{pmatrix} iG^K(t, t') & iG^R(t, t') \\ iG^A(t, t') & 0 \end{pmatrix}, \quad (2.14)$$

where $\alpha, \beta = (cl, q)$ and the superscripts R, A , and K label the *retarded*, *advanced*, and *Keldysh* components of the Green function. The continuum action over the new fields is given by,

$$S[\phi^{cl}, \phi^q] = \int \int_{-\infty}^{\infty} dt dt' \left(\bar{\phi}^{cl} \quad \bar{\phi}^q \right)_t \begin{pmatrix} 0 & [G^{-1}]^A \\ [G^{-1}]^R & [G^{-1}]^K \end{pmatrix}_{t, t'} \begin{pmatrix} \phi^{cl} \\ \phi^q \end{pmatrix}_{t'}. \quad (2.15)$$

For the details of these calculations see Kamenev [33]. Further, for using the path integral over matrix product states (MPS) see [28], for a Keldysh path integral over MPS see [34]. Later in Chapter 4 we present an action of this form over MPS fields to construct the MPS Langevin equation.

2.2.3 A quantum particle interacting with an environment

Starting from the Keldysh action of a quantum particle interacting with an Ohmic bath (i.e. linear dissipation), then taking the classical limit in a certain way, yields a Langevin description. Limits can be taken in various ways. Keeping only linear terms in the quantum coordinates leads to a classical Newtonian equation that disregards both classical (thermal) and quantum fluctuations. Taking the limit $\hbar \rightarrow 0$ leads to the classical dissipative action, which has been reproduced from [33].

For a quantum particle with coordinates $X(t)$, placed in a potential $V(X)$, brought into contact with a bath of harmonic oscillators (Caldeira-Leggett model), the classical dissipative action is given by,

$$S[\vec{X}] = \int_{-\infty}^{+\infty} dt \left\{ -2X^q [\ddot{X}^{cl} + \gamma \dot{X}^{cl} + V'(X^{cl})] + 4i\gamma T (X^q)^2 \right\}. \quad (2.16)$$

From here, a Langevin equation is obtained by applying the Hubbard-Stratonovich transformation to the last term in the action,

$$\exp \left\{ -4\gamma T \int dt (X^q)^2 \right\} = \int D[\zeta(t)] \exp \left\{ - \int dt \frac{1}{4\gamma T} \zeta^2(t) - 2i\zeta(t) X^q(t) \right\}, \quad (2.17)$$

where $\zeta(t)$ is an auxiliary Hubbard-Stratonovich field. When we consider observables in terms of the classical coordinate X^{cl} , calculation leads to a delta function so that the only trajectories $X^{cl}(t)$ that contribute to observables must satisfy,

$$\ddot{X}^{cl} = -\gamma \dot{X}^{cl} - V'(X^{cl}) + \zeta(t), \quad (2.18)$$

which is a Langevin equation as introduced in Eq. 2.8, where $\zeta(t)$, the auxiliary Hubbard-Stratonovich field, appears as the time-dependent external force. This *unravelling the density matrix* generates stochastic quantum trajectories, much like a single realisation of a quantum mechanical path to be averaged over.

In Chapter 4, we introduce a new technique for the study of open quantum systems, which we dub the TDVP-Langevin equation. This technique extends usual TDVP (Sec 1.2.3) by adding noise and friction terms just as Eq. 2.18. The derivation follows as above, where the fields are now MPS fields. This picture can provide a Hamiltonian analogue to random circuit analyses of thermalisation [35–37], results for which are presented in this chapter.

2.3 Quantum simulation on quantum computers

In the 1980s Richard Feynman [1] and Yuri Manin [38] both proposed harnessing quantum mechanics to build a powerful new type of computer. Since the introductory section, we have been faced by the difficulty of modelling quantum mechanics due to the exponential scaling of Hilbert space. Perhaps this task could be tangible if we instead used *quantum computers* to simulate quantum mechanical processes.

There has been a large research effort in the area of *quantum technologies*, where much progress is being made in developing devices that exploit quantum properties of matter. We are currently in the age of *noisy intermediate scale quantum* (NISQ) computing (see [39] for a review) and seeing large technical advances so that these devices are becoming available for use. Different types of architectures are being developed for the quantum computers of the future, including superconducting chip based, photonic, and ion-trapping methods.

Independent of the architecture, the fundamental model of quantum computation is the quantum circuit model (see [40]). As is in classical computation, algorithms can be expressed as quantum circuits, which are built up of quantum gates. A quantum gate is a unitary operation, thus the quantum circuit is a way of expressing matrix manipulation. There are sets of gates that are *universal* – any quantum computation can be expressed in terms of a basis of these gates. Other models of quantum computation also exist.

For the task of quantum simulation, there is an exponential overhead of the classical computational resources required. Whereas quantum resources should scale linearly, i.e. in implementing state evolution using n spin systems. This is not true for *general* quantum simulation, certain quantum evolution can be efficiently simulated classically. Furthermore it was shown that quantum dynamics can be efficiently simulated when only a restricted amount of entanglement is present in the system, such as the quantum computation of MPS.

For NISQ devices entanglement is a limited resource due to their typical gate fidelities and achievable circuit depths. Thus, making use of low entanglement cuts and tensor networks can be one way to simulate quantum systems much larger than the devices themselves [41]. It is important to develop algorithms that make efficient use of the continually improving quantum resources available.

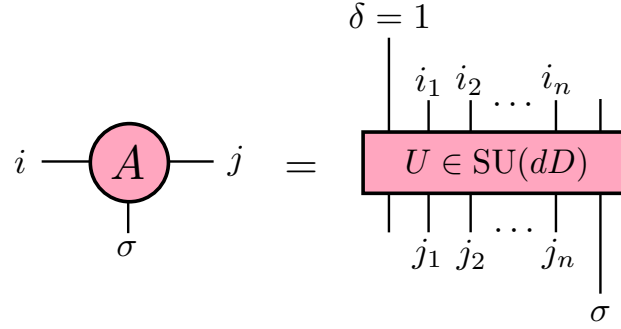


Figure 2.2: The mapping between a tensor with two virtual indices i, j of dimension D and physical index σ of dimension d , and the unitary $U \in \text{SU}(dD)$. The i, j are such that $i = i_1 \otimes i_2 \otimes \dots \otimes i_n$ and similarly for j . The way this decomposition is performed guarantees either left or right canonicalisation of the MPS. In this diagram left canonicalisation follows since $\sum_{\sigma} (A_{ij}^{\sigma})^{\dagger} A_{jk}^{\sigma} = \delta_{ik}$.

2.3.1 Encoding MPS in quantum circuits

One way to make efficient use of the limited entanglement resources of present day quantum devices is to develop matrix product state (MPS) based quantum algorithms. Rather than using the quantum simulator to simulate n quantum spins, a device of n qubits simulate states of bond dimension 2^n . This treats entanglement as a resource and for algorithms using these states, bond dimension can be increased as resources such as gate fidelities and numbers of qubits increase.

There is a natural mapping between tensors, A , of bond dimension D and local Hilbert space dimension d and the matrices $U \in \text{SU}(dD)$, $A_{ij}^{\sigma} = U_{(1 \otimes j), (\sigma \otimes i)}$ [41–44]. This equivalence between MPS and quantum channels is shown in Fig. 2.2. From this, left canonicalisation $\sum_{\sigma} (A_{ij}^{\sigma})^{\dagger} A_{jk}^{\sigma} = \delta_{ik}$, follows from the unitary property of U . This gives us a quantum channel that propagates the right environment in the spatial direction. Here the right environment is regarded as a sequence of density matrices that represent mixed states in the bond space [43]. Swapping the decomposition of U arrives at MPS in right canonical form.

In digital (rather than analog) quantum simulation, the idea is to be able to simulate quantum systems different and potentially larger than the device itself. Here computational gates approximate the time evolution of local Hamiltonians. This versatility is similar to classical computation, and we expect future quantum devices to be able to simulate complex large quantum interactions. Nonetheless, as we have seen so far, approximating *larger* systems is possible using MPS in the case of infinite translationally invariant systems.

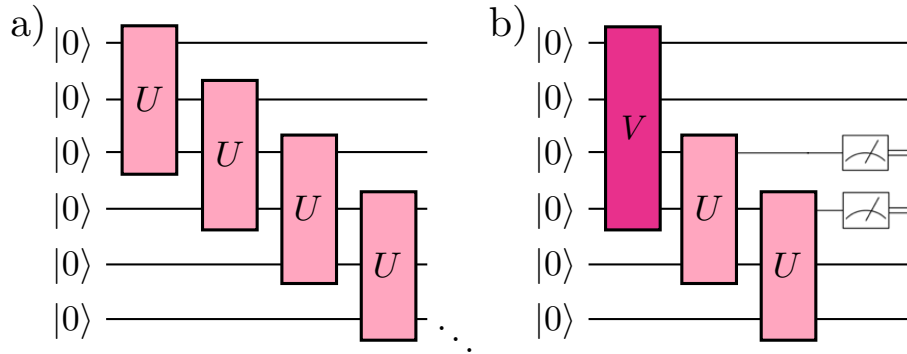


Figure 2.3: a) Infinite translationally invariant MPS. Here each unitary U is identical. In general a unitary on n qubits represents a spin-1/2 MPS of bond dimension $D = 2^{n-1}$. b) Computing expectation values of infinite MPS. For infinite MPS in left canonical form, the left of the observable is trivially the identity, while the right is summarised by $V \in \text{SU}(D^2)$. The remaining elements of the unitary encodes the tangent space structure connecting the MPS states spanning the restricted manifold.

An infinite translationally invariant MPS can be represented by an infinite quantum circuit. In Fig. 2.3a this is shown for a spin-1/2 MPS with bond dimension $D = 2^n$, with $D = 4$. For the MPS in left canonical form, the finite circuit showing calculation of local expectation values is shown in Fig. 2.3b. Here the unitaries below the operator being measured trivially contract to the identity, and the contraction above is summarised by $V \in \text{SU}(D^2)$. In general V is not known and must be solved for as Eq. 1.20. The circuit equivalent of this equation is shown in Fig. 2.4.

In Chapter 5 we develop an MPS algorithm to perform time-evolution by implementing time-dependent variational principle (TDVP). This algorithm is for ion-trap quantum devices, where the quantum circuits are laid out in *time* rather than space. In this chapter we describe how to map our quantum circuits to be time-like and make use of the circuit representation of MPS.

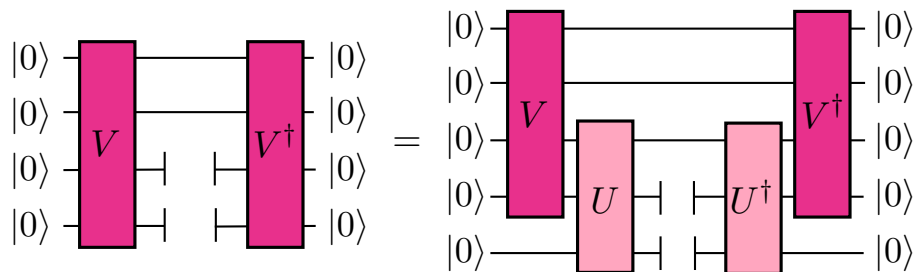


Figure 2.4: The fixed point equations for solving for the right environment. The free qubit lines imply the reduced density matrices, so that this equation is to be interpreted as the equality of these.

Chapter 3

A generalised Haldane map for the J_1 - J_2 model

Many critical phenomena in quantum many-body systems may be understood within the framework of Landau-Ginzburg-Wilson (LGW) theory. This prescribes an approach to phase transitions in terms of symmetry breaking, that has had several successful results, and indeed was believed to be a complete description of continuous phase transitions. However there are both theoretical and experimental phenomena outside of the remit of LGW theory, notably, deconfined quantum criticality. This occurs as an emergence of ‘fractional’ charge and gauge fields near quantum critical points between two conventional (LGW) phases. The J_1 - J_2 model of a one-dimensional spin-1/2 chain has a phase transition from antiferromagnetic to VBS order amongst other established results. We use these as benchmarks for the new approach using matrix product state (MPS) representations within the standard Feynman path integral and find close agreement with the field theory. Crucially, the in-built entanglement structure within the MPS ansatz is capable of describing non-classical physics at the saddle-point level. Taking an appropriate continuum limit, a generalisation of the Haldane map, we recover the known field theory with the topological terms that determine the nature of the phase transition.

This work was performed in collaboration with A. G. Green, Adam J. McRoberts, and Chris Hooley and is currently in preparation for publication [45]. My contribution to this work was in the development of the choice of MPS ansatz and underpinning how to take the continuum limit and computing the topological terms.

3.1 Introduction

At zero temperatures, with the absence of thermal fluctuations, it is *quantum* fluctuations that drive exotic quantum phase transitions. These are a type of continuous phase transition that arise by varying parameters of the system Hamiltonian, such as the magnetic field. At the quantum critical point, quantum fluctuations are scale-invariant. Here the wavefunction can be a complicated superposition of an exponentially large set of configurations that fluctuate at all available length scales, independent of the microscopic details of the system.

Path integrals are a tool for understanding quantum Hamiltonian systems and their interesting quantum phases. The prescription here is the Landau-Ginzburg-Wilson (LGW) paradigm that we will go on to introduce. Here the Feynman path integral is a useful tool in deriving the Ginzburg-Landau action for a quantum Hamiltonian. However, the existence of transitions forbidden by LGW theory means that this is not a complete description of all possible orders of quantum matter.

When it is not possible to deform the wavefunction of a system to a product state by locally removing entanglement, long-range entanglement must be present. That is, all short-range entangled states are related to product states by local unitary transformations, and long-range entangled states remain entangled no matter how you coarse-grain. The important role in governing the dynamics of topological order is played by long-range entanglement.

The LGW paradigm can discern phases between long-range order and no long-range order, but fails in the presence of long-range entanglement, like the example of the Haldane phase that we later introduce. There are many examples of phases beyond the LGW paradigm such as long-range entangled and no long-range order into no long-range entanglement and order as seen in the topological quantum spin liquid to trivial paramagnet transition.

It is also seen [46–48] that this breakdown can even occur between two Landau ordered phases. The original example of this is the antiferromagnetic phase to valence-bond solid phase transition in the spin-1/2 square lattice. This is a transition between two different long-range ordered phases, with no long-range entanglement present. Such is the “deconfined” quantum criticality scenario of extended Heisenberg models (“ J - Q ” models) with antiferromagnetic to VBS transitions.

Senthil and Fisher [49] asked whether the slow power law decay of the classical order parameters means the criticality can be described directly in terms of the order parameters. Senthil showed the importance of topological terms in underpinning the key physics of this transition. A simple example of a system hosting this antiferromagnet to VBS/singlet order transition (first shown by Haldane [14]) is the one-dimensional spin-1/2 J_1 - J_2 model. The field theory for the competing orders is in terms of an $SU(2)$ matrix U with a Wess-Zumino-Witten (WZW) term. U is a combination of the VBS and Néel order parameters, and the role of the non-trivial topological WZW term is to rotate these phases into each other, coupling the defects of the VBS phase to the charges of the coherent state vector.

We approach this phase transition using a path integral over MPS [28]. In this way we consider path integrals over entangled states. Here we parametrise the MPS in a way that is directly related to the order parameters of the two phases, capturing the qualitative physics of the key phases of the model. Even at the saddle-point level this ansatz is remarkably successful at capturing the known results. Taking the continuum limit, we show how the Berry phase terms in the resulting effective action recover the relevant topological terms in a manner very similar to Haldane [14]. This gives an explicit construction of the link between topological structures in the field theory and internal structures of the MPS tensors.

MPS played an important role in revealing the importance of topology in many-body quantum mechanics, for instance, the AKLT state which is an example of symmetry protected topological order is known as the father of MPS [50]. However, the connection between the MPS formulation and the topological terms that enter into field theories, such as those of deconfined critical systems, has not been fully elucidated. In this work we aim to make that link.

3.1.1 Landau-Ginzburg-Wilson paradigm

Until the 1980s, Landau-Ginzburg-Wilson (LGW) theory was able to capture all orders and continuous phase transitions in materials. Its most complete description brings together Ginzburg-Landau symmetry breaking theory, [51] and the renormalization group (RG) approach of Wilson [52]. Understanding quantum critical behaviour through RG flow is a nice application of RG scaling.

It can be summarised by the following key principles. (i) We can accurately describe collective thermal fluctuations near second-order phase transitions classically. Manifested in many physical quantities is an interesting universal singular behaviour. (ii) Our classical model identifies an *order parameter*, this is a thermodynamic function that is different in each phase, so can qualitatively distinguish the ordered state from the disordered state in terms of their associated symmetries. (iii) The thermal and quantum fluctuations in close proximity of the transition point of the order parameter are controlled by a continuum field theory, structured according to some simple symmetry considerations.

This formalism can be applied to certain d -dimensional quantum systems, such as the quantum Ising chain, and the coupled dimer antiferromagnet, whose critical theory is identical to the classical thermal system in $(d + 1)$ -dimensions [53]. Here instantons, that are the zero temperature quantum fluctuations, determine the quantum nature of the system.

The Néel order parameter acts as a measure of the checkerboard patterning of the antiferromagnetic Néel phase. In terms of correlation functions this is,

$$\mathcal{O}_{\text{Néel}}^\alpha = \lim_{|j-k| \rightarrow \infty} (-1)^{|j-k|} \langle S_j^\alpha S_k^\alpha \rangle. \quad (3.1)$$

The Néel ground state is adiabatically connected to the classical state with frozen spins, so does not carry long-ranged quantum entanglement [54]. The shortcomings of this approach lie here. As an example, consider the one-dimensional spin-1 Heisenberg antiferromagnet with additional crystal field anisotropy term [55],

$$H = \sum_i [S_i^x S_{i+1}^x + S_i^y S_{i+1}^y + \lambda S_i^z S_{i+1}^z + D(S_i^z)^2], \quad (3.2)$$

where the sum is over the spin-1 operators, that act on the full Hilbert space, but non-trivially at the i^{th} site, λ is an antiferromagnetic coupling term, and D is the anisotropy term. For large values of the coupling strength λ , the system is Néel ordered, while for large crystal anisotropy, D , it is in a disordered phase.

Kennedy and Tasaki approached this problem using stochastic geometric methods [56] for a path integral approach, treating it as a classical two-dimensional system with imaginary time coordinate. In this way, it is possible to discern the

phase diagram of the system qualitatively, and identify a third phase. The Haldane phase is a *topological* phase with both λ and D small. It is characterised by a hidden antiferromagnetic ordering.

If spins can take one of the values $+, -, 0$, which are quantum numbers linked to the eigenvalues of \hat{S}_Z , then it can be seen in this example configuration, $+00 - 000 + 0000 - 0+$, that Néel ordering is concealed/hidden by an unpredictable number of 0-configurations. A local order parameter would be incapable of distinguishing between the Haldane phase and the disordered phase. The non-local order parameter identifying the Haldane phase in this system is the den Nijs and Rommelse [57] string order parameter,

$$\mathcal{O}_{string}^\alpha = \lim_{|j-k| \rightarrow \infty} \left\langle -S_j^\alpha \exp \left[i\pi \sum_{l=j+1}^{k-1} S_l^\alpha \right] S_k^\alpha \right\rangle. \quad (3.3)$$

3.1.2 One spin-1/2 Berry phase

The Berry phase is a quantity that describes how a global phase accumulates as some complex vector is carried around a closed loop in a complex vector space. Since we are only interested in phases, the complex vectors can be taken to be unit vectors that we can identify with the ground state wavefunction.

An intuitive example is a spin-1/2 particle in an external magnetic field that varies around a closed loop on the unit sphere. This is because the SU(2) spinor can be mapped to an O(3) vector – building a physical picture of what the eigenstates represent since the spin aligns with the magnetic field. In external magnetic field $\vec{B} = B_0 \hat{n}$ and expressed in polar coordinates, this has Hamiltonian $H = -\gamma \vec{S} \cdot \vec{B} = -\frac{\gamma \hbar}{2} \vec{B} \cdot \vec{\sigma}$ in terms of the Pauli vector, with eigenstates

$$|+\rangle = \begin{pmatrix} \cos \theta / 2 \\ e^{i\phi} \sin \theta / 2 \end{pmatrix} \quad |-\rangle = \begin{pmatrix} \sin \theta / 2 \\ -e^{i\phi} \cos \theta / 2 \end{pmatrix} \quad (3.4)$$

When the external magnetic field varies, $\vec{B}(t)$, slowly enough (so that the final time $T \rightarrow \infty$) that the adiabatic theorem applies, the eigenstates accumulate Berry phases. The adiabatic theorem states the groundstate evolves as,

$$\begin{aligned} |\psi(t)\rangle &= U(t) |n(B(t))\rangle \\ &= e^{-\frac{i}{\hbar} \int_0^t dt' E_n(B(t'))} e^{i\gamma n(t)} |n(B(t))\rangle \end{aligned} \quad (3.5)$$

where the first part is the dynamical phase contribution, which equals 1 since cyclic evolution implies $\vec{B}(0) = \vec{B}(T)$ or we can set $E_n = 0$. The second exponential term is the geometric contribution, the Berry phase, and n labels the eigenstate at this instant. This extra geometric contribution arises by taking the overlap with $\langle\psi|$ of the Schrödinger evolution with adiabatic ansatz.

$$\langle\psi|\dot{\psi}\rangle = \dot{U}U^* + \langle n|\dot{n}\rangle = 0 \quad (3.6)$$

where the right-hand side equals zero because instantaneously, $\hat{H}(B)|n(B)\rangle = 0$.

Our goal is to compute the phase of $U(t)$ upon a closed path C in parameter space that avoids the negative z axis, i.e. the Berry phase,

$$e^{i\gamma} = e^{-\oint_C dt \langle n(\vec{B})|\dot{n}(\vec{B})\rangle} \quad (3.7)$$

For $|+\rangle$ this can be solved using polar coordinates,

$$\langle +|\frac{\partial}{\partial B}|+\rangle = i \sin^2 \theta / 2 \frac{\partial \phi}{\partial B} = \frac{i}{2} (1 - \cos \theta) \frac{\partial \phi}{\partial B}. \quad (3.8)$$

To calculate the Berry phase we can use Stokes' theorem and parametrise the interior of the closed path by τ . The path traced out by the varying magnetic field \vec{B} can be projected down to the Bloch sphere where it aligns with the path of the spin unit vector \underline{n} ,

$$\begin{aligned} \int dt \langle \underline{n}|\dot{\underline{n}}\rangle &= \int \int dt d\tau \epsilon_{ijk} n_i \partial_t n_j \partial_\tau n_k \\ &= -\frac{1}{2} \int dt (1 - \cos \theta) \dot{\phi} \\ &= -\frac{1}{2} \omega \end{aligned} \quad (3.9)$$

where ω is the solid angle subtended by the spin.

For general spin quantum number S , the Berry phase is $-S\omega$. The Berry phase is well defined since taking the pole to be the positive z axis, the resultant solid angle ω' satisfies $|\omega - \omega'| = 4\pi$ since the solid angle should add up to 4π . This contributes a factor of 2π in the Berry phase, and $e^{2\pi i} = 1$.

3.1.3 Haldane's mapping

In one-dimensional systems, the quantum Mermin-Wagner theorem implies that for $T \geq 0$ quantum fluctuations always disorder the ground state so there is no spontaneously broken symmetry. This means that the conventional means of spin-wave theory [58] cannot be used to study the disordered phases of the Heisenberg model, as this assumes a starting point of magnetic ordering. In the language of symmetry breaking, the $O(3)$ symmetry is spontaneously broken.

However, spin-wave theory is not completely abandoned. Haldane approached this problem through a mapping distinguishing the effective long- and short-wavelength behaviour of the ordered ground state. The Heisenberg antiferromagnet has a short-ranged Hamiltonian, which makes it most sensitive to short-ranged correlations. Thus, at shorter wavelengths we do not expect much deviation from Néel ordering, only at longer wavelengths deviation is appreciable. Haldane's map retains only these long-wavelength fluctuations, thus retaining the $O(3)$ symmetry.

Haldane mapped the effective long-wavelength action of the quantum Heisenberg antiferromagnet onto the nonlinear sigma model (NL σ M). The separation of short and long length fluctuations defines two continuous vector fields that capture the individual spin and collective behaviour. The spin coherent state at site i is parametrised as,

$$\hat{\Omega}_i(x, t) = (-1)^i \hat{m}_i (1 - \hat{L}_i^2)^{\frac{1}{2}} + \hat{L}_i, \quad (3.10)$$

where \hat{m} is the unimodular Néel field, and \hat{L} is the transverse canting field, chosen to obey $\hat{L} \cdot \hat{n} = 0$ and the unit vector field $\hat{\Omega}$ is such that $\vec{S}_n = (-1)^n S \Omega(\hat{x}_n)$. Dominant contributions to the path integral vary slowly in time. The \hat{n} is assumed to be smoothly varying in space and time, while \hat{L} fluctuates.

The effective action for the slowly varying fields is given by,

$$\begin{aligned} S &= \frac{1}{2g} \int \int dt dx \left(c^{-1} |\partial_t \hat{\Omega}|^2 - c |\partial_x \hat{\Omega}|^2 \right) + \frac{\Theta}{4\pi} \int \int dt dx \left(\hat{\Omega} \cdot \partial_t \hat{\Omega} \times \partial_x \hat{\Omega} \right) \\ &= \frac{1}{2g} \int \int dt dx \left((\partial_t \underline{n})^2 - (\nabla \underline{n})^2 \right) + \frac{\Theta}{4\pi} \int \int dt dx \epsilon_{ijk} n_i \partial_t n_j \partial_x n_k \end{aligned} \quad (3.11)$$

where c is the spin-wave velocity and in the second line we have transformed to polar coordinates.

The second term is the topological “theta” term, $\Theta = 2\pi S$, that can be derived from the Berry phases of the individual spins, which we have shown. The theta term is a total derivative and does not appear in the classical equations of motion. This is because on adjacent sites $\underline{n}_i \approx -\underline{n}_{i+1}$. So the Néel degrees of freedom vary as $\underline{n}_i \rightarrow (-1)^i \vec{n}_i$ and the Berry phase is the sum of the individual spin-1/2 Berry phases and the integral arises in taking the continuum limit.

The Θ term is linear in time derivatives therefore does not affect the classical limit of the equations of motion. From this term follows Haldane’s conjecture, about the nature of the disordered ground state depending on the value of the spin. For integer values of spin the ground state surprisingly has a gap and unbroken symmetry. This is the explanation of the free spin-1/2 states at the ends of the AKLT chain. Haldane’s conjecture is supported by strong numerical [59,60], theoretical [50,61], and experimental [62] arguments.

Accordingly, the Berry phases are irrelevant to the low energy properties of the Néel phase, while being crucial to capturing the paramagnetic VBS phase. Senthil et al. [48] show that these terms also modify the quantum critical point between these phases. This leads to the critical exponents to be different to those predicted by LGW theory in the absence of Berry phases.

3.2 Results for the J_1 - J_2 model

The J_1 - J_2 model on the spin-1/2 chain contains nearest and next-nearest neighbour interactions and is a simple model of competing exchange or frustration,

$$H = J_1 \sum_i \hat{\sigma}_i \cdot \hat{\sigma}_{i+1} + J_2 \sum_i \hat{\sigma}_i \cdot \hat{\sigma}_{i+2}. \quad (3.12)$$

This model played an important role in understanding the role of topology in describing quantum systems. Semi-classically, an incommensurate helimagnetic phase interpolates between the ferromagnetic and anti-ferromagnetic (Néel) phases. This shows up in a large spin treatment as a helimagnetic phase that interpolates between the antiferromagnetic and ferromagnetic phases.

When $J_1 \neq 0$ and $J_2 = 0$ this is the Heisenberg antiferromagnet. For general J_1, J_2 this magnetic order vanishes and a valence-bond solid (VBS) ground state is formed. The phase diagram varying J_1, J_2 includes the Majumdar-Ghosh point where $J_2 = J_1/2$. Here the exact ground state is given by the equal superposition of the two singlet/VBS decorations of the line.

Related to topology, is the appearance of a singlet dimer phase when $J_1/J_2 \approx 1/6$ that was first noted by Haldane [63] using a combination of fermionisation and bosonisation methods. This revealed a Kosterlitz-Thouless like transition between the singlet and antiferromagnet. A plethora of numerical and analytical approaches have been developed and deployed to reveal further features [64–70].

The transition to the dimer phase is actually not quite Kosterlitz-Thouless. This is understood through the space-time topology of the quantum states. The key additional physics as mentioned earlier in the introduction is that the topological defects in one phase are bound to the charges of the other – the boundary between two singlet or VBS phases has a (delocalised) single spin [49].

In field-theoretical treatments this is encoded through additional topological terms in the effective action. These are generalisations of the Haldane Theta term [14] and measure the space-time winding of a joint singlet-antiferromagnetic order parameter during the tunnelling events (instantons) that drive the transition between phases.

For this model, the order parameter is $\underline{u} \in \text{SO}(4)$ with $\underline{u} = (\cos\theta, \sin\theta \underline{n})$. The effective field theory is a non-linear sigma model with Berry phase term,

$$S = \int d\tau dt dx [(-\partial_t \underline{u})^2 + (\nabla \underline{u})^2] + \frac{1}{\pi} \epsilon_{ijkl} u_i \partial_\tau u_j \partial_t u_k \partial_x u_l \quad (3.13)$$

It is the Berry phase topological term that imposes a single spin at the site of a VBS domain wall.

3.2.1 The model and MPS ansatz

The simple J_1 - J_2 model has a rich phase diagram containing different quantum phase transitions. In a coherent state description, a ferromagnetic state gives way to an antiferromagnetic phase via an incommensurate helimagnetic phase with wavevector that varies as a function of J_1/J_2 – interpolating between the ferromagnetic and anti-ferromagnetic phase. Haldane showed that allowing for the possibility of singlet order modifies this phase diagram with a transition from anti-ferromagnetic to singlet order at around $J_1/J_2 \approx 1/6$. Here we focus on this transition.

We introduce an MPS ansatz that can interpolate smoothly across the phase transition between the anti-ferromagnetic and singlet phases. The ansatz,

$$|A\rangle = \begin{pmatrix} \cos \psi & 0 \\ 0 & ie^{i\xi} \sin \psi \end{pmatrix} \begin{pmatrix} |\mathbf{n}\rangle & e^{i\pi/4} |-\mathbf{n}\rangle \\ e^{i\pi/4} |-\mathbf{n}\rangle & |\mathbf{n}\rangle \end{pmatrix} \quad (3.14)$$

where $|\mathbf{n}\rangle$ represents a coherent state polarised in the direction of the unit vector \mathbf{n} , is a MPS of bond-dimension two that allows for long-range magnetic order. There is a gauge fixing implied when using coherent states, which we present at the end of this section. The angle ξ allows tuning between singlet and $S = 0$ triplet configurations and will generally be set to zero in the following considerations.

This ansatz captures all of the key phases of the J_1 - J_2 model, where the angle ψ interpolates between singlet and magnetically ordered phases. When $\psi = 0$ or $\psi = \pi/2$, we describe the product-state antiferromagnet, where $|\mathbf{n}_i\rangle = |(-)^i \mathbf{n}\rangle$. The singlet covers are obtained by taking $\psi_{\text{even}} = \pi/4$, $\psi_{\text{odd}} = 0$, $|\mathbf{n}\rangle = |(-)^i \mathbf{n}\rangle$, with the translation by one bond being made by interchanging the roles of ψ_{even} and ψ_{odd} . The ansatz can also accommodate a coexistence of (commensurate) singlet and incommensurate magnetic order by an alternation of ψ and an incommensurate modulation of \mathbf{n} .

Furthermore, this ansatz has a finite, 2-site correlation length, and as a result can be mapped to a two-layer circuit representation (see Section 2.3). Thus, the expectation of the Hamiltonian in this ansatz can be calculated exactly and manipulated analytically. Eq.(3.14) is in left canonical form with a left environment given by the identity and environment to the right of a site i given by $R_i = (\mathbf{I} + \tau_z \cos(\psi_{i+1}/2))$.

Gauge fixing

The MPS ansatz that we use entangles together coherent state configurations in a certain way. As usual in using coherent states, there is a gauge fixing implied. The polar vector \mathbf{n} and the tangent vectors in the θ - and ϕ -directions are,

$$\mathbf{n} = (\sin\theta \cos\phi, \sin\theta \sin\phi, \cos\theta) \quad (3.15)$$

$$\boldsymbol{\theta} = (\cos\theta \cos\phi, \cos\theta \sin\phi, -\sin\theta) \quad (3.16)$$

$$\boldsymbol{\phi} = (-\sin\phi, \cos\phi, 0) \quad (3.17)$$

These are the gauge fixing polar vectors, constructed so that \mathbf{n} , $\boldsymbol{\theta}$ and $\boldsymbol{\phi}$ form a right handed set. This particular choice of the two vectors $\boldsymbol{\theta}$ and $\boldsymbol{\phi}$ corresponds to the usual U(1) gauge choice for the local phase of the wavefunction.

We want to arrive at expressions in which this gauge freedom is explicit. In order to do this, we define the complex vectors $\Theta = \boldsymbol{\theta} + i\boldsymbol{\phi}$ and $\Theta^* = \boldsymbol{\theta} - i\boldsymbol{\phi}$

$$|\mathbf{n}\rangle = \cos(\theta/2) |\uparrow\rangle + e^{i\phi} \sin(\theta/2) |\downarrow\rangle \quad (3.18)$$

$$|-\mathbf{n}\rangle = -\frac{1}{2}\Theta^* \cdot \boldsymbol{\sigma} |\mathbf{n}\rangle \quad (3.19)$$

$$= \sin(\theta/2) |\uparrow\rangle - e^{i\phi} \cos(\theta/2) |\downarrow\rangle \quad (3.20)$$

where $|-\mathbf{n}\rangle$ is a coherent state orthogonal to $|\mathbf{n}\rangle$, related by $\theta \rightarrow \pi - \theta$ and $\phi \rightarrow \pi + \phi$. These relations imply that $|\mathbf{z}\rangle = |\uparrow\rangle$ and $|-\mathbf{z}\rangle = -|\downarrow\rangle$. Furthermore, with these relations we can also verify that,

$$\langle \mathbf{n} | \sigma_i | -\mathbf{n} \rangle = -\Theta_i^*. \quad (3.21)$$

3.2.2 Energetics and phase diagram

To simplify the analysis, we restrict \mathbf{n} to lie in the xy -plane with an angle between sites of Δ , such that $\mathbf{n}_i \cdot \mathbf{n}_{i+1} = \boldsymbol{\phi}_i \cdot \boldsymbol{\phi}_{i+1} = \cos\Delta$ and $\boldsymbol{\theta}_i = -\mathbf{z}$. Here $\boldsymbol{\theta}_i$ and $\boldsymbol{\phi}_i$ are unit vectors in the directions of increasing polar angles θ and ϕ . Moreover, we restrict the angles ψ_i to alternate between two values ψ_A and ψ_B on alternating bonds of the lattice. Note that while the resulting singlet order is commensurate with the lattice, this restriction permits an incommensurate magnetic order.

The expectation of the Hamiltonian Eq.(3.12) with the MPS ansatz Eq.(3.14) is calculated using the methods seen in Section 1.2,

$$E = J_1 [(\cos^2(2\psi_A) + \cos^2(2\psi_B)) \cos \Delta - \sin[2(\psi_A + \psi_B)](1 - \cos \Delta)] \\ + J_2 [2\cos^2(2\psi_A) \cos^2(2\psi_B) \cos(2\Delta) + \sin(4\psi_A) \sin(4\psi_B)(1 + \cos(2\Delta))/4]. \quad (3.22)$$

The phase diagram can be deduced by optimising Eq.(3.22) over ψ_A , ψ_B and Δ . The situation of no entanglement, $\psi_A = \psi_B = 0$, corresponds to the classical ground state phase diagram, i.e. optimising over a coherent state. The energy reduces to $E = J_1 \cos \Delta + J_2 \cos 2\Delta$, where an (incommensurate) helimagnetic phase with $\Delta = \cos^{-1}[-J_1/(4J_2)]$ interpolates between ferromagnetic and Néel order at $J_1/J_2 < -4$ and $J_1/J_2 > 4$ respectively.

For non-zero entanglement, ψ_A and ψ_B , the optimisation relies on numerical methods, these results are shown in Fig. 3.1. Over much of the phase diagram the behaviour is qualitatively similar to the result of optimising over a coherent state, except the values of J_2/J_1 where the helimagnetic phase interpolates between ferromagnetic and antiferromagnetic phases changes. Indicated by non-zero values of $\cos 2\psi$, a degree of entanglement appears, breaking lattice translation symmetry. $\psi_A = \psi_B$ everywhere, except in a small region, $0.1619 < J_2/J_1 < 1.317$.

The breaking of translational invariance of the entanglement structure corresponds to the formation of one of the two singlet phases out of the antiferromagnet. This occurs very close to $J_2/J_1 = 1/6$, which was the point identified by Haldane using Abelian bosonisation [63]. On the scales indicated in Fig. 3.1 a) and b), the singlet phase appears to form at an abrupt first order discontinuity in the parameters of the MPS ansatz. However upon zooming in, this is actually second order.

Calculation of when the energy of the state with uniform entanglement ($E = -2\cos \psi[(J_1 - J_2) \cos \psi + 2J_1 \sin \psi]$) crosses the energy of the singlet state ($E = -3J_1$) suggests that such a first order transition would occur at precisely $J_2 = J_1/6$. However, zooming in on the region around this point reveals the transition to be continuous, albeit over a narrow range of parameters from $J_2/J_1 \approx 0.1619$, the point at which the translational invariance of the entanglement structure is first broken, upto $J_2/J_1 = 3 - 2\sqrt{2} \approx 0.1716$ when the singlet order is fully formed.

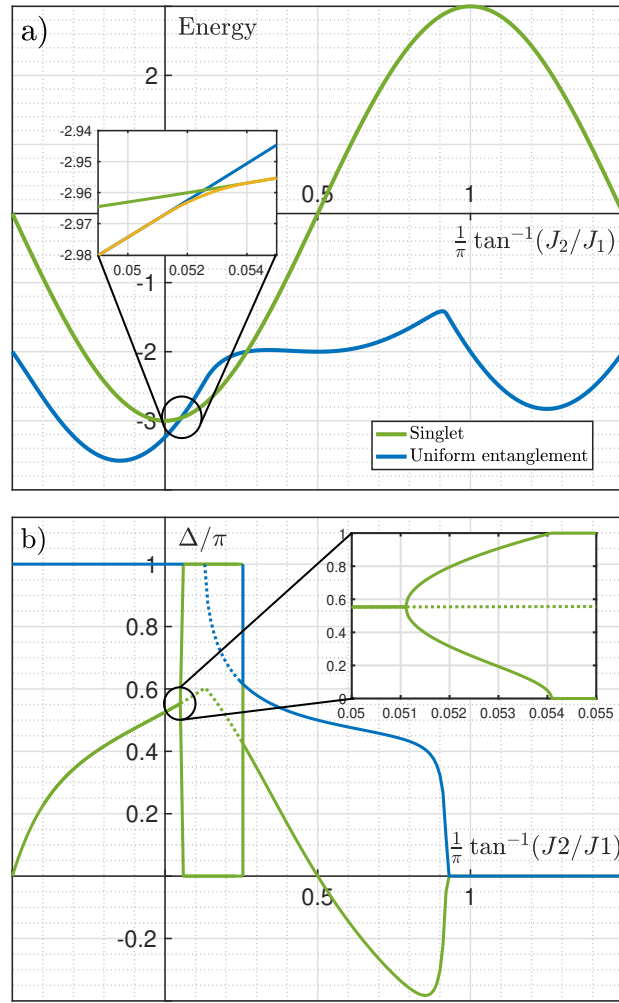


Figure 3.1: Phase diagram as a function of $\arctan(J_2/J_1)/\pi$. a) A plot of the energy through the phase diagram. The blue curve shows the energy calculated within equal entanglement on even and odd bonds, while the green curve is the energy of a singlet cover. On the scale of the main plot the phase transition between antiferromagnet and singlet appears discontinuous. However, zooming in on the transition, presented in the inset, shows that the minimum energy (in orange) is given by a smooth interpolation between the two phases. b) A plot of the helimagnetic pitch Δ/π and the entanglement parameter $\sin(2\psi)$. Over most of the phase diagram the entanglement on even and odd bonds is the same so that $\psi_A = \psi_B$. Between $J_2/J_1 = 0.1619$ and 0.1716 this symmetry is broken favouring $\psi_A = 0$ and $\psi_B = \pi/4$ (or *vice versa*). This transition is extremely rapid on the scale of the main plot. The inset shows that it is in fact continuous over a very narrow range. Dashed curves show the optimum symmetric parameters $\psi_A = \psi_B$ in the region where the translational symmetry is broken.

Haldane used a fermionic representation of the spins followed by a bosonization to instead predict a Kosterlitz-Thouless transition into the singlet phase¹. This picture will be slightly modified by the topological terms, but there will remain a

¹We believe that this is the origin of the narrowness of the transition in our treatment.

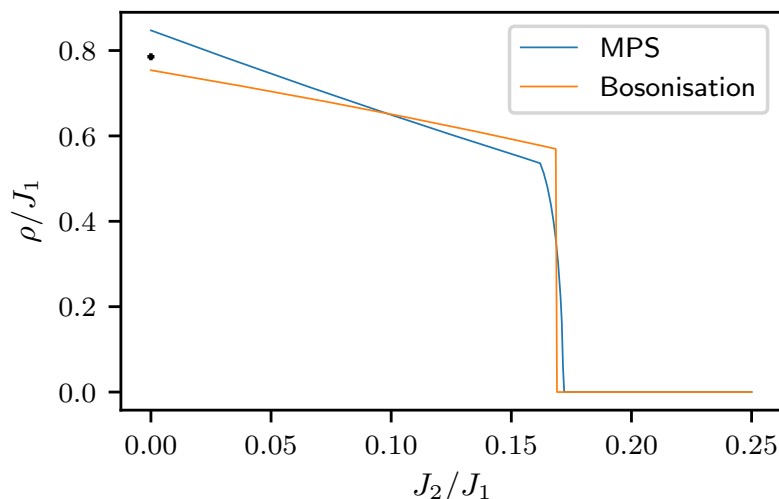


Figure 3.2: The spin stiffness ρ as a function of J_2/J_1 across the Néel-singlet transition. This is obtained for the saddle point configuration of the MPS ansatz, eq. 3.23, and the bosonized field theory [45]. There is good agreement between the two methods, with both exhibiting the jump at critical J_2 . The black point is the exact (Bethe-Ansatz) value, $\pi/4$, at $J_2 = 0$. This figure was produced by Adam J. McRoberts.

universal jump in the spin stiffness ρ (this is derived by Adam J. McRoberts in [45]). On the other hand, for the MPS ansatz, an estimate for ρ is obtained remarkably straightforwardly. We use the dependence of the pitch Δ to evaluate the resistance to inducing a twist in the magnetic order. That is,

$$\rho = \langle N \rangle \left. \frac{\partial^2 E}{\partial \Delta^2} \right|_{\Delta=\pi} \quad (3.23)$$

where $\langle N \rangle = \cos(2\psi_A) \cos(2\psi_B)$ is the Néel order parameter.

This is plotted in Fig 3.2. Here we see the universal jump associated with the KT transition is visible, that is even at the saddle-point level the MPS ansatz does a remarkably good job of capturing the key physics. The jump occurs between the split transitions, rather than discontinuously, and is broadly in agreement with the field-theoretic estimate.

The focus of this work is on this Néel to singlet order transition. Later work [49] went beyond a purely KT treatment and showed the importance of topological WZW terms in the field theory to encode the binding of spins to domain walls between singlet phases. The MPS ansatz encodes this physics directly in the structure of the spin wavefunction. In the following we show how these two perspectives can be reconciled.

3.2.3 SO(4) order parameter and continuum limit

In order to relate the MPS and field theoretical approaches, we must construct the local SO(4) order parameter and then take an appropriate continuum limit. This treats the Néel and singlet order on an equal footing. In terms of MPS Eq.(3.14), the local (Néel) magnetic order is given by

$$\mathbf{N}_i = (-)^i \langle \hat{\sigma}_i \rangle = \cos(2\psi_i) \cos(2\psi_{i+1}) \mathbf{n}_i. \quad (3.24)$$

The singlet states may be distinguished in the thermodynamic limit by a string order parameter (e.g. Eq. 3.3). However, for our purposes it suffices to identify a local singlet order parameter, which can be written when $\mathbf{n}_i \approx -\mathbf{n}_{i+1}$,

$$D_i = (-)^i \langle \hat{\sigma}_i^+ \hat{\sigma}_{i+1}^+ + \hat{\sigma}_i^- \hat{\sigma}_{i+1}^- - \hat{\sigma}_{i-1}^+ \hat{\sigma}_i^+ - \hat{\sigma}_{i-1}^- \hat{\sigma}_i^- \rangle \quad (3.25)$$

where $\tilde{\sigma}^+ = \Theta \cdot \sigma/2$ and $\tilde{\sigma}^- = \Theta^* \cdot \sigma/2$ are spin raising and lowering operators in the basis of $|\pm \mathbf{n}_i\rangle$. When \mathbf{n} is ordered in the \mathbf{z} -direction, these reduce to the usual raising and lowering operators. Then for our state ansatz, Eq.(3.14),

$$D_i = (-)^i [-\sin(2\psi_{i+1}) \cos(\psi_i - \psi_{i+2}) \cos(\psi_i + \psi_{i+2}) + \sin(2\psi_i) \cos(\psi_{i-1} - \psi_{i+1}) \cos(\psi_{i-1} + \psi_{i+1})] \quad (3.26)$$

The task now is to bring these into a single order parameter. To do so, we note the following occurs when entanglement is allowed on either only even or only odd bonds. When there is no entanglement on odd bonds ($\psi_{2i+1} = 0$) the order parameters reduce to $\mathbf{N}_{2i} = \cos(2\psi_{2i}) \mathbf{n}_{2i}$, $\mathbf{N}_{2i-1} = -\cos(2\psi_{2i}) \mathbf{n}_{2i-1}$, and $D_{2i} = D_{2i-1} = \sin(2\psi_{2i})$ so that $\mathbf{n}^2 + D^2 = 1$, forming an SO(4) multiplet². Conversely, when there is no entanglement on even bonds ($\psi_{2i} = 0$), $\mathbf{N}_{2i} = \cos(2\psi_{2i+1}) \mathbf{n}_{2i}$, $\mathbf{N}_{2i+1} = -\cos(2\psi_{2i+1}) \mathbf{n}_{2i+1}$ and $D_{2i} = D_{2i+1} = -\sin(2\psi_{2i+1})$.

The two singlet orders can be characterised by a single angle $\chi \in [-\pi, \pi]$ defined on even sites of the lattice as follows: $2\psi_{2i-1} = \chi_{2i} \Theta(\chi_{2i})$ and $2\psi_{2i} = -\chi_{2i} \Theta(-\chi_{2i})$, where $\Theta(x)$ is the Heaviside step function. In this way, positive χ_{2i} indicates entanglement between sites $2i$ and $2i + 1$, and negative χ_{2i} indicates entanglement

²Note that the roles of $\sin(2\psi)$ and $\cos(2\psi)$ are interchanged compared to the usual polar decomposition of an SO(4) multiplet.

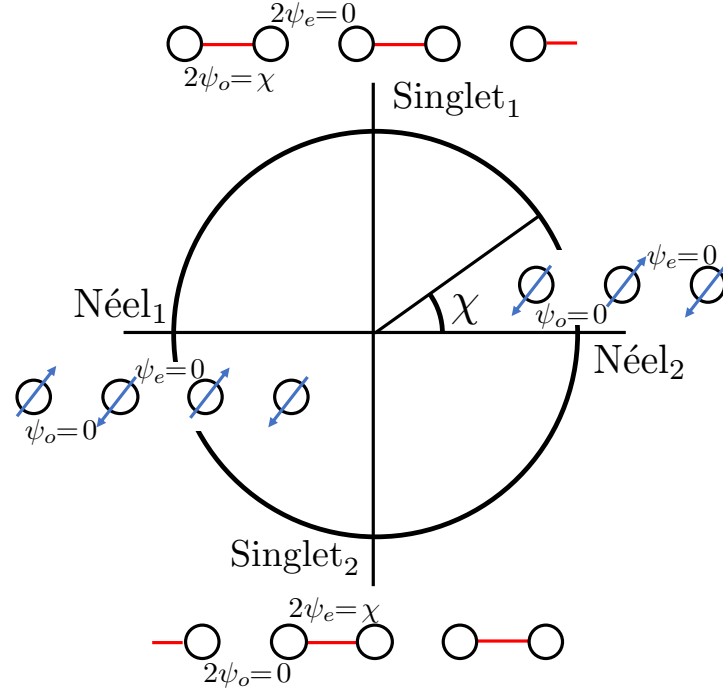


Figure 3.3: Order Parameter: The parameters of the MPS ansatz Eq.(3.14) must be patched together in order to construct the $SO(4)$ order parameter. The angle $\chi \in [-\pi, \pi]$ is introduced so that between $(0, \pi)$ it describes entanglement on odd bonds and between $(0, -\pi)$ entanglement on the even bonds. The points $\chi = 0$ and π describe the two different antiferromagnetic phases.

between sites $2i - 1$ and $2i$. Fig. 3.3 shows how the angles χ rotate between the two singlet phases and antiferromagnetic phases.

Quantum fluctuations

The saddle-point of the Hamiltonian computed within our ansatz, i.e. the uniform entanglement saddle-points of the MPS (3.14) shown in Fig. 3.1 cannot be completely characterised by the $SO(4)$ order parameter. It captures significant quantum fluctuations corresponding to instantons in the field theory between the two singlet covers. Such fluctuations are constrained in a subtle way by monogamy of entanglement and the structure of the singlet phases such that a (potentially delocalised) spin appears at the boundary between singlet orders. This is captured by the auxiliary-space structure of the MPS tensors and ultimately in the topological terms that appear in the continuum field theory.

3.2.4 The effective action

Using the $SO(4)$ order parameter and the MPS ansatz that allows a continuum limit, we can construct the field theory as an MPS path integral [28] (and see Section 2.1.1),

$$\mathcal{Z} = \int \mathcal{D}\Psi e^{i\mathcal{S}[\Psi]}, \quad \mathcal{S} = \int dt \langle \Psi | \partial_t \Psi \rangle - \mathcal{H}, \quad (3.27)$$

where $\mathcal{D}\Psi = \mathcal{D}\mathbf{n}\mathcal{D}\chi\mathcal{D}\zeta$ is over the parameters of the restricted MPS ansatz.

Despite the enforced staggering of ψ_i , we still take advantage of the entanglement captured by the ansatz at the saddle-point level (the singlet cover). The procedure we present is in essence an extension of the derivation of the action for the antiferromagnet, first carried out by Haldane [50, 58, 71]. There are three key contributions to the effective action; the expectation of the Hamiltonian, a kinetic term and a topological term.

In the lattice case, we assume entanglement only between sites $2i$ and $2i + 1$ (considering entanglement on the alternate bonds leads to the same continuum limit). We have the Berry phase,

$$\begin{aligned} \mathcal{S}_B &= \int dt \langle \psi | \partial_t \psi \rangle \\ &= \int dt \sum_i \left[\frac{i\dot{\zeta}_{2i}}{2} (1 - \cos \chi_{2i}) + \frac{i}{2} \cos \chi_{2i} \underbrace{[\dot{\phi}_{2i} \cos \theta_{2i} - \dot{\phi}_{2i-1} \cos \theta_{2i-1}]}_{\text{Area swept at } 2i \text{ minus } 2i-1} \right]. \end{aligned} \quad (3.28)$$

that is derived in the following way,

$$\begin{aligned} \mathcal{S}_B &= \int dt \langle \psi | \partial_t \psi \rangle \quad (3.29) \\ &= \int dt \sum_i \text{Tr} \langle A_i | \partial_t A_i \rangle \begin{pmatrix} \cos^2 \psi_{i+1} & 0 \\ 0 & \sin^2 \psi_{i+1} \end{pmatrix} \\ &= \int dt \sum_i \text{Tr} \begin{pmatrix} \langle \mathbf{n}_i | & e^{-i\pi/4} \langle -\mathbf{n}_i | \\ e^{-i\pi/4} \langle -\mathbf{n}_i | & \langle \mathbf{n}_i | \end{pmatrix} \begin{pmatrix} \cos \psi_i & 0 \\ 0 & -ie^{-i\zeta_i} \sin \psi_i \end{pmatrix} \times \\ &\quad \partial_t \left[\begin{pmatrix} \cos \psi_i & 0 \\ 0 & ie^{i\zeta_i} \sin \psi_i \end{pmatrix} \begin{pmatrix} |\mathbf{n}_i\rangle & e^{i\pi/4} |-\mathbf{n}_i\rangle \\ e^{i\pi/4} |-\mathbf{n}_i\rangle & |\mathbf{n}_i\rangle \end{pmatrix} \right] \begin{pmatrix} \cos^2 \psi_{i+1} & 0 \\ 0 & \sin^2 \psi_{i+1} \end{pmatrix} \\ &= \int dt \sum_i \left[i\dot{\zeta}_i \frac{1}{2} (1 - \cos 2\psi_i) + \cos 2\psi_{i+1} \cos 2\psi_i \langle \mathbf{n}_i | \dot{\mathbf{n}}_i \rangle \right. \\ &\quad \left. + i\dot{\phi}_i (\cos^2 \psi_i \sin^2 \psi_{i+1} + \sin^2 \psi_i \cos^2 \psi_{i+1}) \right] \end{aligned}$$

$$= \int dt \sum_i \frac{i\dot{\zeta}_i}{2} [1 - \cos 2\psi_i] + \frac{i\dot{\phi}_i}{2} [1 - \cos \theta_i \cos 2\psi_{i+1} \cos 2\psi_i],$$

and the Hamiltonian,

$$\begin{aligned} \mathcal{H} = & -J_1 \sum_i [\mathbf{m}_{2i-1} \cdot \mathbf{m}_{2i} + w_{2i}^z w_{2i+2}^z \mathbf{m}_{2i} \cdot \mathbf{m}_{2i+1} + w_{2i}^x (\mathbf{m}_{2i-1} \cdot \mathbf{m}_{2i} + 1)] \\ & + J_2 \sum_i w_{2i}^z w_{2i+2}^z (\mathbf{m}_{2i} \cdot \mathbf{m}_{2i+2} + \mathbf{m}_{2i-1} \cdot \mathbf{m}_{2i+1}) \end{aligned} \quad (3.30)$$

where as a last step in these calculations we have identified an $O(3)$ vector $\mathbf{w} = (\sin \chi \cos \zeta, \sin \chi \sin \zeta, \cos \chi)$ to parametrise the entanglement, and switching to a Néel field $\mathbf{m}_i = (-)^i \mathbf{n}_i$. The smoothly varying Néel order parameter amounts to introducing a polar angle that alternates between sites as $\theta_{i,odd} = \theta_i$ and $\theta_{i,even} = \pi - \theta_i$. In our assumption, $\psi_{2i+1} = 0$ on odd bonds and $2\psi_{2i} = \chi_{2i} - \pi \neq 0$ on even bonds, leading to the final form of \mathcal{S}_B , (3.28)). The first term of \mathcal{S}_B accounts for fluctuations between singlet and triplet channels. Later we set ζ to its mean-field value and discard this term.

The Hamiltonian term

The Hamiltonian contribution is the most straightforward to evaluate. This can be found by taking the continuum limit of the Hamiltonian directly.

$$\begin{aligned} E = & J_1 \sum_i \left[\begin{array}{l} \mathbf{n}_{2i-1} \cdot \mathbf{n}_{2i} \\ -\frac{1}{2} \sin \chi_{2i} (e^{-i\zeta_{2i}} \Theta_{2i-1} \cdot \Theta_{2i} + e^{i\zeta_{2i}} \Theta_{2i-1}^* \cdot \Theta_{2i}^*) \\ + \cos \chi_{2i} \cos \chi_{2i+2} \mathbf{n}_{2i} \cdot \mathbf{n}_{2i+1} \end{array} \right] \\ & + J_2 \sum_i \cos \chi_{2i} \cos \chi_{2i+2} (\mathbf{n}_{2i} \cdot \mathbf{n}_{2i+2} + \mathbf{n}_{2i-1} \cdot \mathbf{n}_{2i+1}). \end{aligned} \quad (3.31)$$

Identifying the same $O(3)$ vector \mathbf{w} to parametrise the entanglement, using the notation $w^\perp = \sin \chi$ for compactness, and switching to Néel parameters $\mathbf{n}_{2i+1} \rightarrow -\mathbf{n}_{2i+1}$, $\phi_{2i+1} \rightarrow -\phi_{2i+1}$, and, $\theta_{2i+1} \rightarrow +\theta_{2i+1}$. Then,

$$\begin{aligned} E = & -J_1 \sum_i \left[\begin{array}{l} \mathbf{n}_{2i-1} \cdot \mathbf{n}_{2i} \\ +\frac{1}{2} w_{2i}^\perp (e^{-i\zeta_{2i}} \Theta_{2i-1} \cdot \Theta_{2i}^* + e^{i\zeta_{2i}} \Theta_{2i-1}^* \cdot \Theta_{2i}) \\ + w_{2i}^z w_{2i+2}^z \mathbf{n}_{2i} \cdot \mathbf{n}_{2i+1} \end{array} \right] \\ & + J_2 \sum_i w_{2i}^z w_{2i+2}^z (\mathbf{n}_{2i} \cdot \mathbf{n}_{2i+2} + \mathbf{n}_{2i-1} \cdot \mathbf{n}_{2i+1}). \end{aligned} \quad (3.32)$$

We manipulate the exchange term into a form from which we may directly take the thermodynamic limit. This is to find the optimal angles ξ_{2i} to minimise the energy.

One can rotate between the real and imaginary parts of $\Theta = \theta + i\phi$ by multiplying by a phase factor; $\Theta' = \theta' + i\phi' = e^{i\mu}(\theta + i\phi)$. This corresponds to the U(1) gauge freedom in our choice of vectors orthogonal to \mathbf{n} . It is always possible to make such a rotation so that $\theta'_{2i-1} = \theta'_{2i} \propto \mathbf{n}_{2i-1} \times \mathbf{n}_{2i}$ (or alternatively $\phi'_{2i-1} = \phi'_{2i} \propto \mathbf{n}_{2i-1} \times \mathbf{n}_{2i}$) in which case $\phi'_{2i-1} \cdot \phi'_{2i} = \mathbf{n}_{2i-1} \cdot \mathbf{n}_{2i}$.

The expectation of the energy is then,

$$E = -J_1 \sum_i \left[\begin{array}{l} \mathbf{n}_{2i-1} \cdot \mathbf{n}_{2i} \\ + w_{2i}^x \cos(\xi_{2i} + \mu_{2i-1} - \mu_{2i})(\mathbf{n}_{2i-1} \cdot \mathbf{n}_{2i+1}) \\ + w_{2i}^z w_{2i+2}^z \mathbf{n}_{2i} \cdot \mathbf{n}_{2i+1} \end{array} \right] \quad (3.33)$$

$$+ J_2 \sum_i w_{2i}^z w_{2i+2}^z (\mathbf{n}_{2i} \cdot \mathbf{n}_{2i+2} + \mathbf{n}_{2i-1} \cdot \mathbf{n}_{2i+1}).$$

The optimum value of ξ_{2i} is given when $\xi_{2i} + \mu_{2i-1} - \mu_{2i} = 0$. This corresponds to maximising the singlet order on the bond \mathbf{n}_{2i-1} and \mathbf{n}_{2i} . The subsequent treatment expands around this value. Taking the continuum limit in the usual way leads to the final expression,

$$E = \frac{1}{2} \int dx \left[\begin{array}{l} [J_1(1 + (w^z)^2 + w^\perp)/2 - 4J_2(w^z)^2](\nabla \mathbf{m})^2 \\ + (2J_1 - 4J_2)(\nabla w^z)^2 \\ - J_1 - 2J_1 w^x + (2J_2 - J_1)(w^z)^2 \end{array} \right]. \quad (3.34)$$

where \mathbf{m}_i are Néel parameters, $\mathbf{m}_{2i} = (-)^{2i+1} \mathbf{n}_{2i+1}$, and $w^\perp = \pm 1$ in the singlet phase.

This energy has a mean field transition in the bare theory at $J_1 > 0$ and $J_2 = 0$ between a partially antiferromagnetic phase at $J_2 < 0$ and a perfect singlet phase at $J_2 > 0$. Quantum fluctuations are expected to shift the position of this transition (and to restore the translational symmetry in some regions of the phase diagram) to recover the results of the previous MPS analysis.

Kinetic terms

The relevant saddle-points of this action are the two singlet covers, where $\chi = \pm\pi/2$. By retaining the ξ -dependence of the Berry phase and energy, then expanding to

second order in the deviations of ζ from its equilibrium value in either case, and then integrating it out, we obtain a kinetic term $(\partial_t \chi)^2 / 32J_1$.

The \mathbf{m} -contribution can be derived in a very similar way as the anti-ferromagnet (see Haldane's mapping function, Section 3.1.3 and (3.10)). Separating \mathbf{n} into slow ($c = 0$) and fast ($c \approx \pi$) degrees of freedom, \mathbf{m} and \mathbf{l} respectively (note that we have not retained \mathbf{l} in (3.30)), and expanding the Berry phase to first order in the fast degree of freedom, leaves the contribution $\int \cos \chi \mathbf{l} \cdot (\mathbf{m} \times \partial_t \mathbf{m}) dt$. The leading contribution to the fast degrees of freedom of the Hamiltonian is given by $\chi_0 \mathbf{l} \cdot \mathbf{l}$. Integrating out \mathbf{l} , we obtain a kinetic term $\chi_0^{-1} \cos^2 \chi (\partial_t \mathbf{m})^2$.

The topological term

The effective field theory of the J_1 - J_2 model has a topological term that encodes the structure of the defects between the two singlet phases or between two Néel phases. This can be obtained substituting Eq.(3.10) into \mathcal{S}_B , Eq.(3.28) following Haldane's steps in the derivation of the Theta term for the antiferromagnet. The topological term arises from the second term of \mathcal{S}_B (3.28). In the continuum limit this becomes,

$$\begin{aligned} i\Omega &= \int d\tau \sum_{2i} \frac{i}{2} \cos \chi_{2i} (\dot{\phi}_{2i} \cos \theta_{2i} - \dot{\phi}_{2i-1} \cos \theta_{2i-1}) \\ &\sim \int d\tau dx \frac{i}{4} \cos \chi (\partial_\tau \phi \partial_x \cos \theta - \partial_x \phi \partial_\tau \cos \theta) \end{aligned} \quad (3.35)$$

Here, the second term follows after integrating by parts, and θ and ϕ are now the angular co-ordinates of the Néel field \hat{m} . Note the factor of 1/2 in changing from the sum over n to the integral over x . Eq.(3.35) is the polar coordinates version of the SO(4) topological term identified in [49].

$$\Omega = \frac{2\pi k}{2\pi^2} \int_0^1 d\zeta \int d\tau dx \epsilon_{abcd} u_a \partial_\zeta u_b \partial_\tau u_c \partial_x u_d \quad (3.36)$$

where $k \in \mathbb{Z}$ is odd. The factor of $2\pi^2$ in the denominator is the area of S^3 , the unit three-sphere, and $u(\zeta, \tau, x)$ is an extension of the field $u(\tau, x) = (\sin \chi, \cos \chi \mathbf{m}) \equiv (u_0, \mathbf{u})$ satisfying

$$u(\zeta = 0, \tau, x) = (1, 0, 0, 0) \quad (3.37)$$

$$u(\zeta = 1, \tau, x) = u(\tau, x) = (\sin \chi, \cos \chi \mathbf{m}) \quad (3.38)$$

In the MPS treatment, the internal structure of the ansatz constrains domain walls between different singlet phases to contribute to the overall Berry phase as a free spin. The topological term imposes this same constraint in the field theory. To see this consider a Néel order for \mathbf{n}_i without x -dependence and a static smooth interpolation of $\cos \chi$ between $-\pi$ and π . In this case, using the second form of the Berry phase, Eq.(3.35), the integral over space can be carried out leaving a result equal to the Berry phase of a single spin.

The resultant field theory

We switch to the standard angular coordinates on S^3 , i.e. define $\alpha = \pi/2 - \chi$, in terms of which $(w^z)^2 = \sin^2 \alpha$ and $(\partial w^z)^2 \sim (\partial \alpha)^2$. Then, in summary, we have derived the following field theory from the MPS ansatz,

$$\mathcal{S} = i\Omega + \int dt dx \left[\frac{1}{32J_1} ((\partial_t \alpha)^2 + \sin^2 \alpha (\partial_\tau \hat{\mathbf{m}})^2) + (J_1 - 2J_2) ((\partial_x \alpha)^2 + \sin^2 \alpha (\partial_x \hat{\mathbf{m}})^2) + V(\alpha) \right], \quad (3.39)$$

where the dimerisation potential is,

$$V(\alpha) \approx -\frac{3J_1}{2} + \frac{J_2}{2} - \frac{J_2}{2} \cos 2\alpha \quad (3.40)$$

The action was derived directly from an MPS parameterisation of the spin states Eq.(3.14). This form of the action makes the physics of the transition particularly transparent, if $J_2 < J_2^c$, the potential $V(\alpha)$ is irrelevant and the SO(4) symmetry emerges in the infrared, while the topological term ensures the theory remains gapless. Whereas if $J_2 > J_2^c$, the $V(\alpha)$ term appears, and the SO(4) symmetry is broken in favour of dimer order.

3.3 Discussion

This work has introduced an MPS ansatz that reproduces key features of the phases transitions of the J_1 - J_2 model, encompassing ferromagnetic, Néel, spiral, and dimer orders. When optimised for the J_1 - J_2 Hamiltonian, it shows a very rapid, but continuous transition between antiferromagnetic and singlet order in the vicinity

of $J_2/J_1 = 1/6$. This is the transition point found by Haldane in his fermionisation/bosonisation treatment of the same model³.

In this work an $SO(4)$ order parameter combining the Néel and singlet orders is identified, and a continuum path integral constructed over MPS fields parametrised by this. The construction is similar to that for the antiferromagnet, but using MPS valued fields rather than coherent states.

The MPS treatment parametrises the microscopic structure of topological defects in the spin configuration. Specifically, the presence of a single (delocalised) spin at the boundary between singlet phases. Haldane's original treatment showed that the transition is Kosterlitz-Thouless like⁴. It is remarkable how the simple MPS ansatz captures so many key features of this transition at the saddle-point level. The underlying Kosterlitz-Thouless character is presumably responsible for the rapidity of the transition.

The MPS state effectively re-sums instantons of the coherent state theory and encodes their topological structure in the local structure of the MPS fields. This connection has been noted previously [28, 72]. The contribution made here is to show how the MPS faithfully encodes topological features, and how these lead directly to topological terms encoding the same information in the field theory.

It is intriguing to speculate that this connection between topological terms in a field theory and the structure of MPS ansätze could be used more generally as a method to re-sum instantons, in favour of a higher bond-dimension MPS path integral. Indeed, finite correlation-length MPS tensors – such as those used in this work – play a special role in classification of symmetry protected topological order.

Ultimately, it would be desirable if these methods could be extended to two-dimensions to capture similar physics in models such as the J - Q model [48]. This is tricky because generic PEPS states are not efficiently contractible rendering a PEPS path integral non-local (a criteria for the MPS path integral discussed in Section 2.1.1), although it may be possible to circumvent this difficulty by using sequential circuit ansätze [73].

³If one restricts to helimagnetic phases with translationally invariant entanglement and purely singlet phase, then the transition is first order at exactly $J_2/J_1 = 1/6$.

⁴Where logarithmic corrections occur due to the topological term in the action.

3.3.1 Extending to higher dimensional J - Q models

The J - Q model, also known as the coupled dimer antiferromagnet [54], extends the Heisenberg antiferromagnet. This is a model on the two-dimensional square lattice with Hamiltonian,

$$H = J \sum_{\langle ij \rangle} \sigma_i \cdot \sigma_j + Q \sum_{\langle ijkl \rangle} (\sigma_i \cdot \sigma_j - 1)(\sigma_k \cdot \sigma_l - 1) \quad (3.41)$$

where the second sum is to be taken over plaquettes, i.e. opposite sides of the unit square of the lattice. This model also hosts the VBS to antiferromagnetic transition, as previously introduced.

This is an example of higher dimensional deconfined quantum criticality. Here we consider the order parameter $\underline{u} \in \text{SO}(5) \setminus \text{SO}(4)$ given by $\underline{N} = (\underline{v} \cos \theta, \underline{n} \sin \theta)$, where $\underline{v} \in \text{O}(2)$ is the VBS contribution and $\underline{n} \in \text{SO}(3)$ is the Néel vector [74]. Similar to the Haldane map, the topological WZW term [46,49] is a mapping function, which contains the order parameter field $\underline{u} \in \text{SO}(5)$ that drives the non-trivial physics of this model. The effective action is given by,

$$S = \int dt dx dy d\tau [(\partial_t \underline{u})^2 + (\nabla \underline{u})^2] + \epsilon_{ijklm} u_i \partial_t u_j \partial_x u_k \partial_y u_l \partial_\tau u_m \quad (3.42)$$

The topological term couples defects of the VBS phase to the charges of the coherent state vector. It counts a free spin \underline{n} worth of Berry phase in the middle of the vortex \underline{v} . Capturing this behaviour by a generalised Haldane map in the field theory over entangled states is an overarching goal. Here we have shown this for the simpler example, the one-dimensional J_1 - J_2 model.

Chapter 4

Phase transitions in the classical simulability of open quantum systems

A key challenge for quantum technologies lies in understanding how the quantum system interacts with its environment and how this interaction affects the quantum nature of the system. This chapter introduces a new technique for the simulation of open quantum systems, and shows how this can be used to demonstrate novel features in entanglement dynamics. Specifically, we take a Langevin trajectories approach that allows for fine tuning of the environment parameters. As the strength of coupling to and temperature of the environment is increased, we find a transition where the entanglement of the individual trajectories saturates, thus permitting a classical simulation of the system for all times.

This work was performed in collaboration with Andrew G. Green, Andrew Hallam, and James Morley and has been published [75]. My primary contribution to this work was looking at the application of this technique as a probe of entanglement dynamics. The data collected to produce the figures in this chapter is available online, DOI: 10.5522/04/22732289.

4.1 Introduction

In Chapter 1, we introduce open quantum systems and how they lend to the classical world we observe. We also introduce the different approaches to their study. One is where we describe the evolution of the density matrix with master equations. Where the inclusion of Lindblad operators account for the effects of an environment. Another is to use stochastic trajectories of pure quantum systems that can reproduce results of the former approach upon averaging.

This is more aligned with the Langevin approach that gives a good account of the thermal properties of the system-bath interaction. Accounting for both temperature and coupling to the environment is achieved due to their satisfying a fluctuation-dissipation relation. These parameters appear in the equations of motion as separate terms so they can be fine-tuned and studied individually.

While Langevin methods have been used extensively for quantum systems, they can be limited to individual quantum systems that do not take into account entanglement. Extending the Schrödinger equation to a stochastic differential equation by accounting for noise and dissipation becomes the usual problem of exponential scaling of Hilbert space.

It is at this point that tensor network states prove useful with their tunable degree of entanglement. We derive and present a technique for simulation of open quantum systems that makes use of a variational parametrisation of trajectories obtained by unravelling the evolution of an open system density matrix. The equations of motion of each trajectory can be considered a Langevin extension of the time-dependent variational principle (TDVP). This extension adds noise and friction terms to the original TDVP equations [25].

This work is of two parts, the technique itself and the interesting physics observed by applying this tool. We apply this technique to probe entanglement dynamics in open systems. Open system dynamics act to disentangle and cause decoherence, furthermore, classical behaviour in open systems can often be emergent. This is linked to the complexity of describing the open system at early and late times. Broadly speaking, an open quantum system can be termed classical in at least two different ways.

On one hand, if a quantum system is in a weakly-entangled state, it may be considered classical as long as the entanglement remains low. In this early time limit, semi-classical equations of motion of the system apply – growing entanglement makes this problem intractable. On the other hand, an open system behaves classically once the coupling to the environment has caused dephasing.

Can these views be reconciled and a classical description developed that works from the earliest to the latest times? Recent insights have made steps towards such an understanding for open systems. The interplay between entangling dynamics and frequent projective or weak measurements has been explored [35,76–81]. The transition from volume law to area law entanglement allows such a classical (i.e. weakly-entangled) description of the system for all times.

Such semi-classical descriptions and the transition in entanglement growth are related to the quantum Zeno effect. This is the phenomenon by which frequent measurement in a channel impedes transitions in that channel [82]. The nature of a transition to a many-body quantum Zeno phase has been studied extensively [83–93] and similar analyses extended to measurement-induced transitions in open Hamiltonian systems [94–97].

For closed systems, the TDVP equations constitute a semi-classical limit; they correspond to classical Hamilton equations of motion on the variational manifold [25,98]. As the entanglement grows during the Hamiltonian evolution, the TDVP equations break down as a larger and larger variational manifold is required in order to capture the state and its dynamics, alongside a larger and larger error when projecting the evolved states back to a given variational manifold. In this sense, the semi-classical description is confined to early times, where a finite bond order simulation is sufficient to capture the entanglement.

In our stochastic TDVP Langevin equation applied to MPS, we find thresholds in the dynamics of individual trajectories as a function of coupling to and temperature of the environment. Beyond a certain coupling strength, the bath-system interaction causes the entanglement to saturate at a low value, so that a low-bond order MPS description gives high fidelity for all time. This constitutes a transition in the classical describability of the open quantum system: the low bond order TDVP Langevin equation is an effective semi-classical description that works for all time.

This chapter is organised as follows. We begin by introducing the stochastic TDVP-Langevin equation in Sec. 4.2. Here we discuss its derivation and numerical implementation. Then in Sec. 4.3 we introduce some results from applying this technique, studying the open evolution of a rapidly entangling system. Here we see a transition to a quantum Zeno phase as the strength of coupling to the environment is increased in different limits (finite temperature, noise, friction). We then look more closely at our data and discuss scaling relations and how the data collapse is different before and after the transition in Sec. 4.3.2. Finally we explore limits on classical simulability in Sec. 4.4 and efficiency of our approach, then we look into further avenues for this work in Sec. 4.5.

4.2 A Stochastic TDVP Langevin Equation

Langevin equations describe the motion of a system coupled to an environment (or alternatively the motion of slow collective degrees of freedom in an effective bath described by the faster degrees of freedom [99]) by adding noise and friction terms to the basic equations of motion of the system.

If the environmental degrees of freedom are in thermal equilibrium, the friction and noise satisfy a fluctuation-dissipation relation. Applied to quantum systems, the Schrödinger equation provides the basic equations of motion. The ensemble of the resulting stochastic Schrödinger trajectories recovers the density matrix evolution and is said to be an unravelling of it.

The TDVP Langevin equation can be written in its Markovian limit as:

$$\langle \partial_i \psi | \partial_j \psi \rangle \dot{X}_j = -i \langle \partial_i \psi | \hat{H} | \psi \rangle - i \sum_n \langle \partial_i \psi | \hat{F}_n | \psi \rangle \eta_n(t) - i \sum_n \gamma \frac{d \langle \psi | \hat{F}_n | \psi \rangle}{dt} \langle \partial_i \psi | \hat{F}_n | \psi \rangle. \quad (4.1)$$

The terms on the left-hand side and the first term on the right constitute the conventional time-dependent variational principle (TDVP) equations (Section 1.2.3) [25] projecting the Schrödinger equation onto a variational manifold. The second and third terms on the right are the noise and friction due to coupling to the environment. \hat{F}_n are the operators by which the system is coupled to the bath displacement operators. We generally assume these to be spatially local.

For spin-half chains they are given by the x, y and z -components of the spin operators on each site, each of which couples to a separate bath. The bath is described as a collection of harmonic oscillators and the noise-correlator is determined by the spectrum of oscillators and the temperature of the bath. These are related by a fluctuation-dissipation relation, $\langle\langle\eta(t)\eta(t')\rangle\rangle = 2\gamma T\delta(t-t')$ in the combined classical and Markovian limits.

This approach to unravelling the density matrix evolution has some particularly attractive features. It can treat coupling to finite-temperature and non-Markovian environments, expanding the relevance of environment-induced many-body Zeno transitions. The TDVP Langevin equation can be used with any variational parametrisations in any dimension that permits a TDVP treatment in the absence of an environment. Consequently, the effects of long-range interactions in one dimension [100,101] can be readily incorporated. It lends itself particularly well for combination with stochastic TDVP evolution of neural quantum states [102–104].

In the present treatment we use one-dimensional matrix product states (MPS) [21, 105, 106]. To date, MPS techniques have been employed in the study of open systems largely by starting with the Lindblad master equation and either describing the density matrix directly as a matrix product operator [107–109] or else unravelling its evolution over MPS representations of quantum trajectories [110–112]. These approaches cannot treat finite temperature or non-Markovian environments for which alternative methods are required [113].

We provide a heuristic derivation and Keldysh field theory derivation of Eq.(4.1) in the following section. We develop the Langevin equation from the Keldysh path integral for the time-evolution of the density matrix. The method follows that of [114, 115] with the modification that the Keldysh path integral is constructed over matrix product states [28].

The result adds noise and friction to the time-dependent variational principle constructed over matrix product states [25]. The same construction for other variational classes leads to a similar stochastic equation of motion, which we dub the TDVP-Langevin equation. Alternative unravellings of the Lindblad equation for the density matrix evolution over MPS [110] apply in different circumstances of relative time and energy scales of the bath and system.

The construction over MPS of Eq.(4.1) follows the prescription for TDVP seen in [25], which we detail in the numerical implementation section. Integration of this equation is made complicated by the friction term. Naively, this requires inversion of a matrix that is proportional to the system size and dimension of the variational manifold. However, recognising that it consists of an outer product of vectors allows an efficient inversion and integration of the equations of motion.

In later sections we also show that thermal distributions are fixed points of the TDVP Langevin evolution. A thermal distribution is given by a Boltzmann-weighted Haar average over the variational manifold. For MPS of bond dimension D , this average can be performed as a Haar integral over the group $SU(dD)$ with d the local Hilbert space dimension.

The bath model

Approaches to studying open systems that involve writing down an effective equation of motion for the reduced density matrix, i.e. a Markovian or non-Markovian quantum master equations, can be highly efficient but do not allow any access to the environmental degrees of freedom. In this work we consider a paradigmatic model of the dissipative dynamics of the environment, the Caldeira-Leggett model [32].

We model the bath as a collection of independent non-interacting harmonic oscillators. These are linearly coupled to local system operators \hat{F}_n at site n by their displacements. The bath and interaction Hamiltonians are given by,

$$\hat{H}_B = \sum_n \sum_\alpha \hbar \omega_\alpha (\hat{a}_{n,\alpha}^\dagger \hat{a}_{n,\alpha} + \frac{1}{2}) \quad (4.2)$$

$$\hat{H}_I = - \sum_n \sum_\alpha \lambda_\alpha (\hat{a}_{n,\alpha}^\dagger + \hat{a}_{n,\alpha}) \hat{F}_n \quad (4.3)$$

where the index α labels the different oscillator modes at the site n .

The distribution and temperature of the oscillator modes is assumed to be the same at each site. Further, we assume no back reaction of the system on the bath – as seen by the exclusion of an extra counter term [116,117]. The counter term accounts for frequency shifts so that the system Hamiltonian is the physically observable Hamiltonian, and can formally be absorbed into the system.

The assumption we make is subtle – the bath must be non-linear in order to thermalise energy absorbed from the system, but these non-linearities must operate on timescales such that the bath's effect on the system is the same as independent oscillators. This allows noise and dissipation to be related by the fluctuation-dissipation relation. The assumptions are non-trivial, but standard, and permit the simple manipulations that follow.

A heuristic derivation

A heuristic derivation of the TDVP Langevin equation can be made in the spirit of the Frenkel principle for deriving the TDVP equations [9]. The state of the system and bath are parametrized as $|\psi(\mathbf{x})\rangle \otimes_{n,\alpha} |\phi_{n,\alpha}\rangle$, where \mathbf{x} corresponds to some set of variational parameters of the system and $\phi_{n,\alpha}$ are coherent state parameters of the α -oscillator on site n .

The time derivative of the wavefunction in the Schrödinger equation for the system and bath is expanded using chain rule over these parameters,

$$-i\hat{H}|\psi\rangle \otimes_{n,\alpha} |\phi_{n,\alpha}\rangle \approx \dot{\mathbf{z}} |\partial_{z_i}\psi\rangle \otimes_{n,\alpha} |\phi_{n,\alpha}\rangle + |\psi\rangle \sum_{m,\beta} \dot{\phi}_{m,\beta} \partial_{\phi_{m,\beta}} (\otimes_{n,\alpha} |\phi_{n,\alpha}\rangle) \quad (4.4)$$

where the inequality is because the dynamics might take the state outside of the variational manifold.

Taking an inner product with $\langle \partial_{z_i}\psi | \otimes_{n,\alpha} \langle \phi_{n,\alpha} |$ allows us to obtain an equation of motion for the system in the presence of the bath, while taking an inner product with $\langle \psi | \partial_{\phi_{o,\gamma}} (\otimes_{n,\alpha} \langle \phi_{n,\alpha} |$ allows us to obtain an equation of motion for the bath in the presence of the system, with system Hamiltonian H_S ,

$$i\langle \partial_{z_i}\psi | \partial_{z_j}\psi \rangle \dot{z}_j = \langle \partial_{z_i}\psi | \hat{H}_S | \psi \rangle + \sum_n \langle \partial_{z_i}\psi | \hat{F}_n | \psi \rangle \sum_\alpha \lambda_\alpha (\bar{\phi}_{n,\alpha}(t) + \phi_{n,\alpha}(t)) \quad (4.5)$$

$$i\dot{\phi}_{n,\alpha} = \omega_\alpha + \lambda_\alpha \langle \psi | \hat{F}_n | \psi \rangle \quad (4.6)$$

The equalities are attained since the inner products with the tangent vectors project the Hamiltonian evolution back onto the variational manifold. These equations correspond to the usual TDVP equations with addition of terms coupling between the system and bath.

The remaining steps involve integrating the equation of motion for the bath degrees of freedom and substituting back into the equation of motion for the system. The formal solution of the equation of motion of the bath degrees of freedom is

$$\phi_{n,\alpha}(t) = \phi_{n,\alpha}(0)e^{-i\omega_\alpha t} - \int_0^\infty dt' D^R(t' - t) \langle \psi | \hat{F}_n | \psi \rangle, \quad (4.7)$$

where we have identified the retarded bath correlator $D^R(t' - t) = -i\Theta(t - t') \langle \hat{a}^\dagger(t') \hat{a}(t) \rangle = ie^{i\omega(t' - t)}$. The assumptions of no back reaction of the system on the bath lies in treating the terms $\eta_n(t) = \sum_\alpha \phi_{n,\alpha}(0)e^{-i\omega_\alpha t}$ as a stochastic random field with variance appropriate to the thermal distribution. After further identifying $\partial_t \Gamma(t) = D^R(t)$ the equation of motion is of the form,

$$i \langle \partial_{A_i} \psi | \partial_{A_j} \psi \rangle \dot{A}_j = \langle \partial_{A_i} \psi | \hat{H}_S | \psi \rangle + \sum_n \langle \partial_{A_i} \psi | \hat{F}_n | \psi \rangle \left(\int dt' \Gamma(t - t') \langle \partial_{A_j} \psi | \hat{F}_n | \psi \rangle \dot{A}_j + \eta(t) \right). \quad (4.8)$$

Correlations in the noise fields $\eta(t)$ relate to the dissipation kernel $\Gamma(t - t')$ by fluctuation-dissipation theorem. The Markovian limit, $\Gamma(t - t') = \Gamma\delta(t - t')$, recovers Eq. 4.1.

Keldysh field theory derivation

A formal derivation from the Keldysh path integral can also be made. We follow the approach described in [33, 114, 118] of constructing a Keldysh path integral for the density matrix and then integrating out the bath in an appropriate limit to obtain a Langevin equation. Our main modification is to construct the path integral over MPS following [28].

The initial density matrix is assumed to factorise into density matrices for the system and bath as $\hat{\rho} \otimes \hat{\rho}_{bath}$ - the bath being in thermal equilibrium and its distribution assumed to be unchanged in time. This evolves to $\bar{T} e^{-i \int_0^t dt' (\hat{H} + \hat{H}_{int} + \hat{H}_{bath})} \hat{\rho} \otimes \hat{\rho}_{bath} T e^{-i \int_0^t dt' (\hat{H} + \hat{H}_{int} + \hat{H}_{bath})}$ at time t .

Construction of the Keldysh path integral proceeds by dividing up the time-ordered (T) and anti-time-ordered (\bar{T}) exponentials into many infinitesimal evolutions, and inserting resolutions of the identity over coherent state variables for the bath and using a Haar measure over MPS states for the system [28].

$$\mathbf{1} = \int \prod_n d\bar{\phi}_n(t) d\phi_n(t) e^{-\sum_n \bar{\phi}_n \phi_n} \otimes_n |\bar{\phi}_n\rangle \langle \phi_n| \quad (4.9)$$

$$= \int DA(t) |A\rangle \langle A| \quad (4.10)$$

Here DA symbolises an integral over all tensors in the MPS chain over the Haar measure, as introduced in [28].

A Keldysh rotation transforms from the fields on the time-ordered contour (+) and the anti time-ordered contour (−) to the sum and difference between them, $A^\pm = A^{cl} \pm A^q$, $\phi^\pm = \phi^{cl} \pm \phi^q$ – known as the classical and quantum components of the quantum field. These manipulations give the following path integral for the evolution kernel of the density matrix:

$$K(t) = \int DAD(\bar{\phi}, \phi) e^{S[A^c, A^q, \phi^c, \phi^q]} \quad (4.11)$$

$$S = S[A^{cl} + A^q] - S[A^{cl} - A^q] + \int dt \left[\sum_{n,\alpha} \lambda_\alpha \left(F_n^q, F_n^{cl} \right) \begin{pmatrix} \phi_{n,\alpha}^{cl} + \bar{\phi}_{n,\alpha}^{cl} \\ \phi_{n,\alpha}^q + \bar{\phi}_{n,\alpha}^q \end{pmatrix} \right] \quad (4.12)$$

$$+ \int dt dt' \left[\sum_{n,\alpha} \left(\bar{\phi}_{n,\alpha}^{cl}(t), \bar{\phi}_{n,\alpha}^q(t) \right) \begin{pmatrix} 0 & [D_\alpha^A]^{-1}(t-t') \\ [D_\alpha^R]^{-1}(t-t') & [D_\alpha^-]^{-1}(t-t') \end{pmatrix} \begin{pmatrix} \phi_{n,\alpha}^{cl}(t') \\ \phi_{n,\alpha}^q(t') \end{pmatrix} \right]$$

where D_α^A , D_α^R and D_α^K are the advanced, retarded and Keldysh components of the bath Greens function. Consistent with our assumption of a thermal equilibrium bath and no back reaction, they are related by the fluctuation dissipation relation: $D_\alpha^K(\omega) = \coth(\omega/2T)[D_\alpha^R(\omega) - D_\alpha^A(\omega)]$ with $D^{R(A)} = 1/(\omega \pm i\delta)$. Furthermore, $S[A]$ is the action of the system in the absence of coupling to the bath.

The simple quadratic form of the bath action follows from our assumptions and modelling of its effects as independent harmonic oscillators. This allows for integrating out the bath and, depending upon timescales [119], to construct either a Lindblad or Langevin limit.

We construct the latter limit in three steps. First the bath degrees of freedom are integrated out. The resulting dissipative contribution to the action has cross terms between classical and quantum components of the expectations of \hat{F} , and a term quadratic in the quantum component,

$$S_{diss} = \int dt dt' \sum_n \left(F_n^{cl}, F_n^q \right) (t) \begin{pmatrix} 0 & D^A(t-t') \\ D^R(t-t') & D^K(t-t') \end{pmatrix} \begin{pmatrix} F_n^{cl} \\ F_n^q \end{pmatrix} (t'), \quad (4.13)$$

where the bath propagators without indices indicate a sum over all modes, for example $D^R = \sum_\alpha \lambda_\alpha^2 D_\alpha^R$. The quadratic term in F^q is decoupled with a Hubbard-Stratonovich field $\eta(t)$ that will ultimately play the role of the stochastic noise field in Eq.4.1.

The final trick to bring this integral to the Langevin form is to Taylor expand the action to linear order in the quantum fields, A^q . The result is a path integral over the MPS tensors A^q and A^{cl} and the noise field η :

$$K(t) = \int \mathcal{D}A^q \mathcal{D}A^{cl} \mathcal{D}\eta e^{iS[A^c, A^q, \eta]} \quad (4.14)$$

$$\begin{aligned} S = & \int dt \sum_n A_n^q(t) \dots \\ & \times \underbrace{\left[2\delta S[A^{cl}] / \delta A_n^{cl}(t) + 2 \sum_m \partial F_m^{cl} / \partial A_n^{cl}(t) \left(\int dt' D^R(t-t') F_m^{cl}(t') + \eta_m(t) \right) \right]}_{\text{Eq.(1)}} \\ & - \int dt dt' \sum_n \eta_n(t) [D^K]^{-1}(t-t') \eta_n(t'). \end{aligned} \quad (4.15)$$

This is equivalent to the TDVP Langevin of Eq.(4.8). The quantum field A^q plays the role of a Lagrange multiplier that imposes Eq.(4.8) and the remaining term gives the bath correlations. The tensor indices have been suppressed for clarity in this expression. To make the comparison with the TDVP-Langevin equation, note that when $\delta S[A^{cl}] / \delta A_n^{cl}(t) = 0$ recovers the usual TDVP equations for matrix product states. The additional terms correspond to the dissipative effects of the bath. These terms are non-local in the chain indices n and m , despite our model of local independent baths.

This is due to the potential long-ranged entanglement of the matrix product state. The long-range effects of the noise term reflect those already found in the usual TDVP equations, since the noise term arises from a random local potential. The non-locality of the friction term is more problematic and some insight is required to implement this efficiently. This is discussed when we outline the numerical implementation of this in Sec. 4.2.1

4.2.1 Numerical implementation

Here we outline how the TDVP-Langevin equation, Eq.(4.1), can be implemented numerically for matrix product states (MPS). This work was performed by Andrew Hallam, and we highlight the steps taken here. As we have seen, this equation comprises three parts. The first of these is the closed-system TDVP equation, which is implemented by standard means [25].

The second and third terms incorporate the effects of the environment, and are the random noise induced by the environment and the friction respectively. The noise term is essentially a time-dependent Hamiltonian term, which we integrate in a Stratonovich scheme. The friction term requires more care as even in the Markovian limit, it is generally spatially non-local. A significant simplification can be achieved by working with purely local operators.

The TDVP equations for MPS can be written in the form

$$\begin{aligned} \langle \partial_i \psi | \partial_j \psi \rangle \dot{X}_j &= -i \langle \partial_i \psi | \hat{H} | \psi \rangle \\ \Rightarrow \langle \partial_{A_n} \psi | \partial_{A_m} \psi \rangle \dot{A}_m &= -i \langle \partial_{A_n} \psi | \hat{H} | \psi \rangle \end{aligned} \quad (4.16)$$

where the variational parametrisation with complex parameters $\{X_i\}$ are MPS, $\{A_i\}$, with tensor indices suppressed and retaining only the site index for clarity.

The solution of this equation is well established. A sensible choice of gauge fixing for the tangent vectors to the MPS manifold puts the Gram matrix $\langle \partial_{A_n} \psi | \partial_{A_m} \psi \rangle$ in a diagonal form. Many algorithms exist for evaluating the TDVP equations for finite systems, in this work we use a modification of the method introduced in [27].

A single time-step of the algorithm consists of sweeping through the system from right to left and applying a unitary rotation to the local variables on each site, $A_n(t + \delta t) = e^{iH_{eff}} A_n(t)$, followed by a repetition of this process by sweeping from left to right.

The Noise contribution to the TDVP Langevin equation over MPS can be written in the form

$$-i \sum_m \langle \partial_i \psi | \hat{F}_m | \psi \rangle \eta(t) \Rightarrow -i \sum_m \langle \partial_{A_n} \psi | \hat{F}_m | \psi \rangle \eta_m(t) \quad (4.17)$$

As can be seen, this takes the same form as the right hand side of Eq.(4.16), so no substantial modification to the TDVP algorithm is required. At the beginning of

each timestep δt , $\eta_m(t)$ is chosen by sampling from a normal distribution with mean zero and variance $2\delta t\gamma T$.

Finally, the friction term is computed as follows. In the Markovian limit and in terms of the MPS tensors, the friction term can be written as follows,

$$-i \sum_m \gamma \frac{\langle \psi | \hat{F}_m | \psi \rangle}{dt} \langle \partial_i \psi | \hat{F}_m | \psi \rangle, \quad (4.18)$$

where,

$$\frac{\langle \psi | \hat{F}_m | \psi \rangle}{dt} = \langle \psi | \hat{F}_m | \partial_{A_n} \psi \rangle \dot{A}_n + \langle \partial_{\bar{A}_n} \psi | \hat{F}_m | \psi \rangle \dot{\bar{A}}_n. \quad (4.19)$$

This equation, (4.19), can be evaluated by substituting in Eq.(4.16), the TDVP equations. In the following manipulations we introduce the poisson bracket notation, $\{O_1, O_2\} = i \langle \psi | \hat{O}_1 | \partial_{A_n} \psi \rangle \langle \partial_{\bar{A}_n} \psi | \hat{O}_2 | \psi \rangle - i \langle \psi | \hat{O}_2 | \partial_{A_n} \psi \rangle \langle \partial_{\bar{A}_n} \psi | \hat{O}_1 | \psi \rangle$,

$$\begin{aligned} (\delta_{m,n} + \sum_n \gamma \{F_m, F_n\}) \frac{\langle \psi | \hat{F}_n | \psi \rangle}{dt} &= \{F_m, H\} + \sum_n \{F_m, F_n\} \eta_n(t) \\ \rightarrow \frac{\langle \psi | \hat{F}_n | \psi \rangle}{dt} &= (\mathbf{1} + \gamma F)^{-1} \left(\{F_m, H\} + \sum_n \{F_m, F_n\} \eta_n(t) \right) \end{aligned} \quad (4.20)$$

where $F_{ij} = \{F_i, F_j\}$. Evaluating Eq.(4.20) exactly for arbitrary operators \hat{F}_n is generally numerically inefficient, scaling quadratically in the number of noise operators. Moreover, it is inconsistent with the site-by-site sweep algorithm introduced above for the TDVP equations.

Fortunately, Eq.(4.20) is substantially simplified in the case of single-site, local noise fields. For local fields $\{F_i, F_j\}$ is non-zero provided the two operators are located on the same site of the system. Thus F becomes a simple, block diagonal matrix, which is numerically efficient to invert.

Combining this, the modified TDVP algorithm works as follows: Before each sweep through the system $\eta_m(t)$ is sampled from a normal distribution with mean 0 and variance $2\delta t\gamma T$. The Hamiltonian and noise terms are then used to calculate $\frac{\langle \psi | \hat{F}_n | \psi \rangle}{dt}$ for all noise operators F_n using Eq.(4.20). The noise and friction terms combine with the Hamiltonian using Eq.(4.16) and the state is evolved using the standard TDVP algorithm.

4.2.2 Thermal distributions are fixed points

Here we show that thermal distributions are fixed points of the TDVP Langevin evolution. This is something that we would expect of the TDVP-Langevin equation as realised in our numerical implementation. We show how this is consistent for the one and two spin cases through calculation.

In the left canonical form, MPS of left bond order D and local Hilbert space dimension d are given by $SU(dD)$ isometries [105]. In the case of a finite chain of length L , the left bond order at the n^{th} site $D_n = d^n$ up to the maximum bond order at site $n = \log_d D_{\text{max}}$. The bond order remains D_{max} up to site $L - 1 + \log_d D_{\text{max}}$ beyond which it reduces as $D_n = d^{(n-L+1)}$.

The thermal expectation of an operator can be calculated by a Boltzmann-weighted Haar average over this variational manifold. The average of an operator \hat{O} is given by

$$\langle\langle \hat{O} \rangle\rangle = \frac{\int \prod_n DA_n \langle \phi | \hat{O} | \phi \rangle \exp[-\beta \langle \phi | \hat{H} | \phi \rangle]}{\int \prod_n DA_n \exp[-\beta \langle \phi | \hat{H} | \phi \rangle]}. \quad (4.21)$$

The expectation of the Hamiltonian $\langle \phi | \hat{H} | \phi \rangle$ and the operator $\langle \phi | \hat{O} | \phi \rangle$ are calculated by usual MPS techniques. In practice, we carry out the integrals by sampling a Haar random distribution of isometric MPS tensors; $A_{ij}^\sigma \equiv U_{i \otimes \sigma, j \otimes 1} \in SU(dD_n)$. These are obtained by a QR decomposition of a tensor with elements drawn randomly from a normal distribution.

Fig. 4.1 shows this Boltzmann-weighted Haar distribution as a function of energy at different temperatures. These thermal distributions are fixed-points of the dynamics described by Eq.(4.1). We show for the example of temperature $T = 0.1$ that the energy distribution remains as time evolves.

Example: one spin

For the example of a single spin we can write a Langevin equation and we can calculate the expectation of the Hamiltonian explicitly. The fixed point for both of these is a thermal diffusion over phase space.

For one-spin, we parametrise on the Bloch sphere, L , with the spin coherent state $|\psi\rangle = |L\rangle$, such that $L^2 = 1$. Under the Hamiltonian $H = B\sigma^z$, we want to compute

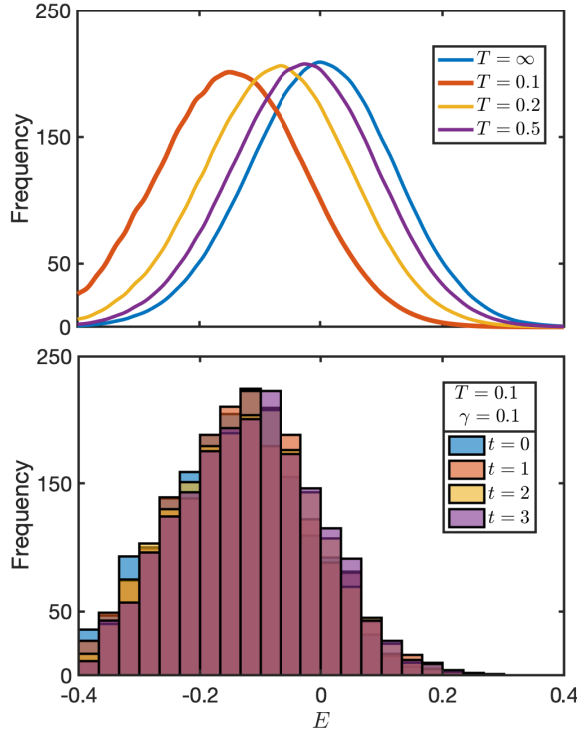


Figure 4.1: Distribution of energies of states at finite-temperature for length 15 chain at bond order $D_{\max} = 2$: a) The density of occupied states is computed for the Hamiltonian studied in this work (introduced here later Eq. (4.24)), $H =$ with $J = 1$ $g = -1.05$, and $h = 0.5$ from a sample of Haar random distributed isometric MPS initial states. At $T = \infty$ – an unweighted Haar average, the majority of the states are in the middle of the spectrum and are highly entangled. A Boltzmann weight shifts this distribution to lower energy. Low-entanglement states are a subset of measure zero in the thermodynamic limit. b) The Boltzmann-weighted Haar average is a fixed point of the TDVP-Langevin equation. Here we compare distributions obtained after evolving with the Hamiltonian for $t = 1, 2$, and 3 , with $\gamma = 0.1$ and $T = 0.1$. The distribution for $T = 0.1$ is shown in bold in a), we see the Langevin evolution preserves this distribution.

$\langle H \rangle$ exactly and using the Langevin equation. The exact calculation is as follows,

$$\langle H \rangle = \frac{\sum_{\sigma} \langle \sigma | H | \sigma \rangle e^{-\beta H}}{\sum_{\sigma} e^{-\beta H}} = \frac{B(e^{B\beta} - e^{-B\beta})}{e^{B\beta} + e^{-B\beta}} = B \tanh B\beta. \quad (4.22)$$

Compared to using the Langevin equation, with $d\underline{l} = \sin\theta d\theta d\phi$,

$$\begin{aligned} \langle H \rangle &= \frac{\int d\underline{l} B l^z e^{-\beta l^z B}}{\int d\underline{l} e^{-\beta l^z B}} \\ &= \frac{\int d\theta \sin\theta \cos\theta B e^{-\beta B \cos\theta}}{\int d\theta \sin\theta e^{-\beta B \cos\theta}} \\ &= \frac{-B}{\beta} \frac{1}{\beta B} \frac{\partial_B \cosh \beta B}{\cosh \beta B} = B \tanh B\beta. \end{aligned} \quad (4.23)$$

4.3 Environment induced transitions in entanglement dynamics

We now move onto applying this technique to investigate environment induced phase transitions. For a given Hamiltonian, we find that as the strength of the coupling to and temperature of the environment is increased, there is a transition into a many-body Zeno phase where the bond dimension necessary to describe the dynamics is capped to be below the system size. As the bath strength increases, the entanglement in the system saturates at a lower value, and states evolve to have a high fidelity with lower bond-dimension simulations.

To begin, we should ask what environment or *measurement* induced transitions in entanglement dynamics are. Measurement induced phase transitions where thermalisation and volume law entanglement growth is inhibited by random measurements leading to non-unitary time evolution was first seen as an entanglement transition in [35,76,80]. In the introduction (Sec. 4.3.2) we define scaling of entanglement, its characterisation can be volume law, subextensive, or area law.

The competition between Hamiltonian dynamics that brings about entanglement growth and local measurement causing entanglement saturation. If g is the coefficient of number of measurements in time over number of unitaries applied in time, $g = \frac{\# \text{ measurements}}{\# \text{ unitaries}}$, there is a critical g_c , beyond which measurements impede entanglement growth.

This setting involves random unitary gates punctuated with projective measurements. This ‘entangling’ to ‘disentangling’ [35] transition has since been seen in random Clifford circuits [36,37,120] and monitored free fermions [97,121]. The question of whether this type of phenomena survives in open quantum circuits, i.e. circuits as we have described but in the presence of realistic decoherence processes, has also been explored [122]. Bypassing the quantum circuit altogether, similar analyses extend to open Hamiltonian systems [94–97,121].

Here we have the tools to ask whether such transitions occur in open Hamiltonian systems in the presence of decoherence and finite-temperature environments. We look at applying the TDVP-Langevin equation to a chaotic Hamiltonian system and look at how entanglement entropy and fidelity of our system state behaves in

different regions of phase space. Environmental parameters that we have available to us are temperature T , friction γ , and noise γT and in the following we explore different limits of phase space. Note, these are not independent parameters as can be seen in the labelling of their variables.

In the absence of coupling to a bath, TDVP equations eventually fail as the entanglement grows beyond that which can be represented on the variational manifold¹. However, just as observed in projective measurements of random circuits, the effects of the environment may restrict the growth of entanglement.

In extremis this might limit entanglement of individual trajectories so that they can be represented on low dimensional variational manifolds. The TDVP Langevin equation will then give a good account of the dynamics at all times, signifying a transition in its classical representability. This is our interpretation of the sequence of results presented in this section.

This key result is summarised in Fig. 4.2 for the specific example of the model we consider, which captures the dynamics of the von Neumann entanglement entropy. We show this figure before introducing the specific model to make clear the basic properties of MPS Langevin evolution. The general shape and behaviour of these trajectories is interesting here and is general.

For temperature fixed at a certain value $T = 0.2$, there is a transition in entanglement dynamics beyond a critical value, $\gamma T \approx 0.11$. The saturation entanglement becoming intrinsic to the interplay between the Hamiltonian and the dissipative bath, rather than by the choice of variational manifold. We detail these results in the following section alongside similar transitions that occur when friction, γ , or noise, γT are kept constant.

¹TDVP equations for the thermofield purification of the density matrix may escape this fate [98] at least as far as local observations are concerned

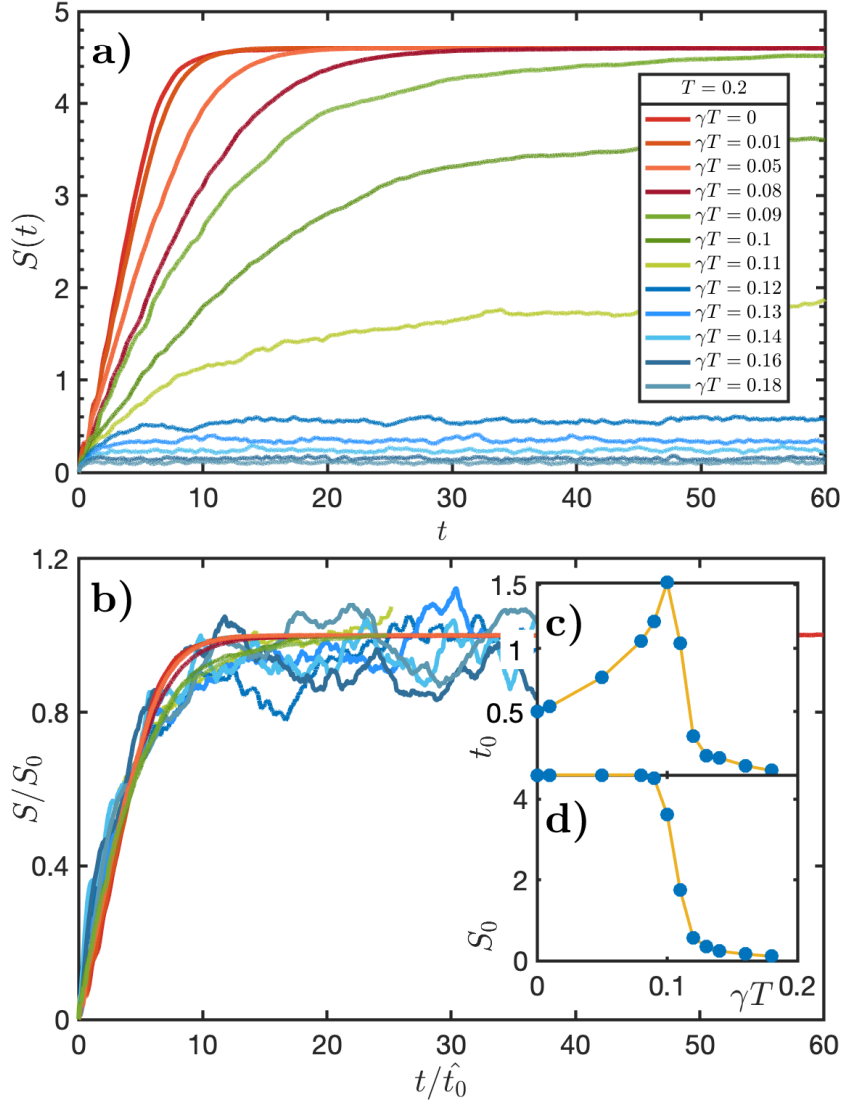


Figure 4.2: *Basic Properties of MPS Langevin Evolution:* The TDVP Langevin equation, Eq.(4.1) describes the evolution of the density matrix through an ensemble of stochastic pure-state trajectories. a) *von Neumann entropy as a function of time* averaged over 70 trajectories at different coupling strengths. Temperature is fixed at $T = 0.2$, while friction, γ (and therefore noise, γT) is varied. Simulations were carried out at bond dimension $D = 128$. Three different regimes of behaviour are apparent: an initial transient, followed by an approximately linear-in- t growth, and finally a saturation. At low values of γ this saturation is determined by the variational approximation. At high values it is determined intrinsically by the interplay of the Hamiltonian and the dissipative bath. It signals whether a lower bond-dimension (hence less computationally intensive) simulation suffices in to capture the entropy dynamics. b) *Scaling collapse* of the data shown in a). Amplitudes and timescales are rescaled by factors of S_0 and t_0 , respectively (Fits to $S(t) = S_0 \tanh(t/t_0)$ are used as a guide to this rescaling). These are plotted *versus* γT in the insets c) and d), which show clear evidence of a transition at around $\gamma T \approx 0.11$, beyond which the saturation entanglement is determined by balance between entangling effects of the Hamiltonian and environmental dissipation.

4.3.1 Results for tilted field Ising model

The Hamiltonian that we consider is the tilted field Ising model

$$\hat{H} = - \sum_i [J\sigma_i^z\sigma_{i+1}^z + h\sigma_i^z + g\sigma_i^x], \quad (4.24)$$

with $J = 1$, $g = -1.05$ and $h = 0.5$. With these parameters, the Hamiltonian is far from any integrable point and rapidly thermalising [26, 123].

Infinite temperature and vanishing friction

Fig.4.3a shows the variation in von Neumann entanglement across the central bond as a function of time for simulations with range of noise strengths. The simulations are carried out at bond order $D = 160$, which sufficiently fully captures the Hilbert space at this system size.

The broad result of these simulations is that the entanglement saturates at long times at a value determined by the system size. This is consistent with an infinite temperature final state with the maximum entanglement supported by the variational manifold. The most interesting aspect of these results is the decreasing rate of early-time entanglement growth with increasing noise strength. Crucially we do not find evidence of an intrinsic saturation of entanglement – only that dictated by the limitations of the variational approximation.

Fig. 4.3b shows the collapse of these data after rescaling time by a factor t_0 (obtained by fitting to the function $S(t) = S_0 \tanh(t/t_0)$, fitting is discussed further in Sec. 4.3.2). The saturation entanglement $S_0 \approx 4.6$ is the same for all noise strengths. Fig.4.3c shows the saturation time t_0 obtained in this way. This fitting is very good beyond $\gamma T = 0.15$. Beyond this coupling strength, the dynamics are similar to random unitary circuits with conservation laws [77, 124]. Indeed, setting the external fields in Eq.4.24 to zero generates the same dynamics.

Finite temperature and friction

Including both noise and friction, we see a transition into a many-body Zeno phase in which entanglement saturates. This is demonstrated in two ways; by considering the saturation of entanglement at long times and by a high fidelity between low- and high-bond order simulations at long times.

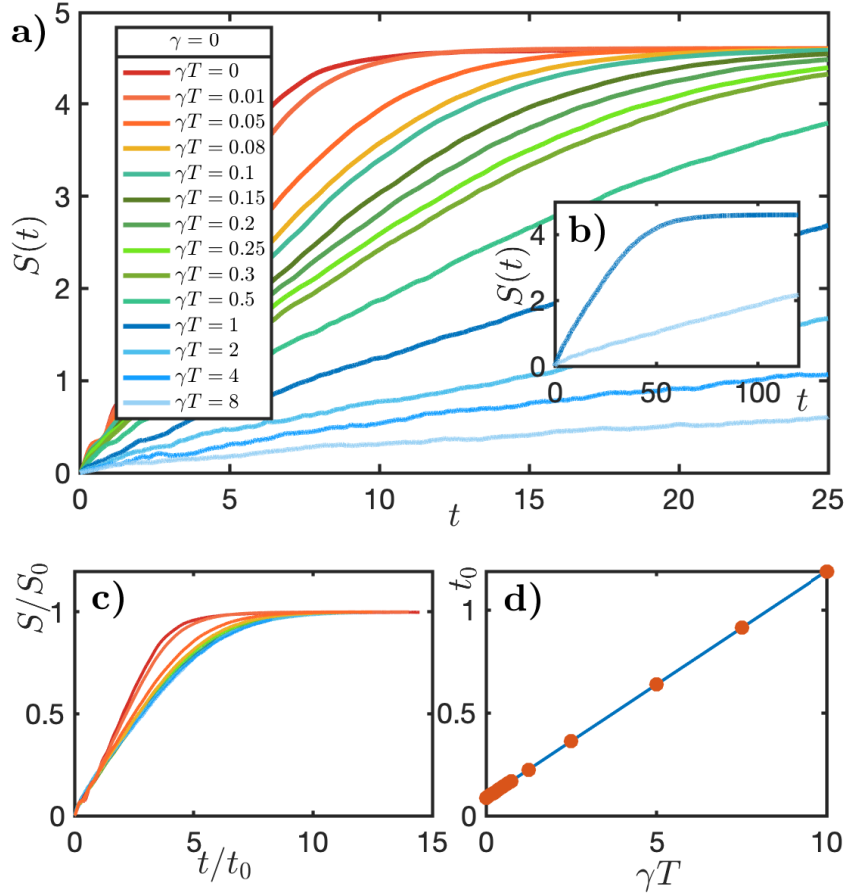


Figure 4.3: Evolution of Entanglement at Infinite Temperature: a) von Neumann entropy versus time for different values of γT with $\gamma = 0$ (infinite temperature). Analogous to Fig. 4.2, after an initial transient, the entanglement grows linearly with time before saturating at a value determined by the MPS manifold (here with $D = 160$). The rate of entanglement growth reduces with increasing noise γT due to dephasing effects of the bath. Unlike the finite temperature and friction case in Fig. 4.2 all curves saturate to the same entanglement. We anticipate that in the absence of restrictions imposed by the system size and/or choice of variational manifold the entanglement would continue to grow linearly in time. b) Saturation of entanglement for higher γT curves illustrated by extending the simulations to $t = 120$. c) Rescaling the time coordinate of the data by a factor t_0 collapses the data onto a single curve (Fitting to a function $S(t) = S_0 \tanh t/t_0$ is used to extract the rescaling factors. The scaling is remarkably good beyond $\gamma T = 0.15$. d) Timescales extracted in this way show a linear dependence upon noise γT .

This transition is evident in the entanglement entropy data for fixed $T = 0.2$, shown in Fig.4.2, where increasing coupling strengths causes reduced saturation entanglement. This transition can also be observed in different cuts through the noise-friction ($\gamma - \gamma T$) plane, where analogous plots to Fig. 4.2 is presented in Sec. 4.3.2.

(1) *Saturating entanglement*: In order to demonstrate this, in Fig. 4.4 we plot the long-time average of the von-Neumann entropy, \bar{S} . The simulations are carried out for a time 60 (in units of J) and averaged over the time interval 50-60.

The typical time-dependence from which such saturation values are computed is shown in Fig.4.2a. For low noise and friction, the saturation is determined by the limitations of the variational manifold. Panels a), b) and c) show \bar{S} as a function of γT at fixed γ , T at fixed γ , and γT at fixed γ , respectively. A threshold is reached for each bond dimension where it adequately captures the saturation entanglement, thus indicating a transition to increasingly classically simulatable dynamics.

The transition can be seen from the point where the trajectories obtained at different bond dimensions give the same saturation entanglement. From this we can extract a critical γ or γT as a function of bond dimension that we show in the insets. Note that since these data show the entanglement averaged over time 50-60, in some cases the saturation entanglement has not yet been reached. The transition is therefore expected to be slightly sharper than that shown in the figures. Compare for example Fig. 4.2d with Fig. 4.4a.

(2) *Fidelity as $t \rightarrow \infty$* : We can identify an analogous transition in the fidelity of each trajectory at different bond dimensions *versus* a reference trajectory with bond dimension $D = 128$. In this case, we find that beyond a critical combination of γ or γT , the fidelity of the state at low bond dimension remains close to 1 for long times.

We expand upon this result in Fig. 4.5, where we identify a divergent classical simulation time. We note that the fidelity is more sensitive to the time-step as friction is increased – an issue typical of numerical integration of systems of stochastic differential equations. This makes accessing the critical point of the transition numerically intensive for the parameters and Hamiltonian we consider. The entropy is less sensitive to this.

4.3.2 Scaling functions and features of open Langevin evolution

As we have shown, in order to investigate the entanglement dynamics that arise in the open evolution, we study the parameter space of the TDVP Langevin equations.

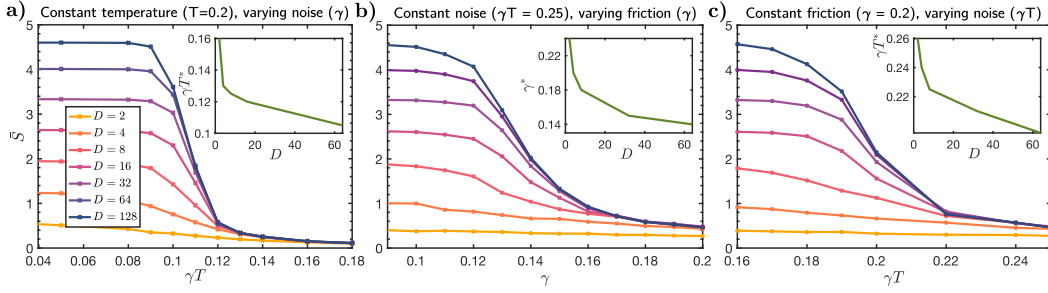


Figure 4.4: *Evolution of Saturation Entanglement at Finite Temperature:* In the main figures we show the dependence of the von Neumann entropy as a function of noise and friction: a) *versus* γT at fixed T , b) *versus* γ at fixed γT , c) *versus* γT at fixed γ . In each case, at low values of noise and friction, the saturation entanglement \bar{S} , is determined by the choice of variational parametrization through the bond order. As the noise and friction are increased, there is a cross-over where the saturation entanglement decreases from this value. Each bond dimension captures the saturation entanglement for a sufficiently large noise and friction. This is indicated when the entanglement begins to follow the entanglement given by the highest bond dimension simulation. At the transition, the saturation entanglement of the lower bond dimensions converges to that of the highest bond dimension. Beyond this point the saturation entanglement is determined intrinsically by the interplay between the Hamiltonian and the environment. In each corresponding inset figure, we have extracted critical dissipation strengths where these transitions occur as a function of bond dimension.

This is by keeping temperature, friction, and noise fixed, while varying either noise or friction. Fig. 4.2a) shows the basic properties of MPS Langevin evolution for the case of fixed temperature, where beyond a certain coupling strength the system enters a quantum Zeno phase. Fig. 4.6 shows analogous plots capturing the dynamics for the cases of fixed γT and γ .

Like the case of $T = 0.2$, the long time saturation of the entanglement can either be determined by the variational approximation (i.e. bond dimension) or intrinsically by the interplay of the Hamiltonian and the dissipative bath. In the accompanying figures, there are now two plots for the data collapse upon scaling. We also plot S_0 , the fitted entanglement saturation value and corresponding t_0 , defining the entanglement saturation time.

The fit to $S(t) = S_0 \tanh t/t_0$ is seen to be better before the transition, and unlike for fixed temperature, the fit to $S_0(1 - \exp(-t/t_0))$ is better after the transition – we plot these separately. For intermediate values of $\gamma, \gamma T$ we use both fits, since features of both sides of the transition appear. This is the source of the hysteresis in the plots for S_0 and t_0 . We have overlaid these plots for S_0 on the plots of \bar{S} in Fig. 4.7. This shows the range of approximate values for the saturation entanglement.

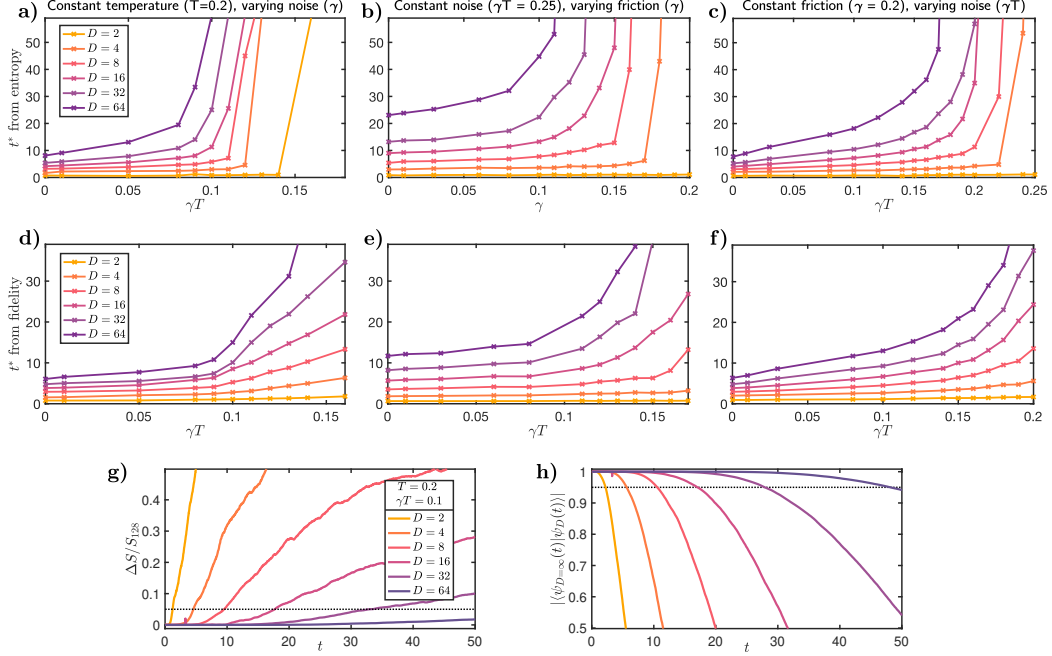


Figure 4.5: Divergent Classical Simulation Time: Simulations carried out at a bond order D give a good account of the system evolution up to a time $t^*(D)$. We extract these values versus a reference $D = 128$ simulation, which serves as the reference account of the system. We do this in two ways, by comparing the difference in von Neumann entanglement entropy between these states and the fidelity with this state. $t^*(D)$ is the time when the simulation with lower bond dimension deviates appreciably from the reference trajectory. The row with panels a), b), c), shows $t^*(D)$ extracted from the entropy, while panels d), e), f) shows $t^*(D)$ extracted from the fidelity. The fixed variables are split across the columns – a), d), shows varying γT at fixed $T = 0.2$, b), e) varying γ at fixed $\gamma T = 0.25$, and c), f) varying γT at fixed $\gamma = 0.2$. Panels g) and h) show typical evolution of entanglement and fidelity with time. These data are taken from the the trajectory with noise $\gamma T = 0.1$ which is close to the critical point for $T = 0.2$. A simulation is judged to have ceased to provide a good account of the system when the trajectory deviates beyond $\epsilon = 0.05$, and the time at which this occurs is $t^*(D)$. In g), this is the point where $\Delta S/S_{D=128} = |S_{D=128} - S_D|/S_{D=128} > \epsilon$. Analogously in h), $t^*(D)$ is the time when the fidelity is appreciably different from 1, i.e. $|\langle \psi_{D=128}(t) | \psi_D(t) \rangle| < 1 - \epsilon$. A divergent $t^*(D)$, within either method of extraction, indicates a transition in the classical simulability of the open quantum system.

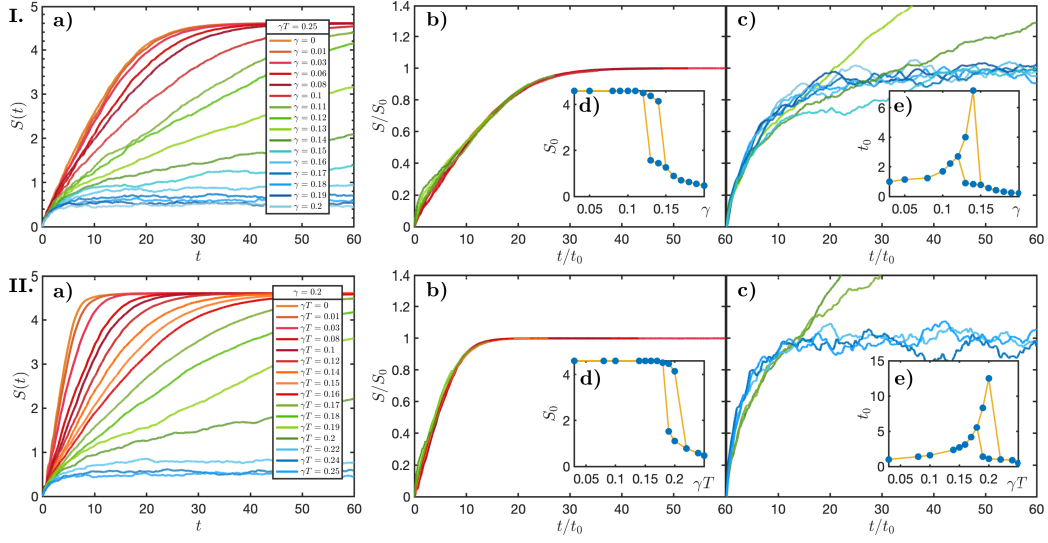


Figure 4.6: Many-body Zeno transition in the $\gamma - T$ plane. These results extend Fig. 4.2 of the main text a) Further values for the von Neumann entropy as a function of time are shown for averaged trajectories at different coupling strengths. In I. we have kept noise fixed with $\gamma T = 0.25$, while in II. we keep friction fixed with $\gamma = 0.2$. These simulations have bond dimension kept at $D = 128$ and serve as the reference case for the comparisons made against lower bond dimension simulations. Curves b) and c) show the data collapse from obtained by rescaling the amplitude by S_0 and the timescale by t_0 before and after the many-body Zeno transition, respectively following the procedure described in the text. A few curves near the transition show different early and late time behaviour leading to the apparent hysteresis in the plots of the extracted S_0 and t_0 shown in the insets d) and e) respectively.

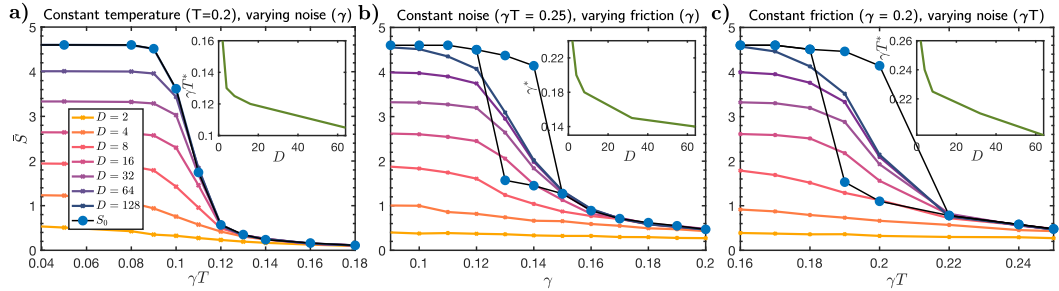


Figure 4.7: Evolution of Saturation Entanglement at Finite Temperature: Here we have shown Fig. 4.4 from the main text with curves for S_0 overlaid. a) In the case where T is kept fixed, the curve for S_0 is exactly the $D = 128$ simulation since clear entanglement saturation occurs. For fixed γT and γ the transition is less sharp. In figures b) and c) we have overlaid the curves for S_0 as seen in Fig. 4.6d. The lower curve shows the saturation entanglement post-Zeno phase, while the higher curve is pre-Zeno, i.e. the value of \bar{S} for non-critical curves that would then be attained given longer simulation time. The actual saturation is intermediate. This indicates a region of values the entanglement may saturate to, since it reflects an averaging of types of trajectory. Near to the many-body Zeno transition a few curves show different early- and late-time behaviour leading to an apparent hysteresis in S_0 .

For these intermediate trajectories, the tanh fitting describes their late time behaviour and the exp fitting the early time behaviour – explaining the trailing off of those trajectories in the fitting. A more detailed look at this observation follows. Identifying a critical point for the $D = 128$ data for fixed $T = 0.2$ (Fig. 4.2) is simple as it is where plateaus at lower values of entanglement are clearly seen, until entanglement in the system becomes distinctly very low.

Meanwhile, a feature that appears in the data for fixed γ and γT is a region of supposed slowed entanglement growth, a more ambiguous critical value, thus a region of intermediate behaviour. Furthermore, for certain *intermediate* trajectories, simulating for longer times could lead to attaining maximal saturation entanglement. Up to the times we simulate, a clear plateau has not emerged.

Taking a closer look, these ‘slowed’ trajectories are unlike the infinite temperature case where noise slows entanglement growth. These seem to evolve as though they are within the Zeno phase up to some time, where a random kick causes the entanglement to continue growing. This can be seen most clearly in Fig. (4.6.II.a), when $\gamma T = 0.19$. Up to time $t = 20$, this trajectory hints to saturating soon, until some kick, seen in the discontinuity or kink around this time, drives the entanglement to keep growing.

Looking at the individual trajectories that are then averaged over, it can be seen that this is not the slowing in entanglement growth as seen in the infinite temperature case (Fig. 4.3), rather the average of three types of behaviour. This is summarised in how we extract the different scaling coefficients for pre- and post-criticality also early and later time critical trajectories.

Our interpretation of these data is that the many-body Zeno transition confines trajectories to a low entanglement region of the variational manifold. Near the transition certain trajectories may have a very long dwell-time in this reduced entanglement phase before being kicked into the higher entanglement region. This might be termed a pre-Zeno plateau.

Extracting scaling coefficients

The essence of our scaling collapse shown in Fig. 4.2 and Supplementary Fig. 4.6 is to rescale entanglement by a factor of S_0 and timescales by a factor of t_0 . We

identify these factors by fitting to two analytical forms: either $S(t) = S_0 \tanh(t/t_0)$ or $S_0(1 - \exp(-1.4 t/t_0))$ (the factor of 1.4 in the latter gives approximately the same fitted t_0 with either function).

These functions are heuristics used to extract our scaling. In principle such a fit is not necessary, but we find it a good way to obtain our scaling. Moreover, the fits are actually rather good. Fig. 4.8 shows a typical fit to $S(t)$ averaged over trajectories. For data at constant temperature shown in Fig. 4.2, we find that the form $S(t) = S_0 \tanh(t/t_0)$ gives a reasonable fit both above and below the many-body Zeno transition.

In the cases of constant noise and constant friction, we find a slightly better fit using $S_0(1 - \exp(-1.4 t/t_0))$ in the many-body Zeno phase. Similar fits (to $\tanh(t/t_0)$) have been used in random unitary circuits [77, 124]. This can explain the quality of fit in the infinite-temperature/zero-friction case, with $\gamma T > 0.15$, where the dynamics are akin to random unitary circuit.

Typical fits: In Fig. 4.8b), we show a typical fitting to $S(t) = S_0 \tanh(t/t_0)$ for the case where $T = 0.2$ and $\gamma T = 0.1$. This trajectory is in the many-body Zeno phase as can be seen by the value of $S_0 = \bar{S} = 3.6$, which is less than the maximum value of 4.6 found in these simulations.

Pre-Zeno fits: As mentioned above, in the case of many-body Zeno transitions at constant noise or constant friction, we find that trajectories near the transition display early-time behaviour typical of the many-body Zeno phase crossing at early times over to a late-time behaviour typical of trajectories in which the environment does not restrict the entanglement growth.

Fig. 4.9 shows how we treat such trajectories. Panel b) shows averaged trajectories at $\gamma = 0.19$, $\gamma T = 0.25$ and $\gamma = 0.18$, $\gamma T = 0.25$ with fits to $S(t) = S_0 \tanh(t/t_0)$ at late times and to $S_0(1 - \exp(-1.4 t/t_0))$ early times. Panel a) shows 70 trajectories that are averaged to obtain the $\gamma = 0.19$, $\gamma T = 0.25$ results. It is from these individual trajectories that the underlying behaviour is one of apparent saturation to a many-body Zeno phase before a random kick from the leaving the low entanglement region of the manifold at some random time.

We also see that as the coupling strength increases, the region of time for which the exp fitting is valid increases, while the tanh fit decreases. This indicates how the

frequency of either type of trajectory changes as the coupling strength increases. Accordingly, for the case of fixed γ and γT , it is difficult to identify a point where the transition occurs.

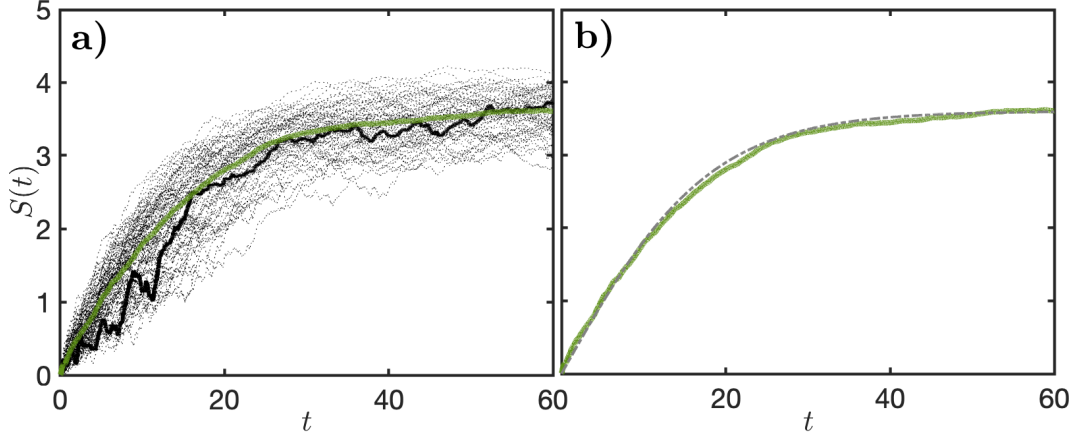


Figure 4.8: *Scaling fit to $S(t)$:* Here we show the fitting procedure used to determine S_0 and t_0 for our scaling collapse for the case fixed temperature and varying noise. a) Shows 70 trajectories for $T = 0.2$ and $\gamma T = 0.1$. For these parameters, the system is in the many-body Zeno phase. We highlighted a typical trajectory in bold and we have overlay the average of these trajectories as depicted in Fig. 4.2 in the main text. b) The dashed line shows the fitting $S(t) = S_0 \tanh(t/t_0)$ with $S_0 = \bar{S} = 3.6$ and $t_0 = 18$.

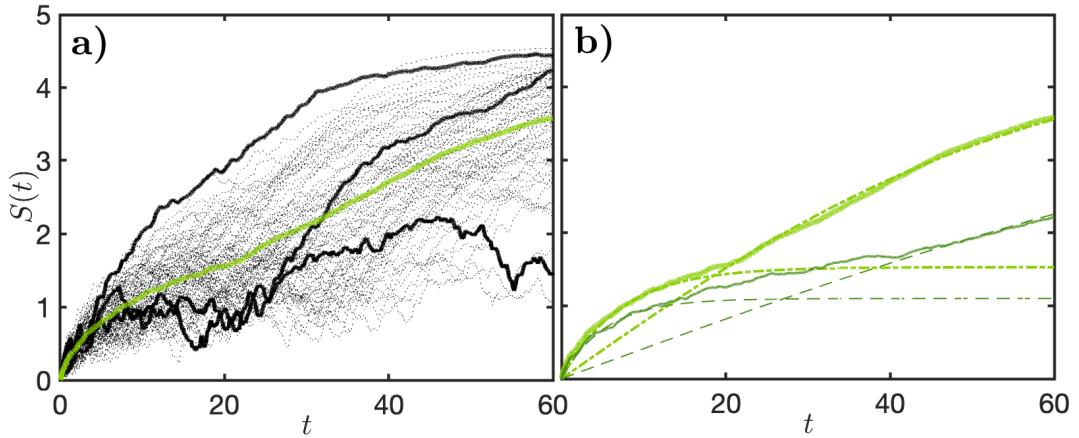


Figure 4.9: *Scaling fit for pre-Zeno Trajectories:* Here we show how scaling is determined for those trajectories near to the many-body Zeno transition that display different early- and late-time behaviour. a) 70 trajectories with $\gamma T = 0.14$ and $\gamma = 0.2$ together with the average trajectory shown in green. Individual trajectories show signs of saturation of entanglement which persists for a period of time before beginning to rise again. b) The average trajectory can be fit in two different ways at early and late times. Here we show these fits for trajectories $\gamma T = 0.14$ and $\gamma = 0.2$, and $\gamma T = 0.15$ and $\gamma = 0.2$ using $S_0(1 - \exp(-1.4 t/t_0))$ for early times and $S(t) = S_0 \tanh(t/t_0)$ for later times.

4.4 Limits on Classical Simulability

The TDVP Langevin equation cannot efficiently describe a system in the many-body Zeno phase, but the question remains of how tight this bound on simulation is. Can efficient methods of classical simulation be found that extend into the region that we have identified as the many-body Zeno phase?

As a system approaches thermalisation, it is more efficient to use a density matrix description, a variational representation of its purification [98], or a neural quantum state [125] than an unravelled description in terms of pure state trajectories. Indeed, these latter descriptions are efficient both at early times where entanglement is weak and at late times as thermalisation occurs [126–129]. Nevertheless, there are good grounds to believe that our bound on classical simulability is strong.

Our reasoning is that the complexity of open system quantum dynamics is non monotonic. In the generic case there is a large information/complexity barrier between efficient early- and late-time descriptions. The question of whether an efficient classical description is possible is essentially asking whether coupling to the environment suppresses this complexity barrier.

When a system is initially in an unentangled state then weakly coupled to a finite temperature bath, the early-time evolution is characterised by a growing complexity similar to growth of entanglement in the closed system. The TDVP-Langevin approach applies in this limit. Alternative approaches such as MPO representations of the density matrix or neural quantum states have similar (or higher) complexity in this limit.

At late times the complexity decreases as the system approaches thermalisation and ultimately a hydrodynamic description is appropriate. An MPO description of the density matrix is efficient in this limit. These considerations separate efficient early- and late-time descriptions of the system dynamics. Whilst we cannot preclude the existence of a more efficient early-time classical description than the TDVP Langevin description (or related unravellings of the Lindblad evolution at early times), we are not aware of any candidate.

We address the issue of classical simulability from the early time side of the complexity barrier where TDVP-Langevin evolution of matrix product states is appropriate – and where its efficiency is at least as good as alternative schemes.

This allows us to ascertain whether the complexity barrier has been suppressed by coupling to the environment.

MPO descriptions of the density matrix, MPS descriptions of its purification, or neural quantum states are efficient both in the early- and late-time limits. Such descriptions must still surmount the complexity barrier and their late-time efficiency does not help in this. Indeed, we anticipate that analyses using different variational parametrizations to determine whether the early-time growth of the complexity barrier is suppressed will yield similar results, notwithstanding the issue of their late-time efficiency.

What is the origin of this complexity barrier and how high is it? The peak in complexity emerges in the balance between the entangling effects of the system's Hamiltonian and the thermalising effects of the bath. We identify two timescales: i. the timescale at which entanglement saturates ($S_{sat} \sim L \log d$) in the absence of thermalisation t_{sat} , (also known as the Thouless time [130]); ii. the timescale t_{therm} at which the system approaches thermalisation with the bath.

Note, this t_{therm} should not be confused with internal relaxation timescale, which for brevity we assume is much longer than t_{therm} . On this timescale the complexity decreases to that of the reduced density matrix on the length scale of the thermal correlation length $\xi(T)$; *i.e.* an operator entanglement $\sim \xi(T) \log d$ and operator bond dimension $d^{\xi(T)}$.

The complexity barrier between early and late times depends upon the relative size of t_{sat} and t_{therm} . The worst case is when $t_{therm} \gg t_{sat}$, this is the complexity of an arbitrary state of the system. Whereas if $t_{therm} < t_{sat}$ then the complexity barrier may be considerably less – and an efficient classical simulation possible.

In this limit, as shown by the results presented here, the ballistic early growth of entanglement may also be suppressed. Moreover, a complete understanding of the thermalisation process from this complexity point of view is also lacking. A reliable estimate of the height of the complexity barrier is therefore still unavailable.

A variational description of the state (say using MPS) is efficient before the complexity barrier and a variational description of the density matrix (for example using an MPO) is efficient at later times. Because of this, we do not expect a more efficient classical algorithm exists to describe the worst case volume-law phase. An

attractive feature of the TDVP Langevin approach to describing the dynamics of this phase is that it permits the use of the same semi-classical parametrization – the variational parameters – from early to late times and ultimately connects to the very late-time hydrodynamic limit.

It is worth comparing this discussion with recent classical time-evolution algorithms that permit an efficient description of local observables in closed thermalising systems, valid for all time [98, 131, 132]. The central idea in these works is that correlations beyond a certain lengthscale are neglected as they never affect local observables. When coupled to an external bath, the explicit restriction to local observables is not required since the bath decoheres longer-range correlations. Whether an internal or external bath, the underlying principles seem similar.

4.5 Further applications

We present applications for the TDVP-Langevin equation that take advantage of the entanglement dynamics/regimes it can probe. Both adiabatic quantum computation and many-body localisation exist in isolated quantum systems, but experimentally there is always some coupling to an environment. The TDVP-Langevin equation can be useful where we wish to study weakly open systems.

Analog error correction

The adiabatic theorem [133] allows for adiabatic quantum computing (AQC). This is useful in the scenario of satisfiability problems and other combinatorial search problems. While ground states are a fundamental notion within condensed matter physics, within computational complexity theory a close analogy can be made with constraint satisfaction problems (CSPs).

A CSP asks whether some mathematical object has a state that satisfies a number of constraints, if not, the problem is said to be unsatisfiable. The terms of some local Hamiltonian can represent constraints whose violation have an associated energy cost, thus taking the system out of equilibrium, proving unsatisfiability. By slowly changing the Hamiltonian, a consequence of the adiabatic theorem is access to quantum states we cannot prepare, i.e. the ground states of our problem Hamiltonian.

Shifting from classical to quantum, the adiabatic theorem implies that such a protocol is guaranteed to work, given we have an isolated quantum system. Realistically, there will always be sources of decoherence. Here we ask whether this present work can be applied to identify a *tolerable* amount of decoherence that can preserve what would be *enough* quantum correlations in the system to take advantage of in computation.

AQC is equivalent to gate based quantum computing, however there is no threshold theorem for adiabatic computing. The threshold theorem, or quantum fault-tolerance theorem, states that within some threshold of physical error rate, a quantum computer can suppress and bound the logical error rate [134]. No such theorem exists for AQC, however, it is interesting to speculate what it means for such a computational device to be in its Zeno phase, and if this could provide similar bounds for error-correction.

In [72] a likening is drawn with many algorithms inspired by processes occurring in the physical sciences, such as AQC, being summarized in the Langevin equation for the Brownian motion of a particle. In this work entanglement is accounted for in the Langevin equation. Then, the existence of a connected adiabatic computational path in the projected dynamics on the manifold of MPS of some bond-dimension determines the limits of AQC.

Following this line of determining entanglement resources that remain in the presence of an environment, it is shown that the dissipative failure of adiabatic quantum transport can be understood as a dynamical phase transition [135]. For the simple model of two spin-1/2s, when there is no entanglement, there is no adiabatic theorem, and so no dynamics. This provides a degree of control in suppressing entanglement and the way this inhibits adiabatic computation.

The present work on the TDVP-Langevin equation extends these analyses of two-spin Langevin evolution to many spins. Modelling the environment as local harmonic baths and thus assuming the number of dissipation channels is proportional to the number of spins translates to physical AQC devices. It is then possible to investigate how environmental depletion of entanglement can cause failure of the computation.

Many body localisation in open systems

The many-body localised (MBL) phase is an insulating phase attained in the presence of quenched disorder, where a many-body quantum system can fail to act as its own heat bath. As a result the MBL phase fails to reach thermal equilibrium, retaining memory of its initial conditions. It is characterised by this quantum ergodicity breaking and area law entanglement scaling – quantum correlations persist locally for arbitrarily long times.

The paradigmatic MBL system is the disordered XXZ spin chain,

$$H = \sum_{i=1}^{L-1} [\sigma_i^x \sigma_{i+1}^x + \sigma_i^y \sigma_{i+1}^y + \Delta \sigma_i^z \sigma_{i+1}^z] + \sum_{i=1}^L h_i \sigma_i^z \quad (4.25)$$

where h_i is random and $h_i \in [-2h, 2h]$. The transition from ergodic to MBL occurs when $h = h_c \approx 3.7$ [136]. Evidence for an MBL phase has been found experimentally [137], motivating an understanding of MBL in the presence of decoherence since achieving physical isolated quantum systems is impossible – there will always be some coupling to an environment by virtue of measurement devices.

This motivates research effort into looking at the MBL phase in open systems. In the presence of an environment, the MBL phase necessarily delocalises. The focus here is when there is weak coupling to a bath – whether the MBL phase persists in the presence of weak dephasing or if there are novel dynamic regimes here. The stability of MBL has been studied in the presence of local dissipation using the Lindblad formalism [138–144], where results are generally indicative of MBL.

An issue that faces numerical studies of MBL are finite-size constraints [145, 146]. Exact diagonalisation techniques are limited to small system sizes, so many of the approaches listed above use MPS and time evolve using TEBD [105]. Using MPS is justified deep in the MBL phase, where analytical and numerical studies find a slow, logarithmic growth of entanglement [147].

In looking at applicability of using MPS in the regime close to criticality, [148] take an approach using TDVP. They find agreement in the critical point for system sizes accessible by exact diagonalisation, and find that this drifts for larger systems. However they find evidence that the critical disorder strength saturates and they match predictions of unbounded growth of this for quasi-2D and 2D systems.

This analysis using TDVP could be extended to the TDVP-Langevin equation in order to investigate questions about weak coupling to an environment and provide a complementary view. Furthermore, non-Markovian baths can be treated in this setting, which is used to understand dephasing in the ergodic phase and study the ergodic to MBL transition [149].

4.6 Discussion

This work introduces a new method to investigate the dynamics of open many-body quantum systems, the TDVP-Langevin equation. We derive this by considering an appropriate limit of the Keldysh path integral constructed over a variational manifold. We carry this out explicitly for the MPS manifold. Our investigations reveal a phase transition in the applicability of this approach as a function of coupling to the environment – when the bath temperature and induced friction are sufficiently high, entanglement growth in individual trajectories is suppressed, and a low bond order description works for all time. This is a transition in the classical simulability of the open quantum system.

We believe that this transition is related to several other transitions in quantum dynamics that have been observed as a function of coupling to the environment or measurement, including the restriction of entanglement growth in random circuits with projective measurement, the quantum Zeno effect (and perhaps the KT transition in the spin-boson model [135, 150, 151]).

The implications of this result may be far-reaching. In the context of using the TDVP-Langevin equation to simulate open quantum systems, an efficient description for long times is possible for systems in the many-body quantum Zeno phase. Indeed, when a target system is in such a phase, there is no (asymptotic) advantage in using a quantum computer to simulate it. Since many chemical reactions of potential interest for quantum computation occur embedded in a dissipative aqueous environment, this is a point worthy of consideration.

Moreover, viewed from the perspective of a description of a quantum computational device or simulator, the transition into the many-body Zeno phase indicates transitions in the ability to solve quantum problems. While thresholds of noise

for quantum error correction have been identified in the case of gate-based quantum computation, no such thresholds currently exist for adiabatic computation. It is intriguing to speculate that determining whether a putative adiabatic computational device is in its Zeno phase or not might provide similar bounds on performance [72, 135].

We envisage a number of ways in which this work might be developed. Extending the approach to local observables in closed quantum systems presents some exciting possibilities. In this case the bath would refer to other elements of the system itself and its properties self-consistently determined through the evolution [99, 152]. Such a description has the promise of connecting early-time semi-classical descriptions to late-time hydrodynamics and thermalisation. Exploring the Fokker-Planck formulation of the TDVP-Langevin equation would bring a complementary perspective to our analysis [153–155].

The accurate description of a quantum system from early to late times is generally not possible because of growing entanglement. However, coupling to the environment can limit this growth and render this achievable. This work has coordinated physical insights from several different perspectives to develop such a numerical scheme. We hope that the algorithm itself will prove useful and that it will inspire further insights.

Chapter 5

MPS algorithms for quantum computers

In the present era of *noisy intermediate-scale quantum* (NISQ) computers, a pertinent challenge remains in how we utilise these devices. The NISQ quantum computer is limited by low numbers of qubits, limited fidelities, and incapacity for error correction. Algorithms using matrix product states (MPS) can maximise limited resources, while allowing the exploration of interesting quantum problems. The key here is that n qubits with connectivity between them can represent an MPS of bond-dimension 2^n . In this work we ultimately look to implement quantum time-evolution on ion-trap based quantum architectures. For this we present and develop the required prerequisites.

This work was performed in collaboration with Lesley Gover, Vinul Wimalaweera, James Dborin, and Andrew G. Green. This work is ongoing. I was involved with this project during the early stages of developing the algorithm.

5.1 Introduction

The term *Noisy intermediate-scale quantum* (NISQ) was coined by John Preskill [156], referring to the current state of quantum computing. Present day quantum computers are not yet advanced enough for fault-tolerant error correction, nor large enough to immediately demonstrate quantum advantage. Available NISQ devices are also limited by gate fidelities, leading to the resultant restriction on the available entanglement resources.

Matrix product state and tensor network based approaches to simulating quantum systems efficiently classically do so by restricting entanglement [23]. For NISQ devices, MPS based approaches can be useful for this reason too since the resource of quantum entanglement is limited. Furthermore, this is often not a restrictive approximation. The classical complexity of simulating the wavefunction of a system of size N is set by the Hilbert space dimension, which scales exponentially. However, as a recurring theme of this thesis, the Hilbert space actually explored by the quantum system can be structured, forming *the physically relevant corner*.

By using MPS and parametrising systems by entanglement, the size of the quantum device can be much smaller than the system being simulated. In this work we look to develop quantum algorithms using MPS for use on near-term ion-trap based quantum devices. In the remainder of the introductory section we discuss ion-trap quantum computing and how MPS can be represented here. We then move on to the results of this work, presenting our schemes for calculating state overlaps, and using this, for quantum time-evolution.

5.1.1 Ion-trap quantum computing

As contenders for future scalable quantum computers go, ion-trap based architectures show a lot of promise. Researchers have demonstrated up-to 10 minute coherence times [157], and have shown that the hardware allows gate, state-preparation, and measurement fidelities in the region of 10^{-4} to 10^{-5} [158]. This follows from the very low cross-talk from measurement.

However, for ion-traps repetition rates are not as good as for other implementations, making the sampling error high. Ion trap quantum computers work by physically *shuttling* the ions around into the active region of the trap in order to

perform gate operations, which are slow processes. Nonetheless, this results in the high gate fidelities and low cross-talk that are several orders of magnitudes higher than say for superconducting quantum computers.

Some ion-trap architectures allow for mid-circuit measurements, which in turn opens up the possibility of performing tensor network calculations [42–44] laid out in *time* rather than space. One such device is Quantinuum’s trapped-ion quantum charge-coupled device (QCCD) proposal [159]. The applicability of our algorithms is generally ambiguous of the ion-trap architecture. The results we present here are for the trapped-ion QCCD with a vision to implement these algorithms on other existing trapped-ion quantum computers to compare and benchmark.

Quantum tensor networks have been implemented on a trapped-ion QCCD, one example is an algorithm for simulating quantum quenches [160]. The general idea is the physical qubits are sequentially generated from left to right, i.e. making use of qubit reuse. The quantum coherence is stored in the bond qubits, thus all available qubits are used for the classically hard part of the simulation; capturing the entanglement. This algorithm has been used to simulate the chaotic dynamics of the self-dual kicked Ising model [161]. Mid-circuit measurement and qubit reuse meant that using at most 9 trapped ion qubits, this simulation could start from an entangled state of 32 spins.

In the remainder of the introduction we show how we map matrix product states (MPS) to *time-like* quantum circuits, using the equivalence to quantum channels that was introduced in Section 2.3. We make use of mid-circuit measurements and qubit re-use, so that the bond-dimension/entanglement information can be maximised across the presently available qubits. We also show how to represent infinite translationally invariant states using a finite state, as seen in Section 1.2, by mapping the environment degrees of freedom to a quantum circuit.

The results of this chapter are shown for the Quantinuum trapped-ion QCCD. As this work is ongoing, the results section is incomplete. Here we come across one of the major issues of using NISQ-era devices, in particular ion-traps, being sampling errors. We show how these problems are overcome by restricting the state space that we optimise over. Further, discussions are in place for running this algorithm on other ion-trap devices, which we hope will form future work.

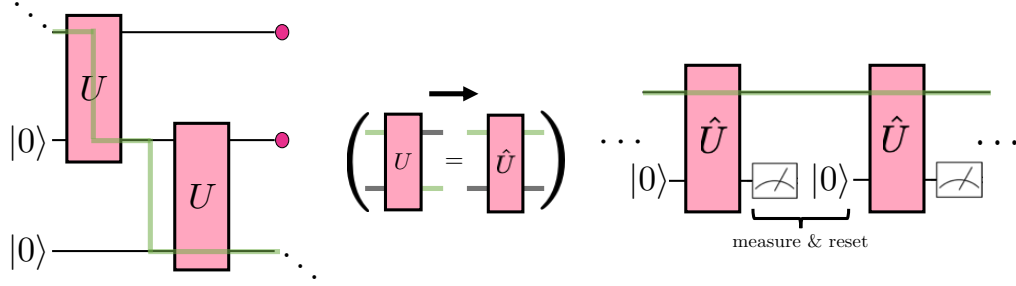


Figure 5.1: Mapping quantum circuits of matrix product states from a space-like representation to time-like. The auxiliary bond dimension leg of the circuit is identified and must be rearranged in the time-like circuit so that it acts on the first $n - 1$ qubits. This swapping of legs is shown under the arrow indicating the transformation from U to \hat{U} , with hat labelling this transformed form. In the time-like representation the final qubit in the register is measured and reset upon each application of the MPS as a unitary matrix. The entanglement information propagates through the auxiliary legs, while qubit reset at each time step means that the next site of the spin chain can be incorporated.

5.1.2 Time-like quantum circuits

In the technical introduction, Section 2.3, we have presented the mapping between matrix product states and quantum channels. Combining this with the feature of qubit reset and reuse that is available to ion-trap based quantum hardware, it is possible to simulate a D -dimensional spin system using a $(D - 1)$ -dimensional subset of qubits alongside an ancillary qubit register whose size scales logarithmically with the amount of entanglement present in the system (i.e. the scaling of bond dimension when we encode MPS in quantum circuits) [160].

This is shown for an indefinitely long spin-1/2 chain in Figure 5.1. On the left of this figure we show a spin-1/2 chain of MPS with bond-dimension $D = 2$. Each unitary U is a site on this spin chain. The green thread linking these unitaries shows how the auxiliary, bond dimension ‘leg’ travels through the circuit (see Figure 2.2 to see how these legs are reshaped). On the right of this figure we show how to map such an MPS laid out in space onto a ‘time-like’ representation.

Here the top-most qubits carry the auxiliary bond-dimension information. For the case of $D = 2$ this is one qubit, otherwise bond dimensions $D = 4, 8, 16, \dots$ would be captured by $2, 3, 4, \dots$ ancillary qubits. After the application of each unitary representing the MPS, the final qubit is measured and reset. This means that this qubit can be shuttled and reused to apply the next unitary along the spin-chain. In this way we have a time-like representation as the next unitary is available and can be applied at the following timestep.

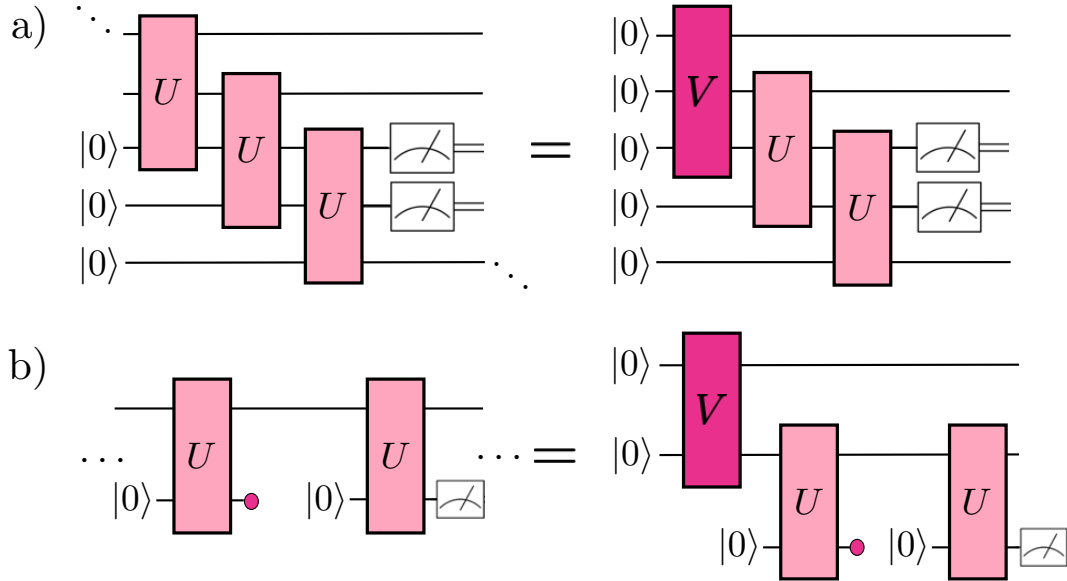


Figure 5.2: Representing infinite translationally invariant states using the power method. Rather than solving the necessary fixed point equations, repeated application of the MPS unitary should converge exponentially to the correct environment tensor. This convergence to V is shown here. a) In the space-like representation, right environment, V , i.e. the infinite state on the right of some point of interest can be summarised by a finite state, the left environment is $L = \mathbb{1}$. b) In the time-like representation, left environment, V , can be summarised by a finite state, the right environment is $R = \mathbb{1}$.

Now we can consider how to represent infinite states. Figure 5.2 shows how we do this for space-like and time-like representations. When calculating some observables at a certain site, the environment tensor V represents the effect of the remainder of the system. This can be solved for via the fixed point equations shown in the technical introduction, Sec 2.3, in Fig. 2.4. The construction of the environment is dependent on the transfer matrix (used to calculate the overlap density classically).

The environment can be approximated using *the power method*, which approximates the infinite state with a finite state. Long chains of the transfer matrix should converge exponentially to the environment tensor. When we introduce our algorithm in the following section, we also show how the transfer matrix is represented in the ‘time-like’ circuits. For transfer matrix C , the power method is the statement that $\lim_{n \rightarrow \infty} C^n V \propto V_0$, where V is some vector and V_0 is the highest eigenvalue. In the following section we calculate these quantities in the time-like representation, beginning with state overlaps and expectation values.

5.2 The algorithm

Here we present the methods used to calculate state overlaps and perform time evolution using time-dependent variational principle. Before considering quantum dynamics, we must be able to compute the overlap effectively as this is a common step in variational protocols. As a starting step we use a simple approximation to the environment using the fact that the time evolution is over a small time interval δt . We then compute the overlap density using the power method.

5.2.1 Calculating state overlaps

For two MPS encoded as unitaries, U_A and U_B , their overlap is computed by considering circuits of the form depicted in Figure 5.3. These circuits consist of n repeating blocks of the transfer matrix C_n . In the case of Figure 5.3, $n = 3$ are visible. For general $U_A \neq U_B$, as $n \rightarrow \infty$, this gives an overlap of 0. The distance between states is encoded in the rate at which the outcome of this circuit tends to 0. This occurs as λ^n , where λ is the principle eigenvalue of the transfer matrix E_{U_A, U_B} .

There are many ways to compute E_{U_A, U_B} [41] uses a variational representation of the either side eigenvectors of the transfer matrix (here these are dubbed top \vec{T} and bottom \vec{B} due to the way this circuit is laid out in space and are analogous to \vec{L} and \vec{R}). To do this involves solving fixed-point equations for \vec{L} and \vec{R} . While in [162] this is expanded on by using the power method instead. The principle eigenvalue is given by,

$$\lambda = \lim_{n \rightarrow \infty} \frac{\vec{L} \cdot E_{U_A, U_B}^n \cdot \vec{R}}{\vec{L} \cdot E_{U_A, U_B}^{n-1} \cdot \vec{R}} = \lim_{n \rightarrow \infty} \frac{C_n(U_A, U_B)}{C_{n-1}(U_A, U_B)} \quad (5.1)$$

Where \vec{L} and \vec{R} are approximations to the eigenvectors of either transfer matrix. This is equivalent to considering ‘long’ blocks of the quantum circuit C_n , i.e. using the power method, and in the limit $n \rightarrow \infty$ this should converge to $\lambda^n / \lambda^{n-1}$. This converges exponentially quickly, and can be sped up for good choices of \vec{L} and \vec{R} . When either approximation is exact, this converges for $n = 1$. For these simulations, $L = |0\rangle\langle 0| + \mathcal{O}(dt^2)$ and $R = \mathbb{1} + \mathcal{O}(dt^2)$.

The symbol representing the destructive SWAP test is a new element appearing in this circuit. The symbol summarises a block containing a Hadamard gate, followed by a CNOT gate and then measurement of both qubits. This is a time-like

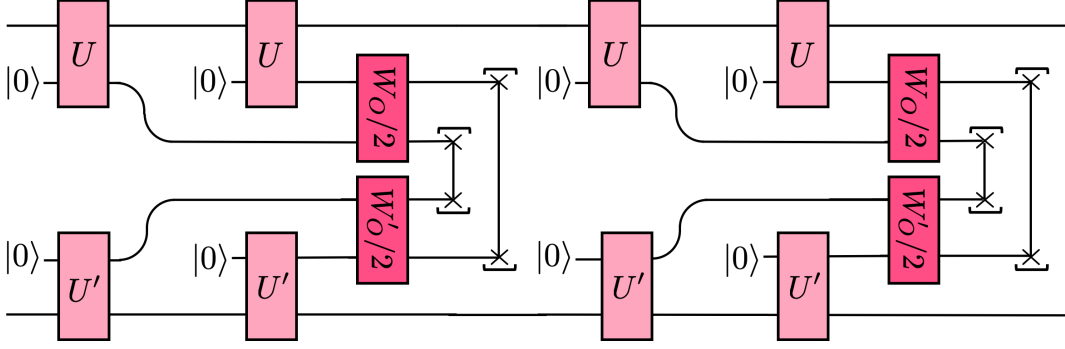


Figure 5.4: First order trotterisation scheme implementing *quantum* time-dependent variational principle. This circuit provides a cost function where the optimisation over U' gives the state parametrised by U at the next time step. Here two powers of the power method are shown. The cost function is $L = |0\rangle\langle 0|$ and due to the first-order Trotterisation errors are such that $R = \mathbb{1} + \mathcal{O}(dt^2)$. Here U is evolved forward by half a time step and the U' is evolved backwards by half a time step for symmetry.

5.2.2 Quantum time-dependent variational principle

In designing algorithms for NISQ devices, the number of qubits the algorithm uses must be minimised. Further the qubits themselves and their landscape will incur sources of errors specific to the device. The key to implementing algorithms is in the management and mitigation of errors, and of course this can be achieved by limiting the resources the algorithm requires. Thus, our implementation of the time-dependent variational principle (TDVP) must be simple.

This implementation of time evolution follows from the method for computing state overlaps [162, 164–166]. Some MPS $|\psi(U(t))\rangle$ parametrised by the unitary $U(t)$ can be time-evolved to a time $t + dt$ under some Hamiltonian H as follows,

$$U(t + dt) = \underset{W}{\operatorname{argmax}} |\langle \psi(W) | e^{iHdt} | \psi(U(t)) \rangle| \quad (5.2)$$

If using the power method to compute this overlap, the probability λ that the swap test measures $0^{\otimes N}$ is the principle eigenvalue of the transfer matrix. For a state parametrised by U at time t , the time evolution circuit provides a cost function whose optimisation over U' returns the state at time $t + dt$. We use the time evolution cost function circuit of Figure 5.4 and repeating blocks of this (the power method) to approximate the principle eigenvalue.

The time evolution operator is expanded using a Trotterisation scheme. While higher order Trotterisation schemes improve the scaling of errors with the time step

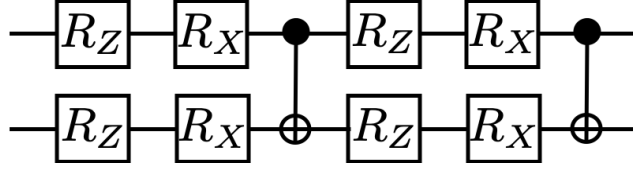


Figure 5.5: Parameterisation of the unitaries so as to restrict the state space optimised over. Due to high sampling errors, we assume that we know two previous steps of the time evolution, so the third step is more simply interpolated. In the simulations, this consists of specifying the Z and X rotations that generate the previous steps.

dt , for circuits laid out in time, their implementation require more qubits. To keep the number of qubits minimal, a feature of translationally invariant states evolving with nearest-neighbour, translationally-invariant Hamiltonians is employed. In this case the TDVP equations with either only the even or odd parts of the Hamiltonian is the same as evolving using the full Hamiltonian then dividing by two [25].

In Figure 5.4, this circuit implements a first order Trotterisation scheme that uses only the odd-bonds of the Hamiltonian. For this scheme the cost function is $L = |0\rangle\langle 0| + \mathcal{O}(dt^2)$ and $R = \mathbb{1} + \mathcal{O}(dt^2)$. Due to this projecting back onto translationally invariant states, errors are incurred at a higher order in dt than is expected by simply accounting for Trotter errors [162]. The repeating block of this circuit is the transfer matrix, so that in Figure 5.4, two powers of the transfer matrix are shown.

5.3 Results

Since this project is in progress, we present the results as they stand so far. We study the dynamical quantum phase transition of the one-dimensional transverse field Ising model [162]. For N sites, the Hamiltonian is given by,

$$H = -J \sum_i^{N-1} \hat{Z}_i \hat{Z}_{i+1} + g \sum_i^N X_i, \quad (5.3)$$

where \hat{Z} and \hat{X} are Pauli matrices acting on site i , J the exchange coupling and g the transverse field. This model harbours a phase transition in the ground state when $g/J = 1$. It has a further *dynamical* quantum phase transition, a phase transition driven by advancing time as opposed to being driven by control parameters such as temperature or pressure. This is when a ground state on one side of this transition (say $g/J < 1$) is evolved with a Hamiltonian opposite (in this case $g/J > 1$).

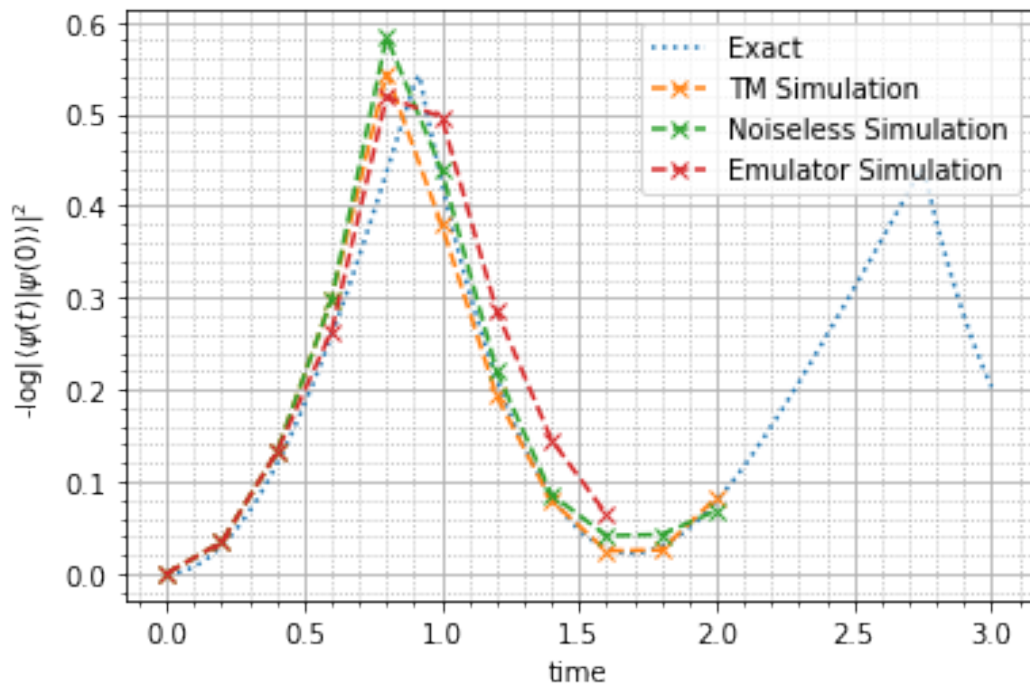


Figure 5.6: Exact and simulated results of the dynamical quantum phase transition. The exact result is useful for comparison with the quantum algorithm. The ‘TM simulation’ refers to dynamics obtained from numerical optimisation of the principle eigenvalue of the ansatz transfer matrix. This is useful for comparison with the simulations as it uses the reduced parameterisation of the 2-qubit unitaries. Further, this is why this calculation does not exactly align with the exact result. Two results are shown for the simulation using the time-evolution algorithm presented here. The noiseless simulation is the numerical optimisation of the circuits Fig. 5.4 in the absence of noise. The emulator simulation is the implementation of this algorithm on the Honeywell ion-trap device emulator. The quantum algorithm is faithful in reproducing the dynamics.

We present results showing that the groundstate and dynamical properties of this model can be seen, thus investigated, on the Quantinuum machine. This algorithm is implemented using the Quantinuum emulator, and plots for the cost function obtained reflects the dynamics we expect.

5.3.1 Mitigating sampling costs

Ion traps have very high gate and measurement fidelities. Their performance is primarily inhibited by long repetition times, which limits the number of samples that can be taken. Without careful consideration, the number of samples required to optimise the U' that parametrises the next time step is prohibitive. This problem is overcome by making a good initial guess.

We assume knowledge of the previous two steps of the time evolution so that the state space optimised over is restricted, we linearly extrapolate to the next time step as an initial guess. This is corrected using SPSA (simultaneous perturbation stochastic approximation) [167] with a narrowly defined sampling region to improve this guess. Furthermore, the unitaries U' are parametrised as shown in Figure 5.5 to enable shallower circuits [162].

5.3.2 Results so far

These results are presented in Fig. 5.6, where $J = 1$, and we begin with a groundstate with $g = 1.5$ and evolve under $g = 0.2$. In Fig 5.6, the results of four calculations are shown. The exact calculation is performed using a Jordan-Wigner transformation and is a useful basis for comparison. The ‘TM simulation’ refers to simulating using transfer matrix methods. Here the parameters of the unitaries are optimised by first converting to the tensor representation and then computing the largest eigenvalue of the transfer matrix. This is useful for comparison with as the peak is shifted slightly left due to also using the reduced parameterisation (Fig 5.5).

We show two simulations using the first order time evolution algorithm we have presented, Fig. 5.4. The noiseless simulation refers to its implementation and numerical optimisation using Cirq, and the emulator simulation is using the Honeywell device emulator. These results show that the time evolution algorithm can reproduce these dynamics. The good results from the Honeywell emulator are promising of the utility of this algorithm for Quantinuum’s device and potentially other ion-trap devices.

5.4 Discussion

So far, this work has demonstrated and implemented an algorithm for performing quantum time evolution on emulators for ion-trap NISQ devices. The emulator results are promising, meaning that we can hope to run this on actual quantum hardware. In future work we would like to be able to implement this algorithm on other ion-trap quantum devices and look at extending to higher bond-dimensions.

Chapter 6

Discussion

This thesis is formed of three main research projects that make use of tensor network, and more specifically, matrix product state (MPS) representations of quantum states. Tensor network representations parameterise the quantum state according to the amount of entanglement. The individual tensors capture some degree of entanglement, or some other key property of the overall wavefunction. Connecting these regions creates a network that builds the complex quantum state. Each research project of this thesis differs in the nature of research and none directly follow from the other, but they all take advantage of the attractive properties of tensor network states, and within these MPS.

The main technique used in this thesis are MPS parameterisations of the many-body Hilbert space. Calculations involving the many-body Hilbert space are often limited by exponential scaling as more bodies are added. For one-dimensional quantum systems, every state can be written in the MPS decomposition, and this representation is useful when bond-dimension D is small. Physically relevant states tend to embody less entanglement than random states in Hilbert space, making the reduction to MPS efficient and useful. In this work, MPS techniques have been extended to tools for the study of field theories of condensed matter, open quantum systems, and quantum simulation, with their advantages built in.

In the first project chapter titled 'A generalised Haldane map for the J_1 - J_2 model', presents an application for field theories over MPS, where entanglement can be captured at the saddle point. In the following chapter, which is a more numerical simulation project, 'phase transitions in the classical simulability of open quantum systems', MPS are the semi-classical states for which we can write

a Langevin equation. Finally, with ‘MPS algorithms for quantum computers’, MPS are utilised in order to maximise the limited entanglement resources of current NISQ-era quantum computers.

The main achievements of this work for each project are: i. Showing the utility of path integrals over MPS, re-deriving the critical point of the J_1 - J_2 model in a simpler way, and as such elucidating the link between the topological terms that enter into field theories and the MPS formulation. ii. Presenting a new way to simulate open quantum systems, using the TDVP-Langevin equation over tensor network states, and providing the Hamiltonian analogue of measurement-induced phase transitions, and demonstrating such entanglement transitions in the finite temperature case. iii. Demonstrating a new algorithm for use on NISQ-era ion trap quantum computers that capitalises on the features of these devices.

There are various future avenues for each project. A goal of the MPS description of the deconfined quantum criticality in the J_1 - J_2 model is to be able to extend to higher dimensional J - Q models, where the analysis is much more complicated. For the TDVP-Langevin equation, it would be interesting to see whether this approach lends to an equivalent threshold theorem for adiabatic quantum computing. This technique can be applied to various scenarios involving open quantum systems, and could be extended to the study of local observables in closed systems. In the limit of a linearised TDVP-Langevin equation, one may seek exact analytic solutions. For quantum time evolution on ion-trap quantum computers, we hope we can use this algorithm on different existing devices and be able to time-evolve larger systems and to higher bond-dimensions.

Progress in theoretical physics is often times importing insights and the joining of ideas of its various sub-disciplines. For tensor network techniques, the focus on entanglement is importing insights from quantum information theory to some problems more in the domain of condensed matter physics. Matrix product states began by providing insights to understanding the spin-1 quantum Heisenberg chain, and now they are ubiquitous. This thesis has made use of many tensor network and matrix product state based tools, and it will be interesting to see in what new arenas these tools may find use.

Bibliography

- [1] Richard P. Feynman. Simulating physics with computers. *International Journal of Theoretical Physics*, 21(6):467–488, 1982.
- [2] Louis De Broglie. Waves and quanta. *Nature*, 112(2815):540–540, 1923.
- [3] George P Thomson and Alexander Reid. Diffraction of cathode rays by a thin film. *Nature*, 119(3007):890–890, 1927.
- [4] Clinton Davisson and Lester H Germer. The scattering of electrons by a single crystal of nickel. *Nature*, 119(2998):558–560, 1927.
- [5] Earl J. Kirkland. Advanced computing in electron microscopy. In *Advanced Computing in Electron Microscopy*, 1998.
- [6] A. Einstein, B. Podolsky, and N. Rosen. Can quantum-mechanical description of physical reality be considered complete? *Phys. Rev.*, 47:777–780, May 1935.
- [7] J. S. Bell. On the einstein podolsky rosen paradox. *Physics Physique Fizika*, 1:195–200, Nov 1964.
- [8] W. Pauli. Über den zusammenhang des abschlusses der elektronengruppen im atom mit der komplexstruktur der spektren. *Zeitschrift für Physik*, 31(1):765–783, 1925.
- [9] J Frenkel. *Wave mechanics, advanced general theory*, volume 1. Oxford, 1934.
- [10] Román Orús. Tensor networks for complex quantum systems. *Nature Reviews Physics*, 1(9):538–550, 2019.
- [11] F. Verstraete, M. M. Wolf, D. Perez-Garcia, and J. I. Cirac. Criticality, the area law, and the computational power of projected entangled pair states. *Phys. Rev. Lett.*, 96:220601, Jun 2006.
- [12] Matthew B Hastings. An area law for one-dimensional quantum systems. *Journal of Statistical Mechanics: Theory and Experiment*, 2007(08):P08024, 2007.
- [13] Jacob D. Bekenstein. Black holes and entropy. *Phys. Rev. D*, 7:2333–2346, Apr 1973.
- [14] FDM Haldane. O (3) nonlinear σ model and the topological distinction between integer-and half-integer-spin antiferromagnets in two dimensions. *Physical Review Letters*, 61(8):1029, 1988.
- [15] J. J. Sakurai and Jim Napolitano. *Modern Quantum Mechanics*. Cambridge University Press, 2 edition, 2017.
- [16] J. R. Klauder. Coherent state (Quantum mechanics). *Scholarpedia*, 4(9):8686, 2009. revision #121886.

- [17] R. P. Feynman. Space-time approach to non-relativistic quantum mechanics. *Reviews of Modern Physics*, 20(2):367–387, 1948.
- [18] J M Radcliffe. Some properties of coherent spin states. *Journal of Physics A: General Physics*, 4(3):313, 1971.
- [19] Eduardo Fradkin. *Field theories of condensed matter physics*. Cambridge University Press, 2013.
- [20] U. Schollwöck. The density-matrix renormalization group. *Rev. Mod. Phys.*, 77:259–315, Apr 2005.
- [21] David Perez-Garcia, Frank Verstraete, Michael M Wolf, and J Ignacio Cirac. Matrix product state representations. *arXiv preprint quant-ph/0608197*, 2006.
- [22] Ian Affleck, Tom Kennedy, Elliott H. Lieb, and Hal Tasaki. Rigorous results on valence-bond ground states in antiferromagnets. *Phys. Rev. Lett.*, 59:799–802, Aug 1987.
- [23] Guifré Vidal. Efficient classical simulation of slightly entangled quantum computations. *Physical Review Letters*, 91(14), 2003.
- [24] Steven R. White. Density matrix formulation for quantum renormalization groups. *Physical Review Letters*, 69(19):2863–2866, 1992.
- [25] J. Haegeman, J.I. Cirac, T.J. Osborne, I. Pižorn, H. Verschelde, and F. Verstraete. Time-dependent variational principle for quantum lattices. *Physical Review Letters*, 107:070601, 2011.
- [26] Eyal Leviatan, Frank Pollmann, Jens H Bardarson, David A Huse, and Ehud Altman. Quantum thermalization dynamics with matrix-product states. *arXiv preprint arXiv:1702.08894*, 2017.
- [27] Jutho Haegeman, Christian Lubich, Ivan Oseledets, Bart Vandereycken, and Frank Verstraete. Unifying time evolution and optimization with matrix product states. *Physical Review B*, 94(16):165116, 2016.
- [28] AG Green, CA Hooley, J Keeling, and SH Simon. Feynman path integrals over entangled states. *arXiv preprint arXiv:1607.01778*, 2016.
- [29] Andrew Hallam. *Tensor network descriptions of quantum entanglement in path integrals, thermalisation and machine learning*. PhD thesis, University College London, UCL, London, 2019.
- [30] H.P. Breuer and F. Petruccione. *The Theory of Open Quantum Systems*. Oxford University Press, 2007.
- [31] Herbert Spohn and Joel L. Lebowitz. *Irreversible Thermodynamics for Quantum Systems Weakly Coupled to Thermal Reservoirs*, pages 109–142. John Wiley I& Sons, Ltd, 1978.
- [32] A. O. Caldeira and A. J. Leggett. Quantum tunnelling in a dissipative system. *Annals of Physics*, 149(2):374–456, September 1983.
- [33] Alex Kamenev. Keldysh and doi-peliti techniques for out-of-equilibrium systems. In *Strongly Correlated Fermions and Bosons in Low-Dimensional Disordered Systems*, pages 313–340. Springer, 2002.
- [34] James Gordon Morley–Wilkinson. *Evolution of entanglement structure in open quantum systems*. PhD thesis, University College London, UCL, London, 2019.

- [35] Adam Nahum, Jonathan Ruhman, Sagar Vijay, and Jeongwan Haah. Quantum entanglement growth under random unitary dynamics. *Physical Review X*, 7(3):031016, 2017.
- [36] Chao-Ming Jian, Yi-Zhuang You, Romain Vasseur, and Andreas W. W. Ludwig. Measurement-induced criticality in random quantum circuits. *Phys. Rev. B*, 101:104302, Mar 2020.
- [37] Michael J. Gullans and David A. Huse. Dynamical purification phase transition induced by quantum measurements. *Phys. Rev. X*, 10:041020, Oct 2020.
- [38] I. Manin and Freeman J. Dyson. Mathematics as metaphor: selected essays of yuri i. manin. In *Mathematics as metaphor: selected essays of Yuri I. Manin*, 2007.
- [39] Kishor Bharti, Alba Cervera-Lierta, Thi Ha Kyaw, Tobias Haug, Sumner Alperin-Lea, Abhinav Anand, Matthias Degroote, Hermann Heimonen, Jakob S. Kottmann, Tim Menke, Wai-Keong Mok, Sukin Sim, Leong-Chuan Kwek, and Alán Aspuru-Guzik. Noisy intermediate-scale quantum algorithms. *Rev. Mod. Phys.*, 94:015004, Feb 2022.
- [40] Michael A. Nielsen and Isaac L. Chuang. *Quantum Computation and Quantum Information: 10th Anniversary Edition*. Cambridge University Press, 2010.
- [41] F. Barratt, James Dborin, Matthias Bal, Vid Stojevic, Frank Pollmann, and A. G. Green. Parallel quantum simulation of large systems on small nisy computers. *npj Quantum Information*, 7(1):79, 2021.
- [42] C. Schön, E. Solano, F. Verstraete, J. I. Cirac, and M. M. Wolf. Sequential generation of entangled multiqubit states. *Phys. Rev. Lett.*, 95:110503, Sep 2005.
- [43] Sarang Gopalakrishnan and Austen Lamacraft. Unitary circuits of finite depth and infinite width from quantum channels. *Phys. Rev. B*, 100:064309, Aug 2019.
- [44] Shi-Ju Ran. Encoding of matrix product states into quantum circuits of one- and two-qubit gates. *Phys. Rev. A*, 101:032310, Mar 2020.
- [45] F. Azad, A. J. McRoberts, C. Hooley, and A. G. Green. A generalised haldane map for the one-dimensional j1-j2 model. In Preparation.
- [46] Todadri Senthil, Ashvin Vishwanath, Leon Balents, Subir Sachdev, and Matthew PA Fisher. Deconfined quantum critical points. *Science*, 303(5663):1490–1494, 2004.
- [47] +T. Senthil, +Leon Balents, +Subir Sachdev, +Ashvin Vishwanath, and +Matthew +P. +A. Fisher. Quantum criticality beyond the landau-ginzburg-wilson paradigm. *Physical Review B*, 70(14), 2004.
- [48] +T. Senthil, +Ashvin Vishwanath, +Leon Balents, +Subir Sachdev, and +Matthew+P.+A." Fisher. Deconfined quantum critical points. *Science*, 303(5663):1490–1494, 2004.
- [49] T Senthil and Matthew PA Fisher. Competing orders, nonlinear sigma models, and topological terms in quantum magnets. *Physical Review B*, 74(6):064405, 2006.
- [50] Ian Affleck and FDM Haldane. Critical theory of quantum spin chains. *Physical Review B*, 36(10):5291, 1987.

- [51] LD Landau, EM Lifshitz, and LP Pitaevskii. Statistical physics, part 2. *Course of theoretical physics*, 9:67, 1981.
- [52] Kenneth G Wilson. The renormalization group and critical phenomena. *Reviews of Modern Physics*, 55(3):583, 1983.
- [53] Subir Sachdev. Quantum phase transitions. *Handbook of Magnetism and Advanced Magnetic Materials*, 2007.
- [54] Subir Sachdev. The quantum phases of matter. *arXiv preprint arXiv:1203.4565*, 2012.
- [55] Tom Kennedy and Hal Tasaki. Hidden $z \times z$ symmetry breaking in haldane-gap antiferromagnets. *Physical review b*, 45(1):304, 1992.
- [56] Michael Aizenman and Bruno Nachtergaele. Geometric aspects of quantum spin states. *Communications in Mathematical Physics*, 164(1):17–63, 1994.
- [57] Marcel den Nijs and Koos Rommelse. Preroughening transitions in crystal surfaces and valence-bond phases in quantum spin chains. *Physical Review B*, 40(7):4709, 1989.
- [58] Assa Auerbach. *Interacting electrons and quantum magnetism*. Springer Science & Business Media, 2012.
- [59] Timothy Ziman and HJ Schulz. Are antiferromagnetic spin chains representations of the higher wess-zumino-witten models? *Physical review letters*, 59(1):140, 1987.
- [60] Shoudan Liang. Monte carlo calculations of the correlation functions for heisenberg spin chains at $t=0$. *Physical review letters*, 64(13):1597, 1990.
- [61] Edward Witten. Non-abelian bosonization in two dimensions. In *Bosonization*, pages 201–218. World Scientific, 1994.
- [62] W. J. L Buyers, R. M. Morra, R. L. Armstrong, M. J. Hogan, P. Gerlach, and Hirakawa K. Experimental evidence for the haldane gap in a spin-1 nearly isotropic, antiferromagnetic chain. *Phys. Rev. Lett.*, 56:371–374, Jan 1986.
- [63] FDM Haldane. Spontaneous dimerization in the $s=1$ heisenberg antiferromagnetic chain with competing interactions. *Physical Review B*, 25(7):4925, 1982.
- [64] Shunsuke Furukawa, Masahiro Sato, Shigeki Onoda, and Akira Furusaki. Ground-state phase diagram of a spin-1 frustrated ferromagnetic xxz chain: Haldane dimer phase and gapped/gapless chiral phases. *Physical Review B*, 86(9):094417, 2012.
- [65] Chanchal K Majumdar and Dipan K Ghosh. On next-nearest-neighbor interaction in linear chain. i. *Journal of Mathematical Physics*, 10(8):1388–1398, 1969.
- [66] Chanchal K. Majumdar and Dipan K. Ghosh. On next-nearest-neighbor interaction in linear chain. II. *Journal of Mathematical Physics*, 10(8):1399–1402, aug 1969.
- [67] Kiyomi Okamoto and Kiyohide Nomura. Fluid-dimer critical point in $s=1$ antiferromagnetic heisenberg chain with next nearest neighbor interactions. *Physics Letters A*, 169(6):433–437, 1992.

- [68] K Nomura and K Okamoto. Critical properties of $s=1/2$ antiferromagnetic XXZ chain with next-nearest-neighbour interactions. *Journal of Physics A: Mathematical and General*, 27(17):5773–5788, sep 1994.
- [69] Steven R White and Ian Affleck. Dimerization and incommensurate spiral spin correlations in the zigzag spin chain: Analogies to the kondo lattice. *Physical Review B*, 54(14):9862, 1996.
- [70] Alexander A. Nersisyan, Alexander O. Gogolin, and Fabian H. L. Eßler. Incommensurate spin correlations in spin- $1/2$ frustrated two-leg heisenberg ladders. *Phys. Rev. Lett.*, 81:910–913, Jul 1998.
- [71] F Duncan M Haldane. Continuum dynamics of the 1-d heisenberg antiferromagnet: Identification with the $o(3)$ nonlinear sigma model. *Physics Letters A*, 93(9):464–468, 1983.
- [72] PJD Crowley, T Đurić, W Vinci, PA Warburton, and AG Green. Quantum and classical dynamics in adiabatic computation. *Physical Review A*, 90(4):042317, 2014.
- [73] M. C. Bañuls, D. Pérez-García, M. M. Wolf, F. Verstraete, and J. I. Cirac. Sequentially generated states for the study of two-dimensional systems. *Phys. Rev. A*, 77:052306, May 2008.
- [74] Adam Nahum, P. Serna, J. T. Chalker, M. Ortuño, and A. M. Somoza. Emergent $so(5)$ symmetry at the néel to valence-bond-solid transition. *Phys. Rev. Lett.*, 115:267203, Dec 2015.
- [75] F. Azad, A. Hallam, J. Morley, and A. G. Green. Phase transitions in the classical simulability of open quantum systems. *Scientific Reports*, 13(1):8866, 2023.
- [76] Yaodong Li, Xiao Chen, and Matthew PA Fisher. Quantum zeno effect and the many-body entanglement transition. *Physical Review B*, 98(20):205136, 2018.
- [77] Adam Nahum, Sagar Vijay, and Jeongwan Haah. Operator spreading in random unitary circuits. *Physical Review X*, 8(2):021014, 2018.
- [78] CW von Keyserlingk, Tibor Rakovszky, Frank Pollmann, and SL Sondhi. Operator hydrodynamics, otocs, and entanglement growth in systems without conservation laws. *Physical Review X*, 8(2):021013, 2018.
- [79] Amos Chan, Rahul M Nandkishore, Michael Pretko, and Graeme Smith. Unitary-projective entanglement dynamics. *Physical Review B*, 99(22):224307, 2019.
- [80] Yaodong Li, Xiao Chen, and Matthew PA Fisher. Measurement-driven entanglement transition in hybrid quantum circuits. *Physical Review B*, 100(13):134306, 2019.
- [81] Marcin Szyniszewski, Alessandro Romito, and Henning Schomerus. Entanglement transition from variable-strength weak measurements. *Physical Review B*, 100(6):064204, 2019.
- [82] Baidyanath Misra and EC George Sudarshan. The zeno’s paradox in quantum theory. *Journal of Mathematical Physics*, 18(4):756–763, 1977.
- [83] Marcin Szyniszewski, Alessandro Romito, and Henning Schomerus. Universality of entanglement transitions from stroboscopic to continuous measurements. *Physical review letters*, 125(21):210602, 2020.

- [84] Yaodong Li, Xiao Chen, Andreas WW Ludwig, and Matthew Fisher. Conformal invariance and quantum non-locality in hybrid quantum circuits. *arXiv preprint arXiv:2003.12721*, 2020.
- [85] Xiao Chen, Yaodong Li, Matthew PA Fisher, and Andrew Lucas. Emergent conformal symmetry in nonunitary random dynamics of free fermions. *Physical Review Research*, 2(3):033017, 2020.
- [86] Qicheng Tang and W Zhu. Measurement-induced phase transition: A case study in the nonintegrable model by density-matrix renormalization group calculations. *Physical Review Research*, 2(1):013022, 2020.
- [87] Lei Zhang, Justin A Reyes, Stefanos Kourtis, Claudio Chamon, Eduardo R Mucciolo, and Andrei E Ruckenstein. Nonuniversal entanglement level statistics in projection-driven quantum circuits. *Physical Review B*, 101(23):235104, 2020.
- [88] Aidan Zabalo, Michael J Gullans, Justin H Wilson, Sarang Gopalakrishnan, David A Huse, and JH Pixley. Critical properties of the measurement-induced transition in random quantum circuits. *Physical Review B*, 101(6):060301, 2020.
- [89] Michael J Gullans and David A Huse. Scalable probes of measurement-induced criticality. *Physical review letters*, 125(7):070606, 2020.
- [90] Michael J Gullans and David A Huse. Dynamical purification phase transition induced by quantum measurements. *Physical Review X*, 10(4):041020, 2020.
- [91] Chao-Ming Jian, Yi-Zhuang You, Romain Vasseur, and Andreas WW Ludwig. Measurement-induced criticality in random quantum circuits. *Physical Review B*, 101(10):104302, 2020.
- [92] Soonwon Choi, Yimu Bao, Xiao-Liang Qi, and Ehud Altman. Quantum error correction in scrambling dynamics and measurement-induced phase transition. *Physical Review Letters*, 125(3):030505, 2020.
- [93] Yimu Bao, Soonwon Choi, and Ehud Altman. Theory of the phase transition in random unitary circuits with measurements. *Physical Review B*, 101(10):104301, 2020.
- [94] Shimpei Goto and Ippei Danshita. Measurement-induced transitions of the entanglement scaling law in ultracold gases with controllable dissipation. *Physical Review A*, 102(3):033316, 2020.
- [95] Vincenzo Alba and Federico Carollo. Spreading of correlations in markovian open quantum systems. *Physical Review B*, 103(2):L020302, 2021.
- [96] Yohei Fuji and Yuto Ashida. Measurement-induced quantum criticality under continuous monitoring. *Physical Review B*, 102(5):054302, 2020.
- [97] O. Alberton, M. Buchhold, and S. Diehl. Entanglement transition in a monitored free-fermion chain: From extended criticality to area law. *Phys. Rev. Lett.*, 126:170602, Apr 2021.
- [98] Andrew Hallam, JG Morley, and Andrew G Green. The lyapunov spectra of quantum thermalisation. *Nature communications*, 10(1):1–8, 2019.
- [99] Robert Zwanzig. Ensemble method in the theory of irreversibility. *The Journal of Chemical Physics*, 33(5):1338–1341, 1960.

- [100] B. Pirvu, V. Murg, J. I. Cirac, and F. Verstraete. Matrix product operator representations. *New Journal of Physics*, 12(2):025012, February 2010.
- [101] Michael P. Zaletel, Roger S. K. Mong, Christoph Karrasch, Joel E. Moore, and Frank Pollmann. Time-evolving a matrix product state with long-ranged interactions. *Phys. Rev. B*, 91:165112, Apr 2015.
- [102] Giuseppe Carleo and Matthias Troyer. Solving the quantum many-body problem with artificial neural networks. *Science*, 355(6325):602–606, 2017.
- [103] Michael J Hartmann and Giuseppe Carleo. Neural-network approach to dissipative quantum many-body dynamics. *Physical review letters*, 122(25):250502, 2019.
- [104] Markus Schmitt and Markus Heyl. Quantum many-body dynamics in two dimensions with artificial neural networks. *Physical Review Letters*, 125(10):100503, 2020.
- [105] Román Orús. A practical introduction to tensor networks: Matrix product states and projected entangled pair states. *Annals of physics*, 349:117–158, 2014.
- [106] Ulrich Schollwöck. The density-matrix renormalization group in the age of matrix product states. *Annals of physics*, 326(1):96–192, 2011.
- [107] Frank Verstraete, Juan J Garcia-Ripoll, and Juan Ignacio Cirac. Matrix product density operators: Simulation of finite-temperature and dissipative systems. *Physical review letters*, 93(20):207204, 2004.
- [108] Jian Cui, J Ignacio Cirac, and Mari Carmen Banuls. Variational matrix product operators for the steady state of dissipative quantum systems. *Physical review letters*, 114(22):220601, 2015.
- [109] Hendrik Weimer, Augustine Kshetrimayum, and Román Orús. Simulation methods for open quantum many-body systems. *arXiv preprint arXiv:1907.07079*, 2019.
- [110] AJ Daley, JM Taylor, S Diehl, M Baranov, and P Zoller. Atomic three-body loss as a dynamical three-body interaction. *Physical review letters*, 102(4):040402, 2009.
- [111] Andrew J Daley. Quantum trajectories and open many-body quantum systems. *Advances in Physics*, 63(2):77–149, 2014.
- [112] Lars Bonnes and Andreas M Läuchli. Superoperators vs. trajectories for matrix product state simulations of open quantum system: a case study. *arXiv preprint arXiv:1411.4831*, 2014.
- [113] Aidan Strathearn, Peter Kirton, Dainius Kilda, Jonathan Keeling, and Brendon William Lovett. Efficient non-markovian quantum dynamics using time-evolving matrix product operators. *Nature communications*, 9(1):1–9, 2018.
- [114] Alex Kamenev. *Field theory of non-equilibrium systems*. Cambridge University Press, 2011.
- [115] Lukas M Sieberer, Michael Buchhold, and Sebastian Diehl. Keldysh field theory for driven open quantum systems. *Reports on Progress in Physics*, 79(9):096001, 2016.
- [116] Hermann Grabert, Peter Schramm, and Gert-Ludwig Ingold. Quantum brownian motion: The functional integral approach. *Physics Reports*, 168(3):115–207, 1988.

- [117] Alessandra Colla and Heinz-Peter Breuer. Entropy production and the role of correlations in quantum brownian motion. *Phys. Rev. A*, 104:052408, Nov 2021.
- [118] Philip JD Crowley and AG Green. Anisotropic landau-lifshitz-gilbert models of dissipation in qubits. *Physical Review A*, 94(6):062106, 2016.
- [119] Fergus Barratt. *The dynamics and control of quantum information out of equilibrium*. PhD thesis, Kings College London, 2021.
- [120] Soonwon Choi, Yimu Bao, Xiao-Liang Qi, and Ehud Altman. Quantum error correction in scrambling dynamics and measurement-induced phase transition. *Phys. Rev. Lett.*, 125:030505, Jul 2020.
- [121] Alberto Biella and Marco Schiró. Many-Body Quantum Zeno Effect and Measurement-Induced Subradiance Transition. *Quantum*, 5:528, August 2021.
- [122] Zack Weinstein, Yimu Bao, and Ehud Altman. Measurement-induced power-law negativity in an open monitored quantum circuit. *Phys. Rev. Lett.*, 129:080501, Aug 2022.
- [123] Mari Carmen Bañuls, J Ignacio Cirac, and Matthew B Hastings. Strong and weak thermalization of infinite nonintegrable quantum systems. *Physical review letters*, 106(5):050405, 2011.
- [124] Anindita Bera and Sudipto Singha Roy. Growth of genuine multipartite entanglement in random unitary circuits. *Phys. Rev. A*, 102:062431, Dec 2020.
- [125] Dong-Ling Deng, Xiaopeng Li, and S. Das Sarma. Quantum entanglement in neural network states. *Phys. Rev. X*, 7:021021, May 2017.
- [126] Tomaž Prosen and Marko Žnidarič. Matrix product simulations of non-equilibrium steady states of quantum spin chains. *Journal of Statistical Mechanics: Theory and Experiment*, 2009(02):P02035, 2009.
- [127] Mari Carmen Bañuls, NY Yao, S Choi, Mikhail D Lukin, and J Ignacio Cirac. Dynamics of quantum information in many-body localized systems. *Physical Review B*, 96(17):174201, 2017.
- [128] Yilun Yang, Sofyan Iblisdir, J Ignacio Cirac, and Mari Carmen Banuls. Probing thermalization through spectral analysis with matrix product operators. *Physical review letters*, 124(10):100602, 2020.
- [129] Aslı Çakan, J Ignacio Cirac, and Mari Carmen Bañuls. Approximating the long time average of the density operator: Diagonal ensemble. *Physical Review B*, 103(11):115113, 2021.
- [130] Mauro Schiulaz, E Jonathan Torres-Herrera, and Lea F Santos. Thouless and relaxation time scales in many-body quantum systems. *Physical Review B*, 99(17):174313, 2019.
- [131] Christopher David White, Michael Zaletel, Roger SK Mong, and Gil Refael. Quantum dynamics of thermalizing systems. *Physical Review B*, 97(3):035127, 2018.
- [132] Tibor Rakovszky, CW von Keyserlingk, and Frank Pollmann. Dissipation-assisted operator evolution method for capturing hydrodynamic transport. *Physical Review B*, 105(7):075131, 2022.

- [133] Edward Farhi, Jeffrey Goldstone, Sam Gutmann, and Michael Sipser. Quantum computation by adiabatic evolution. *arXiv preprint quant-ph/0001106*, 2000.
- [134] Emanuel Knill, Raymond Laflamme, and Wojciech H. Zurek. Resilient quantum computation. *Science*, 279(5349):342–345, 1998.
- [135] Fergus Barratt, Aleix Bou Comas, Philip JD Crowley, Vadim Oganesyan, Peter Sollich, and Andrew G Green. Dissipative failure of adiabatic quantum transport as a dynamical phase transition. *arXiv preprint arXiv:2012.15212*, 2020.
- [136] Arijeet Pal and David A. Huse. Many-body localization phase transition. *Phys. Rev. B*, 82:174411, Nov 2010.
- [137] Dmitry A. Abanin, Ehud Altman, Immanuel Bloch, and Maksym Serbyn. Colloquium: Many-body localization, thermalization, and entanglement. *Rev. Mod. Phys.*, 91:021001, May 2019.
- [138] Mark H Fischer, Mykola Maksymenko, and Ehud Altman. Dynamics of a many-body-localized system coupled to a bath. *Phys. Rev. Lett.*, 116:160401, Apr 2016.
- [139] Mariya V. Medvedyeva, Tomaž Prosen, and Marko Žnidarič. Influence of dephasing on many-body localization. *Phys. Rev. B*, 93:094205, Mar 2016.
- [140] Benjamin Everest, Igor Lesanovsky, Juan P. Garrahan, and Emanuele Levi. Role of interactions in a dissipative many-body localized system. *Phys. Rev. B*, 95:024310, Jan 2017.
- [141] Emanuele Levi, Markus Heyl, Igor Lesanovsky, and Juan P. Garrahan. Robustness of many-body localization in the presence of dissipation. *Phys. Rev. Lett.*, 116:237203, Jun 2016.
- [142] Henrik P. Lüschen, Pranjal Bordia, Sean S. Hodgman, Michael Schreiber, Saubhik Sarkar, Andrew J. Daley, Mark H. Fischer, Ehud Altman, Immanuel Bloch, and Ulrich Schneider. Signatures of many-body localization in a controlled open quantum system. *Phys. Rev. X*, 7:011034, Mar 2017.
- [143] Elisabeth Wybo, Michael Knap, and Frank Pollmann. Entanglement dynamics of a many-body localized system coupled to a bath. *Phys. Rev. B*, 102:064304, Aug 2020.
- [144] Carlo Sparaciari, Marcel Goihl, Paul Boes, Jens Eisert, and Nelly Huei Ying Ng. Bounding the resources for thermalizing many-body localized systems. *Communications Physics*, 4(1):3, 2021.
- [145] Z. Papić, E. Miles Stoudenmire, and Dmitry A. Abanin. Many-body localization in disorder-free systems: The importance of finite-size constraints. *Annals of Physics*, 362:714–725, 2015.
- [146] D.A. Abanin, J.H. Bardarson, G. De Tomasi, S. Gopalakrishnan, V. Khemani, S.A. Parameswaran, F. Pollmann, A.C. Potter, M. Serbyn, and R. Vasseur. Distinguishing localization from chaos: Challenges in finite-size systems. *Annals of Physics*, 427:168415, 2021.
- [147] Jens H. Bardarson, Frank Pollmann, and Joel E. Moore. Unbounded growth of entanglement in models of many-body localization. *Phys. Rev. Lett.*, 109:017202, Jul 2012.
- [148] Elmer V.H. Doggen, Igor V. Gornyi, Alexander D. Mirlin, and Dmitry G. Polyakov. Many-body localization in large systems: Matrix-product-state approach. *Annals of Physics*, 435:168437, 2021.

- [149] Seth M. Davis and Matthew S. Foster. Non-markovian dephasing of disordered quasi-one-dimensional fermion systems. *Phys. Rev. B*, 102:155101, Oct 2020.
- [150] Anthony J Leggett, SDAFMGA Chakravarty, Alan T Dorsey, Matthew PA Fisher, Anupam Garg, and Wilhelm Zwerger. Dynamics of the dissipative two-state system. *Reviews of Modern Physics*, 59(1):1, 1987.
- [151] Serge Florens, Davide Venturelli, and R Narayanan. Quantum phase transition in the spin boson model. In *Quantum Quenching, Annealing and Computation*, pages 145–162. Springer, 2010.
- [152] Robert Zwanzig. Memory effects in irreversible thermodynamics. *Physical Review*, 124(4):983, 1961.
- [153] Mario Berta, Fernando GSL Brandao, Jutho Haegeman, Volkher B Scholz, and Frank Verstraete. Thermal states as convex combinations of matrix product states. *arXiv preprint arXiv:1709.07423*, 2017.
- [154] Federico Carollo, Robert L. Jack, and Juan P. Garrahan. Unraveling the large deviation statistics of markovian open quantum systems. *Physical Review Letters*, 122(13), 2019.
- [155] Federico Carollo, Juan P. Garrahan, and Robert L. Jack. Large deviations at level 2.5 for markovian open quantum systems: Quantum jumps and quantum state diffusion. *Journal of Statistical Physics*, 184(1), jul 2021.
- [156] John Preskill. Quantum Computing in the NISQ era and beyond. *Quantum*, 2:79, August 2018.
- [157] Ye Wang, Mark Um, Junhua Zhang, Shuoming An, Ming Lyu, Jing-Ning Zhang, L.-M. Duan, Dahyun Yum, and Kihwan Kim. Single-qubit quantum memory exceeding ten-minute coherence time. *Nature Photonics*, 11(10):646–650, sep 2017.
- [158] X. Shi, S. L. Todaro, G. L. Mintzer, C. D. Bruzewicz, J. Chiaverini, and I. L. Chuang. Ablation loading of barium ions into a surface electrode trap, 2023.
- [159] J. M. Pino, J. M. Dreiling, C. Figgatt, J. P. Gaebler, S. A. Moses, M. S. Allman, C. H. Baldwin, M. Foss-Feig, D. Hayes, K. Mayer, C. Ryan-Anderson, and B. Neyenhuis. Demonstration of the trapped-ion quantum ccd computer architecture. *Nature*, 592(7853):209–213, 2021.
- [160] Michael Foss-Feig, David Hayes, Joan M. Dreiling, Caroline Figgatt, John P. Gaebler, Steven A. Moses, Juan M. Pino, and Andrew C. Potter. Holographic quantum algorithms for simulating correlated spin systems. *Phys. Rev. Research*, 3:033002, Jul 2021.
- [161] Eli Chertkov, Justin Bohnet, David Francois, John Gaebler, Dan Gresh, Aaron Hankin, Kenny Lee, David Hayes, Brian Neyenhuis, Russell Stutz, Andrew C. Potter, and Michael Foss-Feig. Holographic dynamics simulations with a trapped-ion quantum computer. *Nature Physics*, 18(9):1074–1079, aug 2022.
- [162] James Dborin, Vinul Wimalaweera, Fergus Barratt, Eric Ostby, Thomas E O’Brien, and Andrew G Green. Simulating groundstate and dynamical quantum phase transitions on a superconducting quantum computer. *arXiv preprint arXiv:2205.12996*, 2022.
- [163] Juan Carlos Garcia-Escartin and Pedro Chamorro-Posada. swap test and hong-ou-mandel effect are equivalent. *Phys. Rev. A*, 87:052330, May 2013.

- [164] Sheng-Hsuan Lin, Rohit Dilip, Andrew G. Green, Adam Smith, and Frank Pollmann. Real- and imaginary-time evolution with compressed quantum circuits. *PRX Quantum*, 2:010342, Mar 2021.
- [165] Stefano Barison, Filippo Vicentini, and Giuseppe Carleo. An efficient quantum algorithm for the time evolution of parameterized circuits. *Quantum*, 5:512, July 2021.
- [166] Noah F. Berthusen, Thaís V. Trevisan, Thomas Iadecola, and Peter P. Orth. Quantum dynamics simulations beyond the coherence time on noisy intermediate-scale quantum hardware by variational trotter compression. *Phys. Rev. Res.*, 4:023097, May 2022.
- [167] James C. Spall. Multivariate stochastic approximation using a simultaneous perturbation gradient approximation. *IEEE Transactions on Automatic Control*, 37:332–341, 1992.